

Bose-Einstein Correlations in e^+e^- Annihilation

Een wetenschappelijke proeve op het gebied van de
Natuurwetenschappen, Wiskunde en Informatica

Proefschrift

ter verkrijging van de graad van doctor
aan de Radboud Universiteit Nijmegen
op gezag van de rector magnificus prof. mr. S.C.J.J. Kortmann,
volgens besluit van het College van Decanen
in het openbaar te verdedigen op donderdag 4 september 2008,
om 15.30 uur precies

door

Tamás Novák

geboren op 16 mei 1979
te Gyöngyös,
Hongarije.

Promotores: Prof. dr. E.W. Kittel
Prof. dr. T. Csörgő, MTA KFKI RMKI, Budapest
and University of São Paulo

Copromotor: Dr. W.J. Metzger

Manuscriptcommissie: Prof. dr. S.J. de Jong
Dr. B. Buschbeck, ÖAW, Wien
Prof. dr. E.A. De Wolf, UA, Antwerpen

Bose-Einstein Correlations in e^+e^- Annihilation

An academic essay in Faculty of Science

Doctoral thesis

to obtain the degree of doctor
from Radboud University Nijmegen
on the authority of the Rector Magnificus prof. dr. S.C.J.J. Kortmann,
according to the decision of the Council of Deans
to be defended in public on Thursday, 4 September 2008
at 3:30 pm

by

Tamás Novák

born in Gyöngyös, Hungary
on 16 May 1979.

Supervisors: Prof. dr. E.W. Kittel
Prof. dr. T. Csörgő, MTA KFKI RMKI, Budapest
and University of São Paulo

Co-supervisor: Dr. W.J. Metzger

Manuscript committee: Prof. dr. S.J. de Jong
Dr. B. Buschbeck, ÖAW, Wien
Prof. dr. E.A. De Wolf, UA, Antwerpen

To Judit
for her patience, support and love...

Contents

1	Introduction	1
1.1	Theoretical Description of e^+e^- Collisions	1
1.2	Monte Carlo Generators	5
1.2.1	Hard Processes	5
1.2.2	Soft Processes	5
1.3	Description of Final-state Hadrons	6
1.3.1	Event-shape Variables	6
1.3.2	Single-particle Variables	7
1.4	Brief History of Bose-Einstein Correlations	8
2	Experimental Setup	11
2.1	LEP at CERN	11
2.2	The L3 Detector	13
2.2.1	The Silicon Microvertex Detector	16
2.2.2	The Time Expansion Chamber and Z Chamber	16
2.2.3	The Electromagnetic Calorimeter	18
2.2.4	The Hadron Calorimeter	19
2.2.5	The Muon Detector	19
2.2.6	Other Detector Components	20
2.3	Hadronic Energy Measurements	21
2.4	Data Processing	23
2.4.1	Trigger System and Data Acquisition	23
2.4.2	Event Reconstruction	23

2.4.3	Detector Simulation	24
3	Event and Track Selection	27
3.1	Event Selection	27
3.2	Track Selection	31
3.3	Further Event Selection	36
3.4	Two-jet and Three-jet Event Selection	37
4	Introduction to BEC	39
4.1	Theory	39
4.2	Bose-Einstein Correlation Function	42
4.3	Determination of R_2	43
4.3.1	The Reference Sample	44
4.3.2	Corrections	44
4.4	The Longitudinal Center-of-Mass System	45
4.5	Parametrization of R_2	46
4.5.1	Gaussian Source Distribution	47
4.5.2	Edgeworth Expansion	49
4.5.3	Lévy Stable Source Distribution	50
4.6	Long-range Correlation	52
4.7	Systematic Uncertainties and Checks	52
5	Results on the Parametrization of R_2	55
5.1	Introduction	55
5.2	Proper Variables of R_2	55
5.2.1	Assuming Dependence on $(Q_z, Q_{\text{side}}, Q_{\text{out}})$	56
5.2.2	Investigating Two-dimensional Dependence	57
5.3	Assuming that R_2 is a function of Q	63
5.4	Summary	70
6	Determination of the Proper Shape of BEC	71
6.1	The τ -model	71

6.2	Functional Dependence on Q	73
6.2.1	Symmetric Parametrizations	73
6.2.2	Results for the Symmetric Parametrizations	75
6.2.3	One-sided Parametrization	75
6.2.4	Results for the Asymmetric Parametrization with Average a	78
6.2.5	The Dependence on \overline{m}_t	79
6.2.6	Systematic Uncertainties on Fitted Results	87
6.2.7	Controlling the τ -model with additional measurements	87
6.3	Summary and Conclusions	90
7	Reconstruction of the Emission Function	91
7.1	The Emission Function of Two-jet Events	91
8	BEC and the Anomalous Dimension of QCD	97
8.1	Introduction	97
8.2	(Multi)fractal Structure of the QCD Jets	98
8.2.1	Dipole Formulation	98
8.2.2	Multiplicity Measure	99
8.2.3	Fractal Structures	100
8.3	The Anomalous Dimension of QCD Jets and BEC	100
9	Conclusions	105
	Appendix: Lévy Stable Distributions	107
	Summary	115
	Samenvatting	119
	Acknowledgements	123
	Curriculum Vitae	125

Chapter 1

Introduction

In this thesis we use Bose-Einstein correlations (BEC) to investigate the space-time structure of the pion production region in e^+e^- annihilations at a center-of-mass (cms) energy of $\sqrt{s} = 91$ GeV. We analyse data collected in 1994 by the L3 experiment at the Large Electron Positron (LEP) Collider at the European Organization for Nuclear Research (CERN).

The structure of this thesis is as follows: in Chapter 1, we sketch our present theoretical picture of the physics of e^+e^- collisions. In Chapter 2, we introduce the basic properties of the LEP accelerator that produced these e^+e^- collisions and discuss the setup of the L3 detector. In Chapter 3, we present the selection of the events for the data analysis, which is detailed in Chapters 4, 5 and 6. In particular, Chapter 4 summarizes the experimental methods of extracting Bose-Einstein correlation functions from L3 data, Chapter 5 discusses the choice of variables to parametrize these correlations, while Chapter 6 focuses on the determination of the shape of the correlation functions, in terms of these variables. In Chapter 7, we reconstruct the particle emission source in e^+e^- collisions based on the results of Chapters 5 and 6. In Chapter 8, we relate the shape parameter of the Bose-Einstein correlation function to the fundamental theory of strong interactions, in particular, to the running coupling constant, α_s , of Quantum Chromo Dynamics (QCD). Finally, in Chapter 9 we summarize and conclude. In the Appendix, some mathematical properties of Lévy stable distributions are given for reference.

1.1 Theoretical Description of e^+e^- Collisions

Electron-positron scattering is one of the basic experiments to study the fundamental properties of matter. The clean and exactly known initial state of this point-like reaction allows a straightforward test of the Standard Model, the theory describing the interactions between all presently observed elementary

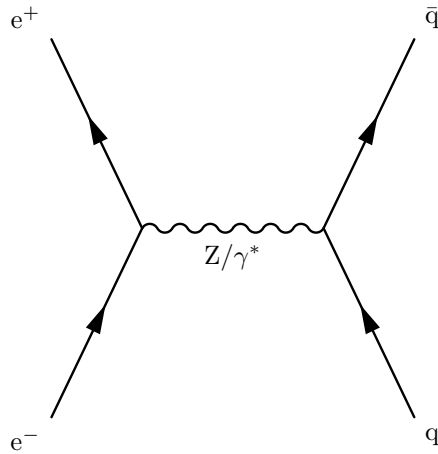


Figure 1.1: The annihilation process $e^+e^- \rightarrow q\bar{q}$.

particles. Strong support for the validity of the Standard Model was obtained with the discovery in $p\bar{p}$ interactions of the W boson [1,2] and the Z [3,4] boson with masses close to their predicted values and by the precision tests at LEP and the Stanford Linear Collider [5].

In an e^+e^- collider, the e^+e^- collisions are usually observed in the center-of-mass system (cms). The main advantage of the cms is that there is no energy loss for center-of-mass motion: if p and p' are the four-momenta of the positron and the electron¹, then the total energy in the cms is $E \equiv \sqrt{s} = \sqrt{(p+p')^2}$.

For a low center of mass energy, the annihilation process $e^+e^- \rightarrow q\bar{q}$ is dominated by an s-channel photon exchange (Fig. 1.1). When the cms energy is around 91 GeV, there is enough energy available for the production of a Z boson and Z exchange becomes the dominant process. The most probable result of an e^+e^- collision near the Z resonance is multihadron production due to the large branching ratio of $Z \rightarrow q\bar{q}$.

Fig. 1.2 shows a schematic illustration of a typical hadronic event in e^+e^- annihilation, where the production mechanism of hadrons can be divided into four stages. In the following, we shall briefly describe these theoretical ideas.

1. The electroweak stage.

In this stage, the e^+e^- pair annihilates into a virtual Z/γ^* resonance according to the theory of electroweak interactions. The virtual Z/γ^* , in turn, decays into a $q\bar{q}$ pair, also following the theory of electroweak interactions. The initial e^+ or e^- may radiate one or more photons by

¹In this thesis $x \equiv x^\mu = (t, r_x, r_y, r_z)$ and $p \equiv p^\mu = (E, p_x, p_y, p_z)$ stand for the four-coordinate and four-momentum vectors, respectively. For a particle with mass m , $p^\mu p_\mu = m^2$. Lower and upper indices indicate covariant and contravariant coordinates, respectively. Note also that we set $\hbar = c = 1$.

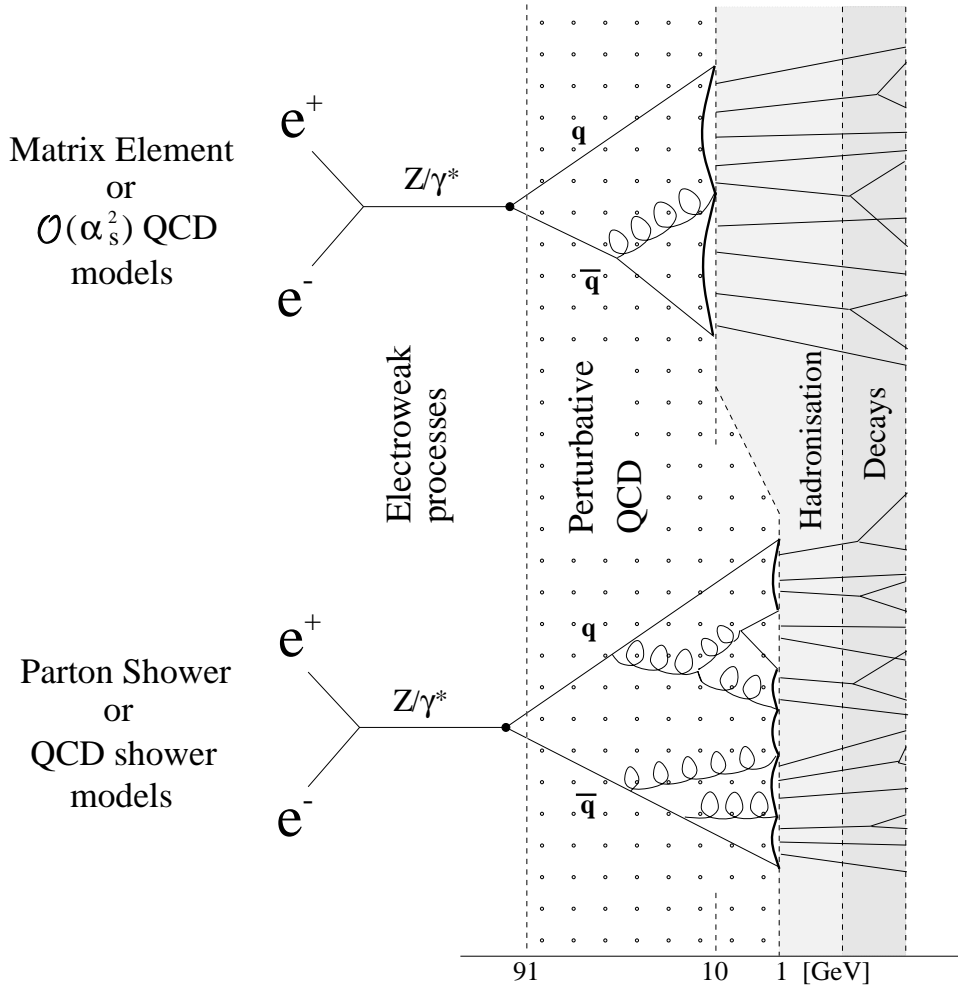


Figure 1.2: A schematic illustration of the process $e^+e^- \rightarrow q\bar{q} \rightarrow \text{hadrons}$.

bremsstrahlung (initial-state photon radiation) before annihilating. This reduces the cms energy of the Z/γ^* decay and, therefore, the total effective mass of the hadronic final state.

2. The perturbative QCD stage.

In the second stage, the quark/anti-quark may radiate gluons according to the theory of quantum chromodynamics (QCD). The gluons may radiate other gluons or split into $q\bar{q}$ pairs, thus giving rise to parton showers emitted near the direction of the primary partons (i.e. the initial quark and antiquark), thus giving a typical jet structure to the events.

Two approaches may be used to describe the production of partons.

The first approach is called the matrix element (ME) method. Feynman diagrams are exactly calculated within QCD, order by order in the strong coupling constant α_s . In principle, these calculations take all interference terms into account. However, such calculations become more and more complicated as the order of α_s is increased. The calculations have been carried out only up to $O(\alpha_s^2)$, i.e., up to four partons in the final state.

The second approach is called the parton shower (PS) method. This approach repeatedly applies the basic splitting processes, $q \rightarrow qg$, $g \rightarrow gg$ and $g \rightarrow q\bar{q}$, using differential probabilities. This method is based on the framework of the modified leading logarithmic approximation (MLLA) [6,7]. In the leading logarithmic approximation (LLA) [8–11] only the leading logarithmic terms in the perturbative expansion are kept. In the MLLA some aspects of the next-to-leading logarithmic approximation (NLLA) [12–14] are also included.

3. The hadronization stage.

In practice, for the description of the transition of colored partons into colorless hadrons only phenomenological models are available. The most commonly used model is the Lund string hadronization model [15]. Colored strings are stretched between the color charges of different partons. The stretched strings break by creating quark-antiquark pairs. Quarks and antiquarks subsequently combine to form color-singlet hadron states. The model can be used both in combination with the PS or the ME perturbative QCD models.

4. The decay stage of unstable hadrons.

The last stage represents the decay of unstable hadrons into experimentally observable particles (mostly pions and kaons). For this stage, again no generally reliable models are available. The experimentally available information on the particle lifetimes and branching ratios is used to predict the outcome.

1.2 Monte Carlo Generators

Monte Carlo generators are essential in our work. They are able to generate a complete particle final state. The assumptions of the models incorporated in the Monte Carlo programs can be tested by comparing properties of these events to those of the data. Even more important is their use after passing them through a detector simulation (see Sub-Sect. 2.4.3) in evaluating detector acceptance and efficiency.

Events are generated independently, and each property, such as quark flavor, particle direction, fragmentation function, branching ratio, is randomly generated according to its probability of occurrence as determined by the particular physics process. The generator also takes into account all the constraints and limitations imposed by the dynamics and the kinematics of the whole chain of processes.

In this thesis, two Monte Carlo models, JETSET [16] and HERWIG [17], are used to simulate the hadron production process at the Z resonance in e^+e^- collisions.

The simulation of hadronic events follows the four stages described in Sect. 1.1 implemented in two main groups: the hard processes in which electroweak and perturbative QCD calculations are used to produce partons, and the fragmentation (soft phase) in which the hadronization processes and the decay of particles are treated phenomenologically.

1.2.1 Hard Processes

The hard processes in hadron production in e^+e^- describe the $e^+e^- \rightarrow Z/\gamma^* \rightarrow q\bar{q}$ process, i.e., the production of a primary quark-antiquark pair, and the final-state radiation of gluons and quarks. The flavor of the quarks in the final state of each event is picked at random, according to the relative couplings.

In JETSET, the higher-order QCD corrections can be described either with the parton shower approach (JETSET PS), which is based on the MLLA framework, or with the matrix element approach (JETSET ME), the latter only allowing to choose between a maximum of 2, 3 or 4 partons in the final-state. The default is the parton shower. In HERWIG, the parton shower approach is, like in JETSET, based on the MLLA scheme. In both JETSET and HERWIG energy and momentum conservation is applied at each branching.

1.2.2 Soft Processes

The basic hadronization scheme implemented in JETSET is the Lund string model [18]. The physical picture behind this model is that of a quark and an-

quark moving in opposite directions, losing energy to the color field between them, which has a string-like configuration with uniform energy density along the string. As the q and \bar{q} move apart, the string may break into two less energetic strings producing a colorless quark-antiquark pair. The resulting string pieces can break up similarly on their turn, until the mass of each resulting string piece has fallen to the hadronic mass scale. Each final $q\bar{q}$ segment forms a meson, and baryon production is introduced by allowing the production of diquark-antidiquark pairs. Gluons are incorporated in the string picture as kinks in the string, acting effectively like a quark and an antiquark located at the same place. This model is the most popular and also the most successful in describing the data.

There is another hadronization scheme, the independent fragmentation model [19], available in JETSET as an option. It has the advantage of simplicity supposing that each parton fragments into hadrons independently. However, it gives only a very approximate description of hadronization and cannot be considered as an alternative to the Lund string model.

The HERWIG generator uses a cluster fragmentation model which implements the idea of pre-confinement [20, 21]. The physical picture is that all of the gluons resulting from the parton shower are split into light quark-antiquark pairs, which are then locally (in phase space) grouped into colorless clusters which decay into hadrons while keeping the main properties of the partonic final state. HERWIG is reasonably successful in describing e^+e^- data, though in most comparisons it is somewhat worse than JETSET.

As the last step of the Monte Carlo generation, unstable hadrons produced during the hadronization process decay into stable particles according to the experimental information on particle lifetimes and branching ratios.

There are several parameters which can be adjusted in both JETSET and HERWIG to ensure a good description of the experimental data.

1.3 Description of Final-state Hadrons

1.3.1 Event-shape Variables

To characterize the hadronic event as a whole, we define several so-called event-shape variables.

Thrust

Thrust, T_{thrust} , is a measure of the alignment of the particles within an event along a common axis, the thrust axis, \mathbf{n}_3 . The thrust axis is the vector along

which the maximum alignment is found according to the following formula [22]:

$$T_{\text{thrust}} = \frac{\sum_i |\mathbf{p}_i \cdot \mathbf{n}_3|}{\sum_i |\mathbf{p}_i|}, \quad (1.1)$$

where \mathbf{p}_i is the momentum vector of particle i . The sum \sum_i runs over all final-state particles. The value of T_{thrust} lies in the interval $[1/2, 1]$, with $T_{\text{thrust}} = 1/2$ for a fully isotropic final state. The value of T_{thrust} approaches unity as the event configuration in the hadronic cms becomes more two-jet like. As the direction on this axis is not defined by Eq. (1.1) (due to taking the absolute value of the dot product: both \mathbf{n}_3 and $-\mathbf{n}_3$ give the same value of the thrust), the positive direction of the thrust axis is randomly assigned.

Major

The major axis, \mathbf{n}_2 , is defined in the plane perpendicular to the event thrust axis \mathbf{n}_3 , in the same way as thrust, but is maximized in this perpendicular plane [23],

$$T_{\text{major}} = \frac{\sum_i |\mathbf{p}_i \cdot \mathbf{n}_2|}{\sum_i |\mathbf{p}_i|}, \quad \mathbf{n}_3 \perp \mathbf{n}_2. \quad (1.2)$$

The positive direction of the major axis is also chosen randomly.

In the case of three-jet events, in the hadron production process in e^+e^- collisions, the $(\mathbf{n}_3, \mathbf{n}_2)$ plane is identified with the plane of the q , \bar{q} and the hardest gluon emitted [23].

Minor

The minor axis, \mathbf{n}_1 , is defined as orthogonal to both the thrust and major axes, according to a right-handed coordinate system.

1.3.2 Single-particle Variables

In this subsection we shall consider variables defined in the orthonormal system $(\mathbf{n}_1, \mathbf{n}_2, \mathbf{n}_3)$ defined with respect to the thrust and major axis. A produced particle can be characterized by the following variables:

Rapidity y :

The rapidity of a particle is defined as

$$y = \frac{1}{2} \ln \left(\frac{E + p_z}{E - p_z} \right), \quad (1.3)$$

where p_z is the momentum component along the z axis, i.e., the thrust axis, and E is the energy of the particle. Since the particle type is not identified, we

may assume that it has the mass of the most abundant type of hadron, i.e. the mass of the pion. The rapidity has the important property of being additive with respect to a Lorentz transformation along the z -axis; thus the shape of the rapidity distribution is invariant.

Azimuthal Angle ϕ :

The azimuthal angle of a charged particle is defined with respect to the minor and major axes ($\mathbf{n}_1, \mathbf{n}_2$) as

$$\phi = \arctan\left(\frac{p_y}{p_x}\right). \quad (1.4)$$

The ϕ variable is invariant under Lorentz transformations along the z -axis.

Transverse Momentum p_t :

The transverse momentum

$$p_t = \sqrt{p_x^2 + p_y^2} \quad (1.5)$$

is the magnitude of the momentum in the plane transverse to the z -axis. It is invariant under Lorentz transformations along the z -axis.

1.4 Brief History of Bose-Einstein Correlations

Essentially, intensity correlations appear due to the Bose-Einstein or Fermi-Dirac symmetrization of identical bosons or fermions, respectively.

Glauber was the first to point out [24] that such intensity correlations are not present in lasers. The understanding of the theory of lasers was one of the key steps in the birth of a new field of science, quantum optics, and the related studies of intensity correlations by Glauber were cited when he was awarded half of the Nobel Prize in physics in 2005 [25].

A new method of measuring the angular diameter of main sequence stars was introduced in astronomy in the middle of 1950s by R. Hanbury Brown and R. Q. Twiss [26–28], namely, the so-called intensity interferometry based on interference of photons emitted by independent sources on the star and detected by two receivers on earth. Likewise, in particle physics, one can in principle use Bose-Einstein correlations between identical bosons to measure the size of the region from which particles originate in a high-energy collision, provided that these bosons are produced incoherently.

The first experiment dealing with Bose-Einstein correlations in high-energy physics dates back to 1959 [29]. The experiment, $p\bar{p}$ annihilation at 1.05 GeV/ c , indicated that the distribution of the angle between pairs of pions deviates from

the prediction of the conventional statistical model. In particular it was found that there is a clear difference between the angular distribution for pion pairs of like-sign charge and that for pairs of unlike-sign charge: like-sign pion pairs are more likely to be emitted into the same hemisphere than unlike-sign pairs.

In order to explain the bulk of that effect, Bose-Einstein symmetrization was applied by G. Goldhaber, S. Goldhaber, W. Lee and A. Pais (GGLP) [30]. By modifying the classical statistical model to include symmetrization between identical particles, the authors were able to reproduce the experimental results at least qualitatively.

In recent years, Bose-Einstein correlations have become a subject of intense experimental activity, both in nuclear and particle physics [31, 32]. The main reason for this is the expectation that one could obtain important information about the space-time extension and the coherence of the hadronic sources from Fourier transforms of the measurable particle momentum correlations. The effect is often referred to as the HBT effect, GGLP effect, intensity interferometry, femtoscopy or simply as BE correlation or BEC.

Leaving a more detailed introduction of this field to Chapter 4, let me highlight some interesting directions in the study of intensity correlations during the last 50 years. Similarities between Bose-Einstein correlations in different reactions might indicate an important limitation of our understanding of particle correlations in e^+e^- , hadron + hadron and nucleus + nucleus reactions. For example, the mass and the transverse mass dependences of the Bertsch-Pratt (see Sect. 4.4) radius parameters in these reactions seem to be very similar, in spite of the fact that the scales and the reaction mechanisms are completely different [31–35]. Parametrizations which go beyond the usual Gaussian approximation have been introduced: a) the Edgeworth and Laguerre expansions utilize complete sets of polynomials that are orthogonal with respect to given weight functions (see [36] and Sect. 4.5.2); b) the Lévy index of stability is a new parameter of the two- and three-particle Bose-Einstein correlation function (see [37, 38] and Sect. 4.5.3). It characterizes the power-law tails of Lévy stable distributions, which appear in physical systems where the final distribution is obtained as a convolution of many elementary random steps. Furthermore, intensity correlations of non-identical particle pairs are new and promising tools in heavy ion physics, given the large number of possible combinations of various types of particles.

In the next Chapter, the LEP collider and the L3 experiment are described.

Chapter 2

Experimental Setup

2.1 LEP at CERN

The Large Electron Positron (LEP) collider [39–41], a part of CERN (European Organization for Nuclear Research), was designed to accelerate and collide electrons and positrons. It was located at the Swiss-French border (see Fig. 2.1) near the city of Geneva.

The LEP collider was in operation from August 1989 to November 2000. During the period from 1989 to 1995, called the LEP I phase, its working energy was around 46 GeV per colliding beam of particles, thus creating center of mass energies of about 92 GeV, approximately the mass of the Z boson. This period was dedicated to the extensive study of the properties of the Z boson. At the end of 1995, LEP entered its second phase, called LEP II. A major upgrade took place in order to increase the LEP working energy to allow the study of the production of W^+W^- pairs and of ZZ pairs and to continue the search, already started at LEP I, for the Higgs boson and for supersymmetric particles.

LEP was installed in an underground tunnel with a circumference of 26.7 km, at a depth varying from 50 to 150 meters. It consisted of eight short straight sections in which the particles were accelerated and eight long curved sections in which the particles were deflected. LEP had four intersection regions, each surrounded by a particle detector, that measured the properties of the particles generated in the collision. Each of the detectors, ALEPH, OPAL, DELPHI and L3, was optimized differently to study various aspects of high energy physics.

Before injection into LEP, the electrons and positrons were first pre-accelerated. Lower energy CERN accelerators, built for previous experiments, were used as the LEP injection system. The system consisted of the following interconnected accelerators (see Fig. 2.2):

- LIL: The system started with the LEP Injector Linacs, producing elec-

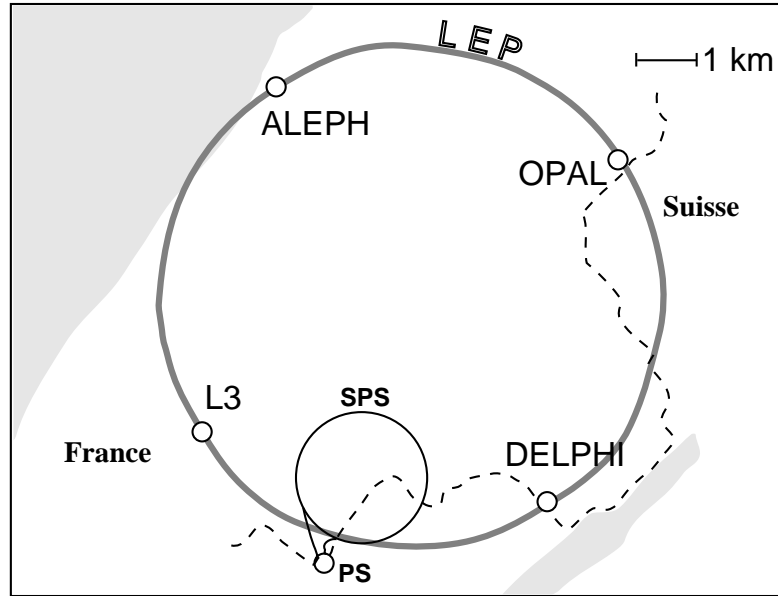


Figure 2.1: The LEP ring under the surface of the French-Swiss border near Geneva.

trons of 200 MeV which stroke a tungsten target (converter) to produce positrons. These positrons were accelerated to 600 MeV by the second linac. The electrons for LEP were produced by an electron gun located near the converter.

- EPA: The Electron Positron Accumulator accumulated the electrons and positrons from the LIL into bunches. The bunches were stored here until they reached the required intensity.
- PS: The Proton Synchrotron was used to increase the energy of the bunches of electrons and positrons to 3.5 GeV.
- SPS: The Super Proton Synchrotron with a circumference of 7 kilometers accelerated the bunches to 20 GeV. At this stage the particles were injected into the LEP ring.

After filling LEP, the particles were further accelerated until they reached the required energy and the desired degree of collimation. As soon as the beams became stable they were made to collide in the four detectors.

The collision rate at the interaction point divided by the interaction cross section is called the luminosity, L . At LEP it was typically of the order of $10^{31}\text{cm}^{-2}\text{s}^{-1}$ and depends on several LEP parameters such as the beam energy, the number of bunches, the current and the size of the beams at the interaction points. Some of these parameters are difficult to measure precisely. The

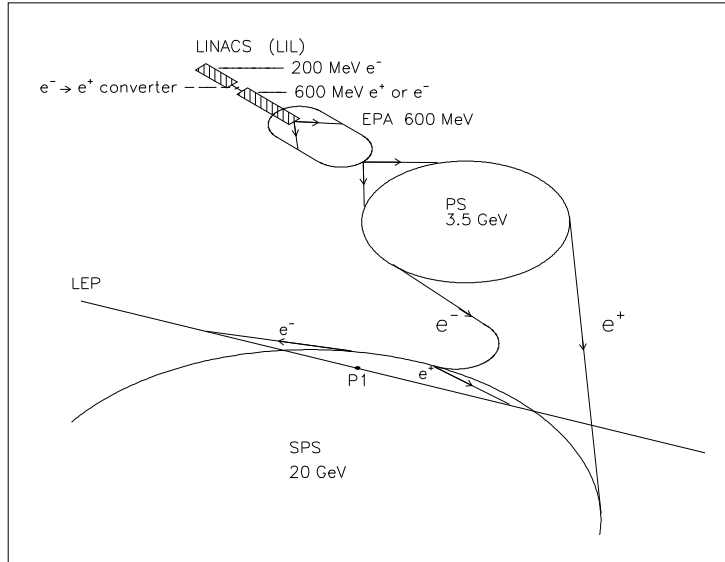


Figure 2.2: A schematic view of the accelerator system at LEP.

time integrated luminosity can be more conveniently measured using small-angle Bhabha scattering ($e^+e^- \rightarrow e^+e^-$) as

$$\mathcal{L} = \int_0^T L dt = \frac{N_{\text{Bhabha}}}{\sigma_{\text{Bhabha}}}, \quad (2.1)$$

because the Bhabha cross section, σ_{Bhabha} , is theoretically well known for small scattering angles. Here, N_{Bhabha} is the number of small-angle Bhabha events collected in a period of time T .

2.2 The L3 Detector

The L3 experiment [42] at LEP is based on a large magnetic detector optimized for the precision measurement of photons, electrons, muons and hadron jets. Fig. 2.3 and Fig. 2.4 show the perspective view and longitudinal cross section of the detector, respectively. The various subdetectors, as well as the directions of the positron and electron beams, are indicated.

We shall use the following coordinate system: the origin is at the center of the detector, the x -axis is perpendicular to the beam, towards the center of the LEP ring, the y -axis points upwards and the z -axis is parallel to the beam pipe and pointing in the flight-direction of the electron beam. It is also useful to introduce polar coordinates r, θ, ϕ , where r is the distance from the interaction

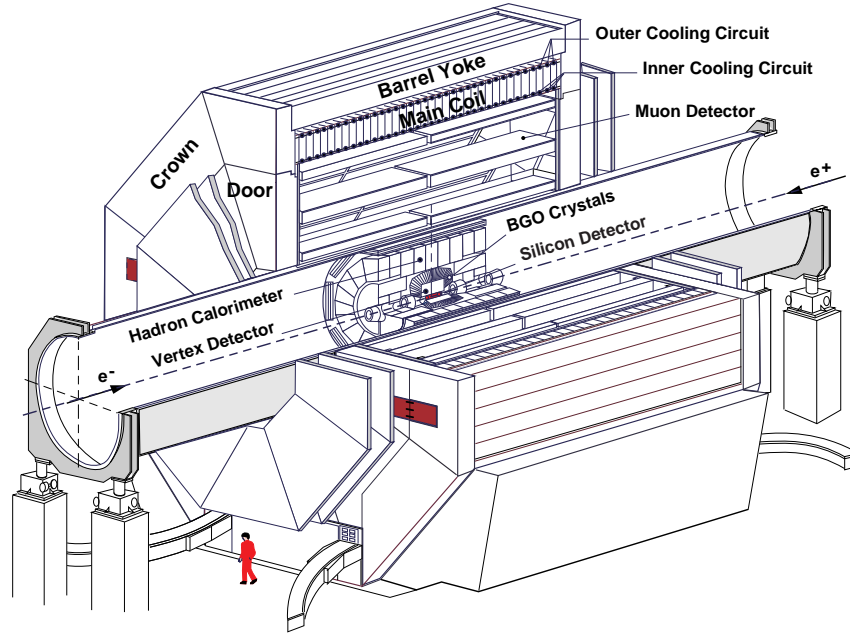


Figure 2.3: Perspective view of the L3 detector.

point, the polar angle, $\theta \in [0, \pi]$, is the angle between the positive z -axis and the r vector and the azimuthal angle, $\phi \in [0, 2\pi]$, is the angle between the x -axis and the projection of the r vector onto the xy plane.

The whole detector was immersed in a magnetic field of 0.5 T along the z -axis produced by a very large volume octagonal solenoid magnet. Both the length and the inner diameter of this magnet were about 12 meters.

The L3 detector was symmetric with respect to the interaction point and was divided into several specialized sub-detectors. The particles produced at the interaction point and their possible decay products successively encountered the following sub-detectors, while traversing the detector.

- Silicon Microvertex Detector (SMD): measured accurately points along a charged particle's trajectory immediately outside the beam pipe.
- Time Expansion Chamber (TEC): a type of wire chamber, that measured the tracks of charged particles. It was part of the central tracking detector which, in addition to the TEC, also contained wire chambers (the Z-chambers) that measured the z coordinate of the particles. From the curvature of the trajectories the charge and the transverse (xy plane) momentum of the particles were determined.
- Electromagnetic CALorimeter (ECAL): arrays of Bismuth-Germanate also called Bismuth-Germanium-Oxide or BGO, crystals, that measured the

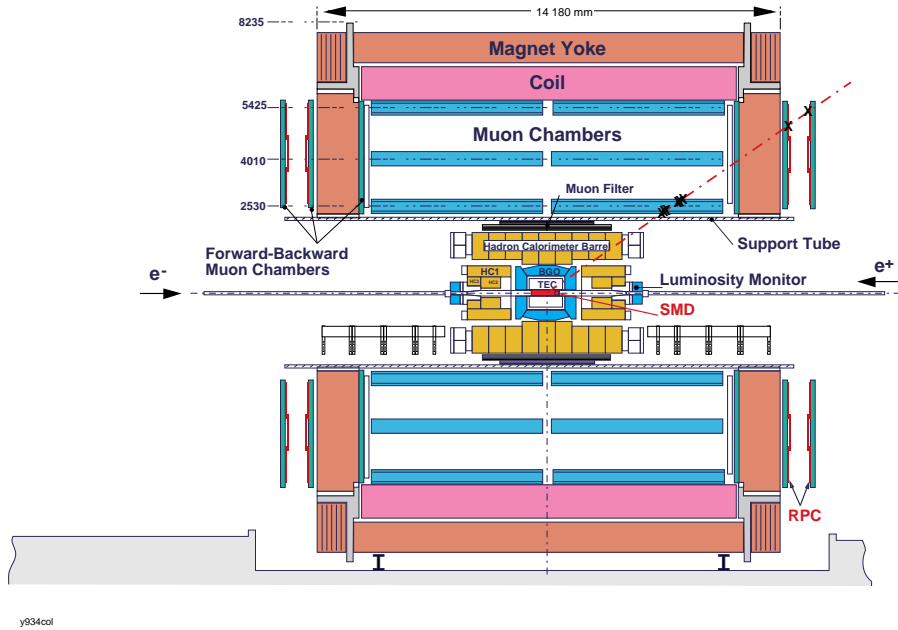


Figure 2.4: Longitudinal cut through the L3 detector.

energy and direction of electrons and photons.

- Scintillation counters: arrays of plastic sheets in which light was produced by the passage of charged particles. The scintillation hit multiplicity was used to trigger hadronic events. The system also recorded the particle's time-of-flight which was used to distinguish between particles from cosmic ray background and particles produced by the e^+e^- collisions.
- Hadron CALorimeter (HCAL): consisted of alternating layers of proportional wire chambers and slabs of depleted uranium, to measure energies of hadrons.
- Muon chambers (MUCH): arrays of wire chambers. They identified and measured the momentum of the muons. Muons have a very low interaction cross section and were hence able to pass through all the previous subdetectors.

All of the subdetectors consisted of a central part (the barrel) and a forward and backward part (the endcaps), except the SMD and the TEC which only had a central part.

In the following sections, the major subdetectors will be discussed in more detail. The SMD, TEC, ECAL and HCAL are of direct importance for the variables used in our analysis.

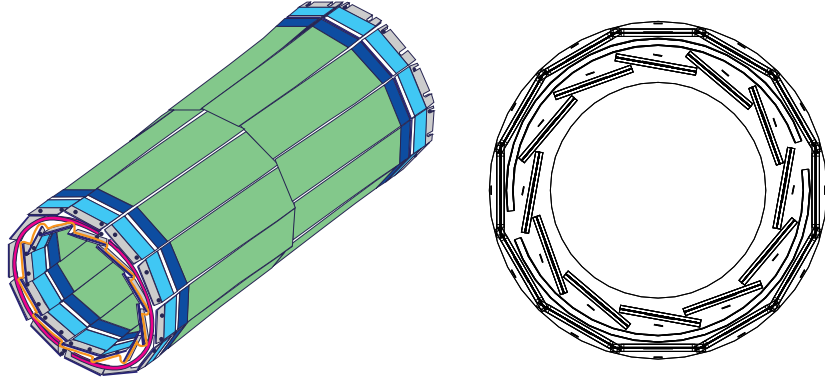


Figure 2.5: The Silicon Microvertex Detector. Left: 3-D view. Right: xy -view.

2.2.1 The Silicon Microvertex Detector

The Silicon Microvertex Detector (SMD) was installed in 1993. It was used to measure the tracks of charged particles close to the interaction point, in order to resolve possible secondary vertices which arise from the decay of short-lived particles such as hadrons containing b quarks.

This detector was directly attached to the beryllium beam pipe and consisted of two radial layers supporting 12 ladders, at 61.7 mm and 77.4 mm, respectively. The length of the SMD was 30 cm which covered the polar angle $22^\circ \leq \theta \leq 158^\circ$. Each ladder contained 4 silicon microstrip sensors made of high-purity n-type silicon. On its junction side, each sensor carried strips designed to measure the $r\phi$ coordinate, while its ohmic side had strips perpendicular to those of the junction side, in order to measure the rz coordinate. The SMD could reach a position resolution of $7.5 \mu\text{m}$ in the $r\phi$ direction and $14.3 \mu\text{m}$ in the z direction [43].

The principle of detection with the silicon microstrip is the following. A particle passing through the silicon sensor produces electron-hole pairs. By applying a voltage bias between the two sides of the sensor, holes and electrons drift to the nearest strips on both surfaces, allowing a simultaneous measurement of the $r\phi$ and rz coordinates. A 3-D and an xy -view of the SMD are shown in Fig. 2.5.

2.2.2 The Time Expansion Chamber and Z Chamber

The Time Expansion Chamber (TEC) and Z Chamber were used to reconstruct the trajectory (track) of a charged particle in $r\phi$ (TEC) and z (Z Chamber), and to measure its transverse momentum, which is calculated from the curvature of the tracks. An xy -view of the SMD, TEC and Z Chamber is shown in Fig. 2.6.

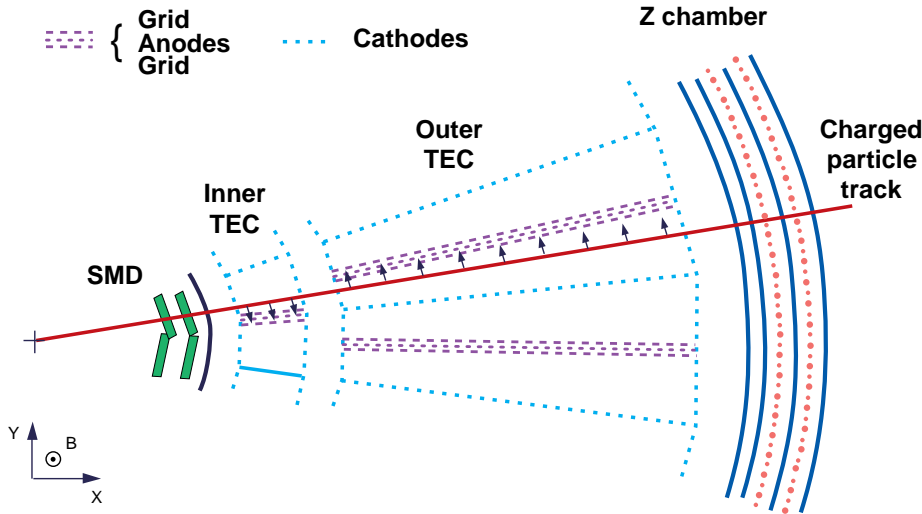


Figure 2.6: xy -view of a section of the central tracking system: the SMD, the TEC and the Z Chamber.

The TEC consisted of a cylindrical drift chamber placed along the beam axis. The chamber was filled with a mixture of 80% carbon dioxide and 20% iso-butane at a temperature of 291K and a pressure of 1.2 bar. Wires running parallel to the z -axis were kept at high voltage. Charged particles traversing the gas volume caused ionization of the gas atoms. While the positive ions drifted to the cathode wires, the ionized electrons drifted to the anode wires, where they caused an avalanche of secondary electrons which gave a detectable signal. The average arrival time of the drift electrons was related to the distance at which the charged particle passed the wire. The amount of charge detected at the anodes was a measure of the amount of ionization produced by the particle in the TEC.

The TEC was divided into two parts. The inner chamber started at 8.5 cm from the beam axis and extended to 14.3 cm, and the outer chamber surrounded the inner one and extended to 46.9 cm. The length in z was 126 cm. The inner TEC consisted of 12 identical inner sectors, each contained 8 anode wires and covered 30° of the xy plane. The outer TEC was subdivided into 24 identical outer sectors each covering 15° of the xy plane, with 54 anode wires each. A plane of grid wires was placed at a distance of 3 mm on each side of the anodes. The difference in the number of sector divisions between the inner and outer TEC was used in the track reconstruction for solving left-right ambiguities. In addition, groups of left-right wires in the grid plane were read out on both sides

of the anode wires to resolve the remaining ambiguities. Tracks with polar angle $44^\circ < \theta < 136^\circ$ could reach all 62 wires, while a track with $\theta < 10^\circ$ or $\theta > 170^\circ$ missed the TEC completely.

The z coordinate of the charged track was measured by the Z Chamber, placed around the TEC. It consisted of two cylindrical proportional wire chambers with cathode strip readout. The Z Chamber allowed the precise measurement of θ in the barrel region ($45^\circ < \theta < 135^\circ$).

The endcap regions of the TEC were covered by proportional wire chambers, FTCs (Forward Tracking Chambers, installed in 1991), that allowed the measurement of the polar angle in this region. These two layers of cylindrical multiwire drift chambers measured position and direction of tracks in the forward direction: $12^\circ < \theta < 34^\circ$ and $146^\circ < \theta < 168^\circ$.

2.2.3 The Electromagnetic Calorimeter

The Electromagnetic Calorimeter (ECAL) was designed to measure precisely the direction and energy of photons and electrons (positrons). It was made of 10734 Bismuth Germanium Oxide ($B_4Ge_3O_{12}$ abbreviated as BGO) crystals pointing to the interaction region. In dense matter, electrons with an energy of at least an order of magnitude higher than the electron mass lose energy primarily through Bremsstrahlung, while photons with such energies mainly interact through pair creation. An electromagnetic shower occurs since these processes occur typically every radiation length (1.2 cm for BGO), resulting in an exponentially growing number of particles with smaller and smaller energies deeper in the material. When the critical energy is reached (about 10 MeV for BGO) the electron energy loss is dominated by ionization and excitation of the atoms in the crystal. This causes the atoms to emit green light, which was collected in photodiodes at the end of the crystals and converted into an electrical signal. This critical energy is much higher for other charged particles, so these only lose energy through ionization in the crystal. If such particles have an energy of about 1 GeV or higher, their energy loss becomes approximately independent of their initial energy, and they are called Minimum Ionizing Particles (MIPs). Hadronic particles lose a large fraction of their energy in a medium by nuclear interaction. These nuclear reactions took place inside the BGO, although with a much smaller probability than the Bremsstrahlung and pair processes for photons and electrons (positrons). Hence, hadrons on average lost only a small part of their energy in the BGO.

The BGO crystals used in this detector were 24 cm long (equivalent to 22 radiation lengths) and have a front-end surface of 2×2 cm², and a back-end surface of 3×3 cm². The barrel part covered the polar angular region $42^\circ < \theta < 138^\circ$, the endcap part $11.6^\circ < \theta < 36^\circ$ and $144^\circ < \theta < 168.4^\circ$ (Fig. 2.7). It must be noted that there was a gap of 7° in the coverage between the endcap and the barrel regions. An upgrade of the detector in 1995 added scintillator in

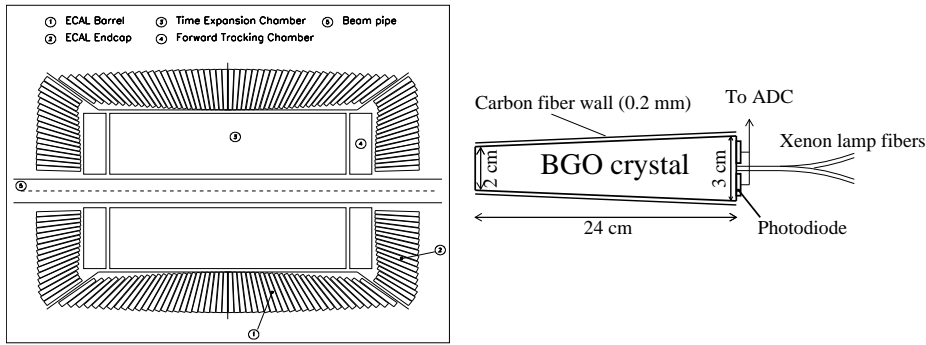


Figure 2.7: Left: the arrangement of the BGO crystals. Right: a BGO crystal.

the detector gap, which reduced this problem.

2.2.4 The Hadron Calorimeter

The Hadron Calorimeter (HCAL) was designed to measure the energy of hadrons. It was made of 5 mm thick depleted uranium plates interleaved with proportional wire chambers. The uranium plates acted as absorbers, while the proportional chambers enabled us to record the position of the hadron along its path through the calorimeter and to measure its energy by the total absorption technique. This technique means that hadrons cannot go through the calorimeter. It worked similarly to the ECAL except that there was a hadronic shower rather than an electromagnetic shower. Such a measurement was only effective if the hadron was totally absorbed in the calorimeter. Therefore, a high density material was required as an absorber and Uranium 238 fulfilled this requirement.

Like the ECAL, the HCAL also consisted of a barrel part, covering $35^\circ < \theta < 145^\circ$, and two endcap parts, covering $6^\circ < \theta < 35^\circ$ and $145^\circ < \theta < 174^\circ$. Both barrel and endcaps covered the whole azimuthal angle. The barrel consisted of 9 rings of 16 modules each; their length was 4.7 m and their outer diameter was 3.6 m. The three inner rings had an inner diameter of 1.78 m whereas the others had a diameter of 1.96 m. The endcaps each consisted of three separate rings (Fig. 2.8). The total amount of material traversed by a particle originating at the interaction point varies between 6 and 7 nuclear absorption lengths.

2.2.5 The Muon Detector

The muon detector was designed to measure muon momenta with a high precision. It was located between the magnet and the inner part of the detector, far from the interaction point. Only energetic muons (with momentum larger than 3 GeV) could reach this detector and be detected, other particles being

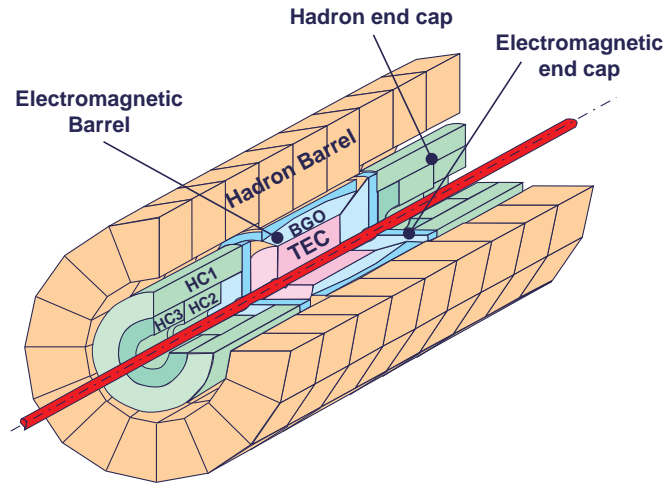


Figure 2.8: Perspective view of the Hadron Calorimeter.

totally absorbed by the material between the interaction point and the muon chambers. The system consisted of three layers of drift chambers, labeled from inside out as MI, MM, MO. The barrel part of the detector covered the polar angle range from 44° to 136° . It consisted of two halves with a gap at $z=0$. Each of the halves was subdivided into 8 octants, covering the region around the beampipe. Each octant contained five drift chambers (P-chambers) arranged in three layers (Fig. 2.9). The middle and outer layers were horizontally divided in two. The outer and inner chambers had 16 wires each, whereas the middle chambers contained 24 wires. P-chambers measured the curvature and hence the momentum of the muon track in the xy plane. To measure the z -coordinate of the muon track, the so-called Z-chambers were mounted on both the inside and the outside of each MI and MO chamber.

2.2.6 Other Detector Components

Apart from the major components discussed above, the L3 detector had several other important components. One of them was the luminosity monitor mounted near the beampipe in the very forward regions of the detector. It was responsible for precisely measuring the luminosity delivered by LEP by counting the number of small-angle Bhabha scattering events. Between HCAL and ECAL a series of large scintillating panels were installed to provide precise timing information, which was used, for instance, to reject cosmic rays and for triggering.

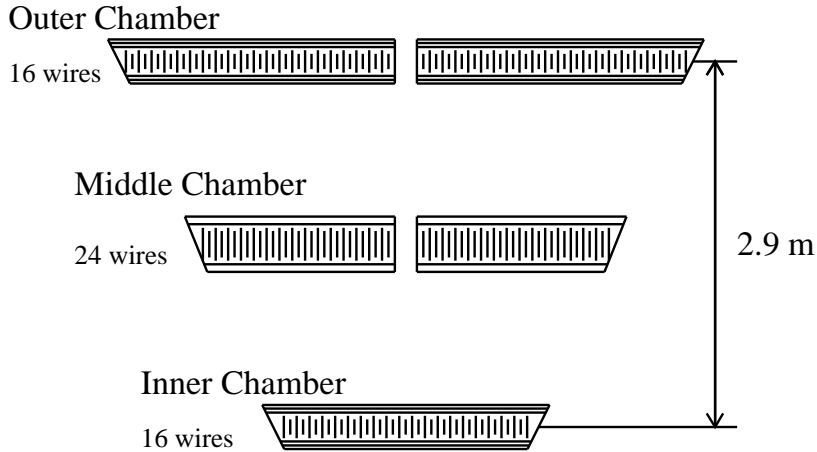


Figure 2.9: The 3-layer structure of a muon octant.

2.3 Hadronic Energy Measurements

As described in the previous section, the L3 detector consisted of various subdetectors. Signals from these subdetectors were related to the energy, momentum and identity of the particles crossing them. In spite of the calibration of the sub-detector components, several effects caused the measured energy to differ from the true energy of the particles. Firstly, the actual detector contained gaps and non-detecting materials such as wires, supports and amplifiers which caused non-detectable energy losses. Secondly, even calibrated subdetectors did not work perfectly. Thirdly, almost all neutrinos passed through the detector without detection. Finally, different parts of the detector have different response for different types of particle. Gain-factors (G -factors) were introduced to correct for these remaining losses.

The principal reason for G -factors is to minimize the total energy resolution. In terms of G -factors, the total visible energy of an event can be written as

$$E^{\text{cal}} = \sum_i G_i E_i, \quad (2.2)$$

where i labels different calorimeter geometrical regions shown in Fig. 2.10, G_i are the corresponding G -factors and E_i the energies deposited by charged particles in the calorimeter regions. The electromagnetic calorimeter consists of the regions 1, 7 and 9. The hadronic calorimeter regions are labeled 2, 3, 4, 6, 8 and 10. Region 5 is not shown since it corresponds to the active lead ring, which is not used in this analysis. Region 11 is assigned to the muon chambers and region 12 is assigned to the central tracking chamber (as summarised in Tab. 2.1).

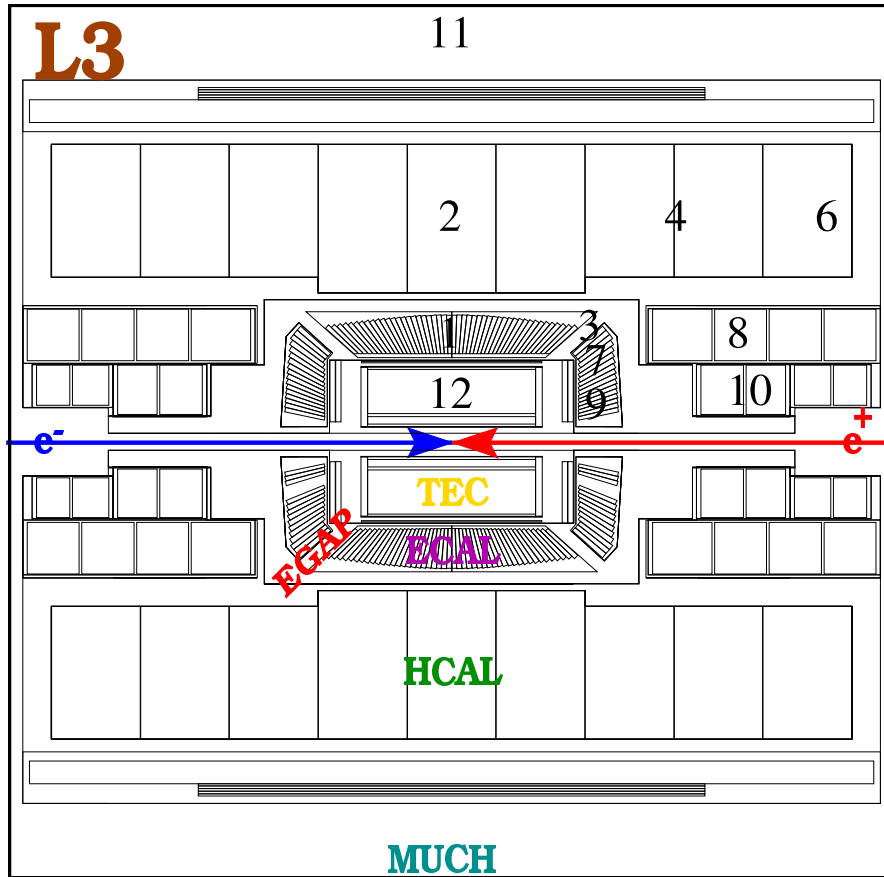


Figure 2.10: Labeling of different geometrical regions of the L3 detector.

Regions	Sub-detector
1, 7, 9	Electromagnetic Calorimeter
2, 3, 4, 6, 8, 10	Hadronic Calorimeter
11	Muon Chamber
12	Time Expansion Chamber

Table 2.1: Different regions of the L3 detector.

The G -factors are determined by minimizing the energy resolution of hadronic events while constraining the mean visible energy to the cms energy.

2.4 Data Processing

The various subdetectors measured variables which, in general, were very far from the physical quantities we are interested in. Therefore, it was necessary to translate information coming from a subdetector into more convenient variables which can be later used to perform data analysis.

There are three main areas of data processing: online triggering and data acquisition, off-line event reconstruction, and Monte Carlo event simulation. In addition, a database was maintained containing running conditions and the results of periodical calibration of the sub-detectors.

The next step is the reconstruction of the data, i.e., to translate the detector response into physical quantities of interest and to store this information on storage media for subsequent analysis.

The third step, the detector simulation, allows us to understand and to reproduce the response of the detector components.

2.4.1 Trigger System and Data Acquisition

The complete readout sequence of an event took about $500\mu\text{s}$ (corresponding to the time of 22 e^+e^- beam crossings), during which the detector could not process any new event. To reduce this dead time, a multi-level trigger system was implemented, which aborted the readout sequence as soon as possible if the beam crossing had not produced an event of interest.

The trigger system consisted of three levels: The role of the first level was to initiate the readout sequence if an e^+e^- collision was detected and to decide to keep it or not for further processing. The level-2 trigger was aimed at rejecting the most obvious background events, such as cosmic events, detector noise and interaction of the beam with residual gas or with the wall of the beampipe. The level-3 trigger used the full data information and was able to perform full reconstruction of the data. If an event was selected by the level-3 trigger, the digitized data obtained by the various subdetectors were collected, built into one set, and subsequently written onto tape.

2.4.2 Event Reconstruction

The data on tape essentially consist of a recording of the various signals emitted by the detector. Further processing is needed in order to convert this information

into the physical quantities we are interested in.

Firstly, information from the database such as calibration constants, alignment parameters, temperatures, and high voltages, is used to convert the digitized data to energy deposits, drift times, etc. Secondly, pattern recognition is performed for each subdetector. For example, crystal energies are converted to energy bumps (groups of BGO crystals containing energy deposits) and hits to tracks. Finally, tracks are matched to bumps in the ECAL and HCAL, and jet finding algorithms can be applied.

The data are stored in several formats. The data format used for physics analysis, the so-called DVN, contains only final objects such as tracks and energy bumps. The information of all individual channels of all subdetectors is kept on much larger sets of tapes, which can be used to re-process the data if better calibrations or reconstruction software become available.

2.4.3 Detector Simulation

Detectors are not perfect. There is always a certain level of noise present. Some parts may not be functioning well. The detectors have less than 100% acceptance. The detector has finite resolution. To study these problems and determine the efficiency and precision of a particular measurement, Monte Carlo (MC) simulations are used. These programs are built around the GEANT [44] package, which contains a detailed description of the interactions of the generated particles with any detector materials, as well as the effect induced by the various parts of the detector. Based on GEANT, a software package called SIL3 simulates the response of the L3 detector, including its resolution, to particles as they traverse the detector.

As input for the detector simulation program, MC models are used to describe final state particles of e^+e^- events according to our current knowledge of particle production in such reactions. In our work we use JETSET 7.4 [16] (including BE effects using the so-called BE_0 algorithm [45] and without BE effects) and HERWIG 5.9 [17].

After the detector simulation, one distinguishes two levels: “ideal” detector MC simulation and “real” detector MC simulation. The first one corresponds to the simulation of a time independent L3 detector for which all the various detector channels work at their maximum efficiency.

The real detector MC simulation is time dependent and the major changes in the detector during the period of data taking are incorporated. This can be the permanent loss of detection channels, such as a dead crystal of BGO, noisy electronic channels, or malfunctioning of the different subdetectors causing its inactivity. As for the TEC, the high voltage is permanently monitored during data taking in order to incorporate in the realistic simulation the loss of power in one or all sectors.

The generator-level and detector-level MC results are stored in the same formats (e.g., DVN) as used for the real data. One can thus compare measurable quantities at generator level of the MC to those at the detector level. In this way, it is possible to study the effects of the detector on these quantities.

Where detector simulation is not required, we also make use of PYTHIA 6.2 [46] and HERWIG 6.2 [47], the latter adapted to use the particle decay and BE routines of PYTHIA 6.2. Both generators make use of the BE₃₂ BE algorithm [45]. Parameters of all generators used have been tuned using L3 data [48].

Chapter 3

Event and Track Selection

The analysis presented here is based on data collected by the L3 detector in 1994 at a center-of-mass energy $\sqrt{s} \approx 91.2$ GeV. The data sample consists of almost two million hadronic Z decays. This 1994 run was the largest data sample at the Z peak recorded by the L3 detector.

Hadronic events produced in an e^+e^- reaction are selected by a two-step procedure. In the first step, one selects hadronic events and removes most of the background, using the energy measured in the electromagnetic and hadronic calorimeters. The second step of the selection is aimed at selecting good tracks measured with the Central Tracking Detector, in order to obtain the best reliability of data while keeping the number of tracks in the events as large as possible. Good agreement between data and MC simulation is essential to reconstruct the Bose-Einstein Correlation function, since this reconstruction depends on the description of the inefficiencies of the L3 detector, which are obtained from the simulations.

Figures in this chapter show the cuts (indicated by arrows) applied to reject events or tracks. The data are shown by dots and compared to events generated with JETSET 7.4 [16] (including BE effects) which have been passed through the L3 detector simulation program (see Sect. 2.4.3), reconstructed, and subjected to track and event selection in the same way as the data.

Our analysis is performed on sub-samples of two-jet and three-jet events as well as on the complete sample. The basic points of the procedure used to select two-jet as well as three-jet events are described in Sect. 3.4.

3.1 Event Selection

The background sources can be divided into two main categories: the first category consists of leptonic Z decays (e^+e^- , $\mu^+\mu^-$, $\tau^+\tau^-$). The second category,

called non-resonant background, contains sources such as two-photon interactions, as well as interactions of the beam with the wall of the beam pipe (beam-wall) or with residual gas inside the beam pipe (beam-gas) events.

The selection of hadronic events is based on the energy measured in the hadronic and electromagnetic calorimeters, with the purpose of rejecting as large as possible a fraction of background without influencing the measurement of the charged tracks in the TEC. Since two- and three-jet events will be selected using the energy of particles (see Sect. 3.4), this method, which largely decouples the event selection from the track selection, takes into account that the algorithm to determine the number of jets works more accurately when neutral as well as charged particles are used.

After having removed calorimeter clusters with energy deposit smaller than 100 MeV, events originating from leptonic Z channels, as well as beam-wall, beam-gas and two-photon events are excluded by requiring that events fulfill the following criteria:

$$0.5 < \frac{E^{\text{cal}}}{\sqrt{s}} < 1.5, \quad (3.1)$$

$$\frac{E_{\perp}^{\text{cal}}}{E^{\text{cal}}} < 0.6, \quad (3.2)$$

$$\frac{E_{\parallel}^{\text{cal}}}{E^{\text{cal}}} < 0.4, \quad (3.3)$$

$$N_{\text{clus}} > 14, \quad (3.4)$$

$$|\cos(\Theta_{\text{th}}^{\text{cal}})| < 0.743, \quad (3.5)$$

where the total visible energy of an event, E^{cal} , is defined as the sum of the N_{clus} cluster energies E_i^{cal} . In a similar manner we define the vectorial energy sum \mathbf{E}^{cal} , obtained by summing the cluster energy along the direction of the cluster as seen from the interaction point, \mathbf{n}_i :

$$E^{\text{cal}} = \sum_i E_i^{\text{cal}} \quad \text{and} \quad \mathbf{E}^{\text{cal}} = \sum_i E_i^{\text{cal}} \cdot \mathbf{n}_i. \quad (3.6)$$

We also define the longitudinal and transverse energy imbalance, $E_{\parallel}^{\text{cal}}$ and E_{\perp}^{cal} , as the projection of \mathbf{E}^{cal} along the z axis and in the plane perpendicular to the z axis, respectively:

$$E_{\parallel}^{\text{cal}} = |E_z^{\text{cal}}| \quad \text{and} \quad E_{\perp}^{\text{cal}} = \sqrt{(E_x^{\text{cal}})^2 + (E_y^{\text{cal}})^2}. \quad (3.7)$$

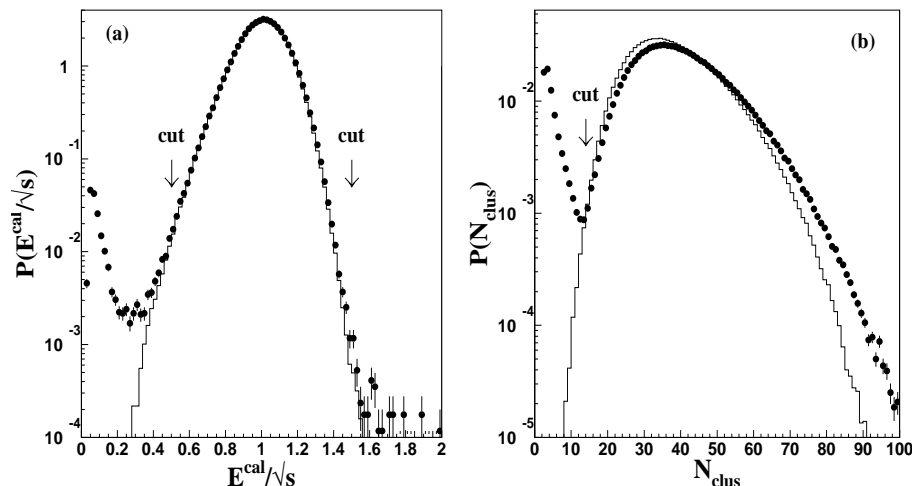


Figure 3.1: (a) Distribution of the visible energy scaled to \sqrt{s} , after application of the other cuts (3.2) – (3.5), (b) distribution of cluster multiplicity of events, after application of the other cuts (3.1) – (3.3) and (3.5). Dots correspond to the data, lines to the Monte Carlo simulation.

Both the sum of energy components along the beam direction and in the plane perpendicular to the beam direction should ideally be zero for hadronic Z decay events. This is because at LEP the laboratory frame is also the center-of-mass frame. We also define $\Theta_{\text{th}}^{\text{cal}}$, which is the polar angle of the event thrust axis determined from the calorimeter clusters.

The limited acceptance, beam-gas and beam-wall interaction events, two-photon events and poor track measurements give rise to parallel and perpendicular energy imbalances. Therefore cuts (3.2) and (3.3) suppress beam-gas, beam-wall and two-photon interactions.

Cuts on the visible energy

Hadronic Z events are characterized by a visible energy centered around the center-of-mass energy, \sqrt{s} . The lower cut of Eq. (3.1) is applied to reject non-resonant background events, such as beam-wall, beam-gas and two-photon events, since typically they have much lower visible energy. The purpose of the upper cut is to remove Bhabha events which are located at scaled energy higher than 1.5 because of the scaling factors (G -factors), which are appropriate only for hadronic events. Fig. 3.1 (a) shows the distribution of the visible energy after application of the other cuts (3.2) – (3.5).

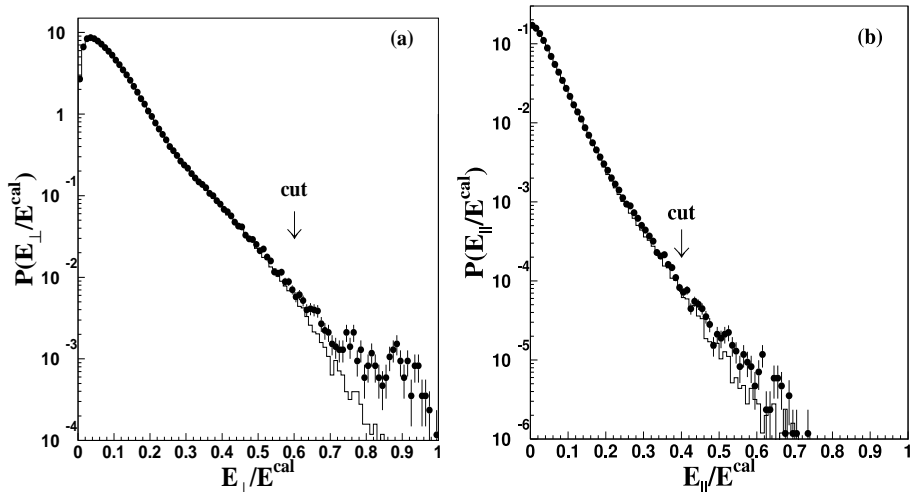


Figure 3.2: (a) Transverse and (b) longitudinal energy imbalance for the data (dots) and for the Monte Carlo simulation (line), after application of cuts (3.1), (3.3) – (3.5) and (3.1), (3.2), (3.4), (3.5), respectively.

Cut on the number of clusters

Hadronic events usually have a larger multiplicity than other processes. Hence, a low-multiplicity cut removes background contaminations such as $Z \rightarrow e^+e^-$, $\mu^+\mu^-$, $\tau^+\tau^-$ and beam-gas events. By requiring that events have at least 14 clusters, Eq. (3.4), most of the background is eliminated.

The distribution of the number of clusters after application of cuts (3.1) – (3.3) and (3.5) is shown in Fig. 3.1 (b). The peak at low multiplicity, which clearly comes from background contamination, is removed using this cut.

Cuts on the energy imbalance

Since at LEP the laboratory frame for e^+e^- collisions coincides with the center-of-mass frame, hadronic events are well balanced in energy. However, interactions of a beam electron with residual gas or with the beam pipe result in large energy imbalances. Also, two-photon interactions result in energy imbalance since one or both of the final-state electrons usually are produced at small angle and hence remain within the beam pipe and are not detected. Hence, cuts Eq. (3.2) and (3.3) are used to reject these background events. As shown in Fig. 3.2 after the other cuts have been applied, we require the transverse energy imbalance E_{\perp}^{cal} to be smaller than 0.6 and the longitudinal energy imbalance $E_{\parallel}^{\text{cal}}$ to be smaller than 0.4 of E^{cal} , where the simulation and data agree well.

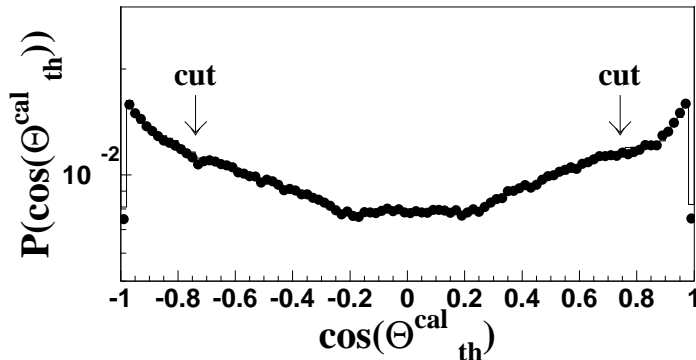


Figure 3.3: Distribution of $\cos(\Theta_{th}^{cal})$ for the data (dots) and for the Monte Carlo simulation (line), after application of cuts (3.1) – (3.4).

Cut on the direction of the thrust axis

Since information is used from TEC and SMD, events are required to be well contained within their acceptance. To achieve this, cut (3.5) is applied. The distribution of the polar angle of the event thrust axis after cuts (3.1) – (3.4) have been applied is shown in Fig. 3.3.

3.2 Track Selection

After the event selection, criteria have to be defined to select tracks which are well reconstructed in the central tracker. There are a number of parameters on the basis of which one can decide if a track is good or not. The TEC based selection criteria of charged particles are summarized here:

$$p_t > 150 \text{ MeV}, \quad (3.8)$$

$$N_{\text{innerhit}} \geq 1, \quad (3.9)$$

$$N_{\text{hit}} > 25, \quad (3.10)$$

$$N_{\text{span}} > 40, \quad (3.11)$$

$$\text{DCA} < 10\text{mm}, \quad (3.12)$$

$$45^\circ < \phi < 52.5^\circ \text{ and } 225^\circ < \phi < 232.5^\circ. \quad (3.13)$$

The quantities used to determine the goodness of tracks are described below.

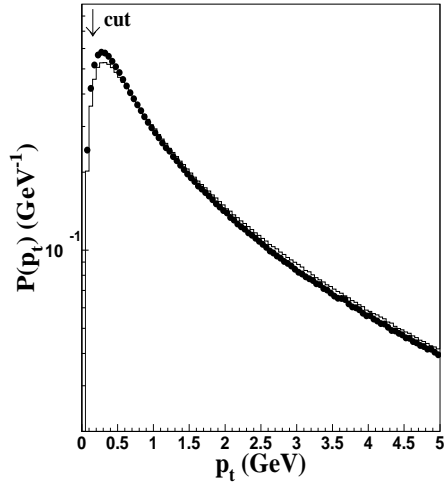


Figure 3.4: Distribution of track transverse momenta for the data (dots) and for the Monte Carlo simulation (line), after application of the other cuts (3.9) – (3.13).

Cut on the transverse momentum, p_t

The transverse momentum of a track is measured from its curvature in the plane perpendicular to the beam axis. Tracks having low transverse momentum p_t cannot cross the TEC and therefore cannot be measured accurately. Besides, tracks with low transverse momentum suffer greatly from multiple scattering leading to poor resolution. To minimize the reconstruction error, tracks are required to have p_t larger than 150 MeV.

Cuts on the number of hits and on the span

When a charged particle passes through the TEC, it causes ionization in the gas of the chamber. The consequent signal on an anode wire of the chamber is called a “hit”. The TEC has 62 wires: 8 wires in the inner TEC and 54 in the outer TEC. Hence, a charged particle can have a maximum of 62 hits. The larger the number of hits, the better is the resolution of the transverse momentum, since the transverse momentum is calculated from the curvature of the track path formed by the subsequent hits.

The so-called span is defined as the number of wires from the first to the last hit (including the first and last hits) and is a measure of the length of the track. Note that the number of hits and span are strongly correlated and both affect the momentum resolution. The larger the number of hits and the span, the better is the resolution of the transverse momentum, since the curvature is calculated from the path drawn by the subsequent hits.

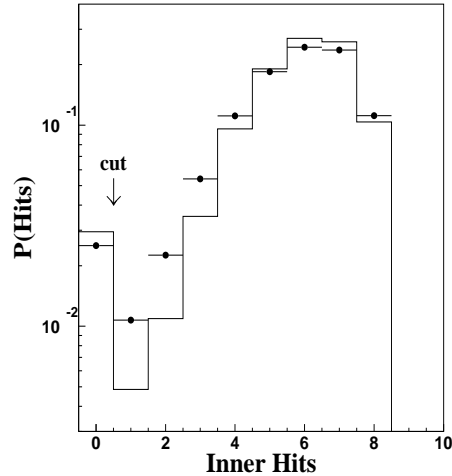


Figure 3.5: Distribution of the number of hits in the inner TEC for the data (dots) and for the Monte Carlo simulation (line), after application of the other cuts: (3.8) and (3.10) – (3.13).

A misreconstructed track usually has a small number of hits. Besides, the absence of any hit in the inner TEC increases strongly the probability of misreconstruction of a track since the left-right ambiguity of the outer TEC cannot be resolved. Therefore, every track is required to have at least one hit in the inner TEC (Fig 3.5).

Fig. 3.6 (a) shows the distribution of the number of hits caused by data and Monte Carlo simulation requiring one hit in the inner TEC and applied cuts (3.8), (3.11) – (3.13). There is a clear discrepancy between these distributions mainly due to the MC overestimation of hits in the inner TEC. The cut is chosen to lie in the middle of a region of the distribution where the variation of the disagreement between data and Monte Carlo is stable and no big change from bin to bin in this disagreement is expected. Hence, the number of hits in the TEC is required to be at least 25. Loss in track momentum resolution, which could result from the use of such a low minimum requirement, is minimized by the previous requirement of at least one hit in the inner TEC and by the choice of a rather large span.

Sometimes, hits belonging to two different tracks can be reconstructed as one track. Since these tracks usually have a smaller length than well reconstructed tracks, it is possible to remove most of these tracks by requiring a minimum length for each track. Since we are interested in the curvature of the tracks, a certain minimum value of the length of the tracks is required. All tracks are required to have a span of at least 40 to reject misreconstructed tracks after applying the cuts (3.8) – (3.10), (3.12) and (3.13), shown in Fig. 3.6 (b).

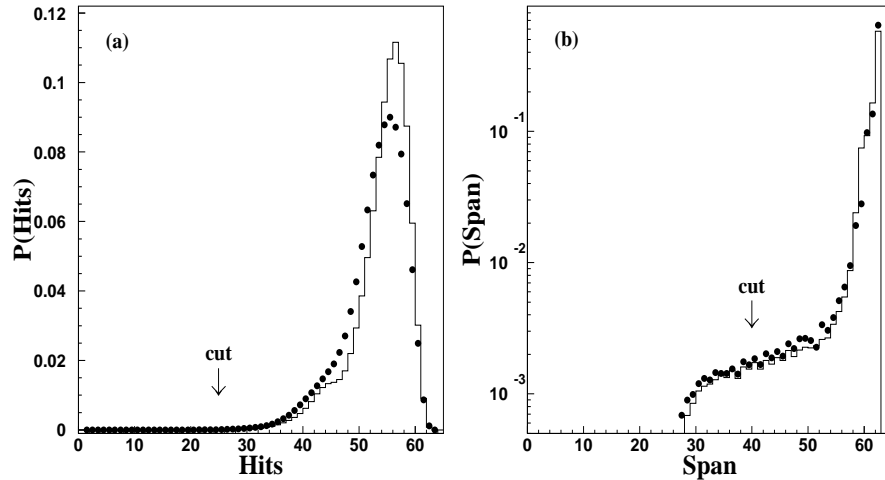


Figure 3.6: Distribution of the number of (a) hits in the whole TEC, after application of the other cuts (3.8), (3.9), (3.11) – (3.13), and of (b) the span of tracks after application of the other cuts (3.8) – (3.10), (3.12) and (3.13). The dots correspond to the data and the histograms correspond to the Monte Carlo simulation.

Cuts on the distance of closest approach

A good track must have a high probability of coming from the interaction point and not being a cosmic ray crossing the tracker or a stray beam particle. A track can be extrapolated back to the vertex. The distance of closest approach (DCA) to the interaction vertex is calculated in the plane transverse to the beam axis. The sign of the DCA depends on whether the interaction point lies inside (negative) or outside (positive) the curve of the trajectory. For a sample of tracks coming from the vertex one would expect a distribution symmetric about zero. Fig. 3.7 shows the distribution of the DCA after applying the other cuts (3.8) – (3.11) and (3.13). In order to ensure that a track originates at the interaction point, tracks are required to have a DCA less than 10 mm. The DCA cut is deliberately very wide to have maximum statistics.

Cuts on azimuthal track angle

As shown in Fig. 3.8 after applying the previously mentioned cuts (3.8) – (3.12), large discrepancies appear between data and Monte Carlo in the azimuthal distribution for two regions: $45^\circ < \phi < 52.5^\circ$ and $225^\circ < \phi < 232.5^\circ$. This is due to a wrong simulation of inefficiencies of the corresponding TEC sectors. Therefore, tracks from these regions are removed from the analysis.

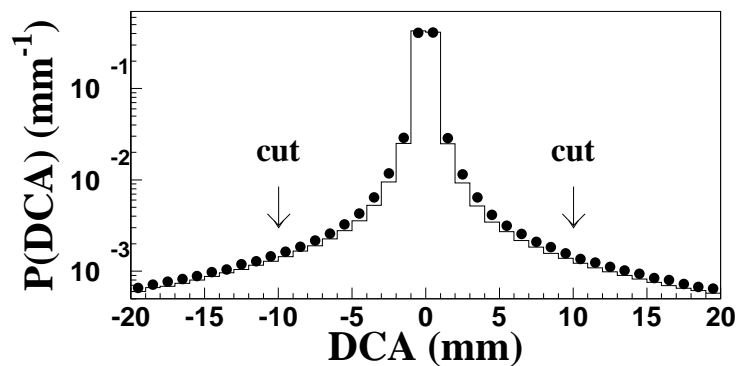


Figure 3.7: Distance of closest approach of tracks for the data (dots) and for the Monte Carlo simulation (line) after application of the other cuts (3.8) – (3.11) and (3.13).

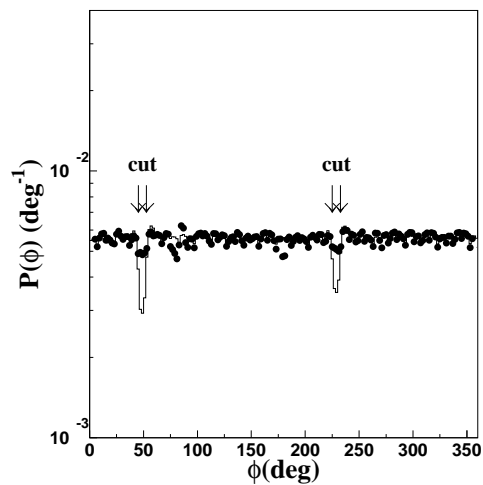


Figure 3.8: Distribution of the azimuthal track angle ϕ for the data (dots) and for the Monte Carlo simulation (line), after application of the other cuts (3.8) – (3.12).

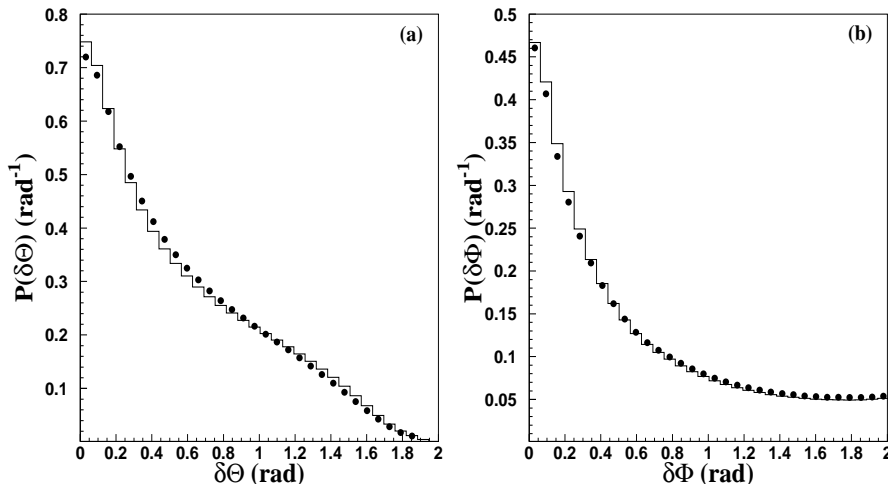


Figure 3.9: Distribution of the difference between two tracks in (a) the polar and (b) azimuthal angle with respect to the beam direction. Dots correspond to the data, lines to the Monte Carlo simulation, after event and track selection.

Additional cuts to improve resolution

The resolution of the opening angle between a pair of tracks is crucial for the study of BEC. For this reason, additional cuts on tracks are imposed to reject a track when no hit in the Z-chamber is found and an energy deposit in the BGO is used to recover this missing hit. After this cut, there is good consistency between data and MC simulation for the difference between two tracks in the polar and azimuthal angles with respect to the beam direction (see Fig. 3.9).

3.3 Further Event Selection

Although we have already applied a hadronic event selection based on calorimeter clusters, two additional cuts are imposed in order to increase the purity of the hadronic sample and the precision of track measurement. Note that these additional cuts are not applied in the figures of the previous two subsections.

Firstly, to reject the residual $\tau^+\tau^-$ background, selected events are required to have their second largest angle, ϕ_2 , between any two neighboring tracks in the $r\phi$ plane, between 20° and 170° (Fig. 3.10).

Secondly, events are required to have their thrust axis, calculated using only charged tracks, in the barrel of the TEC: $|\cos(\theta_{\text{thr}}^{\text{TEC}})| < 0.7$, where $\theta_{\text{thr}}^{\text{TEC}}$ is the polar angle of the event thrust axis determined from the charged tracks.

Together with all of the previous cuts, the number of events remaining is

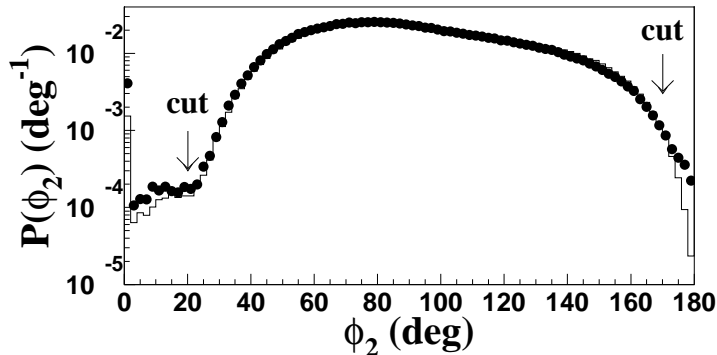


Figure 3.10: Distribution of the second largest angle, ϕ_2 , for the data (dots) and for the Monte Carlo simulation (line), after event and track selection.

about 0.8 million with an average number of charged tracks of about 12.

3.4 Two-jet and Three-jet Event Selection

Besides the full event sample, we also use two-jet and three-jet event subsamples. The jet algorithms most commonly used in studies of e^+e^- annihilation are the JADE [49] and the Durham [50] algorithms. For a review of these and other jet algorithms see [51]. For a review of the Monte Carlo generators and their connections with the jet algorithms see [52].

In the JADE algorithm, one considers all possible pairs (i, j) of particles in the final state, with energies E_i, E_j , and angular separation Θ_{ij} and computes the jet resolution variable

$$y_{ij} = y_{ij}^J = \frac{2E_i E_j (1 - \cos \Theta_{ij})}{E_{\text{cal}}^2}. \quad (3.14)$$

The pair having the smallest value of y_{ij} is combined into a new pseudo-particle k of four-momentum

$$p_k = p_i + p_j, \quad (3.15)$$

provided that $y_{\text{cut}} \leq y_{ij}$. The algorithm is then reiterated using the new set of (pseudo)particles and it stops when, for all pairs, $y_{ij} \geq y_{\text{cut}}$. The pseudoparticles at the end of the algorithm are called jets. The number of jets, therefore, depends on y_{cut} .

A drawback of the definition (3.14) is that also particles at very different angles can be recombined into one pseudoparticle. This is due to the fact that $2E_i E_j (1 - \cos \Theta_{ij}) \approx M_{ij}^2$, where M_{ij}^2 is the invariant mass of the two particles. On the experimental side the trouble is that ghost jets may appear, i.e. jets along

directions where no particles are present. To cure this problem the Durham algorithm was introduced. It works in the same way as JADE but uses the definition

$$y_{ij} = y_{ij}^D = \frac{2\min\{E_i^2, E_j^2\}(1 - \cos \Theta_{ij})}{E_{\text{cal}}^2} \quad (3.16)$$

instead of (3.14). The resolution criterion $y_{ij}^D > y_{\text{cut}}$ becomes, for small angles, $p_{ti}^2 > E_{\text{cal}}^2 y_{\text{cut}}$, where p_{ti} is the transverse momentum of the i -th particle with respect to the direction of the j -th one. In this way the algorithm tries to minimize the transverse momentum rather than the invariant mass.

In our work, the Durham algorithm is used to select two- and three-jet events, and JADE is used to determine part of the systematic uncertainties.

The number of two-jet events, using the Durham algorithm with $y_{\text{cut}} = 0.006$, is about 450k with an average number of charged tracks of about 10. All events which are not selected as two-jet events are considered as three-jet events. The number of three-jet events is about 350k with an average number of charged tracks of about 14.

Chapter 4

Introduction to Bose-Einstein Correlations

In this chapter, the historical and theoretical background relevant to this thesis is given and the basic formalism is defined. Various parametrizations are discussed using different variables and assuming different source functions such as Gaussian or Lévy. The fit results of these parametrizations will be presented in the next chapter. After having established the theoretical correlation function, we discuss how to measure it experimentally. Special attention will be paid to the mixing procedure applied to build the reference sample needed for the construction of the correlation function, as well as to the unfolding of the data for detector related effects, such as acceptance, resolution and particle misidentification.

4.1 Theory

The usual derivation of the BE effect begins with the observation of an interference between two identical bosons, e.g., pions. Two detectors located at X_1 and X_2 detect pions with momentum p_1 and p_2 , respectively. The probability amplitude for observing at space-time point X_1 a pion with four-momentum p_1 originating at a space-point x_1 is

$$\Psi(1) = e^{i\phi_1} e^{ip_1(x_1 - X_1)}, \quad (4.1)$$

where ϕ_1 is the phase of the pion. Thus, the joint probability amplitude for the observation of two distinguishable pions from x_1, x_2 detected at X_1 and X_2 with momentum p_1 and p_2 is

$$\Psi^D(1, 2) = \left(e^{i\phi_1} e^{ip_1(x_1 - X_1)} \right) \left(e^{i\phi_2} e^{ip_2(x_2 - X_2)} \right). \quad (4.2)$$

Here interactions between the two pions are neglected, so that the two-particle amplitude is the product of the two single-particle amplitudes. For indistinguishable bosons, the amplitude must be symmetric under the exchange of the emission points:

$$\Psi(1, 2) = \frac{e^{i\phi_1+i\phi_2}}{\sqrt{2}} \left(e^{ip_1(x_1-X_1)} e^{ip_2(x_2-X_2)} + e^{ip_1(x_2-X_1)} e^{ip_2(x_1-X_2)} \right). \quad (4.3)$$

The reason for using this symmetrization is that the observer cannot decide from which source a particular pion was emitted, so that both possibilities have to be taken into account. If the particle emission is coherent, then

$$\Psi^C(1, 2) = e^{i\phi} e^{-ip_1 X_1 - ip_2 X_2}, \quad (4.4)$$

as emission from x_1 and x_2 appears at the detection X_1 and X_2 in phase, so only an overall phase $\phi \equiv \phi(X_1, X_2)$ is present. However, if the particle emission is completely incoherent, as would be the case for fully chaotic particle production, then the phase of emission is a uniformly distributed random variable at each point of emission, and the phase depends also on the path from x_1 and x_2 to the detector at X_1 and X_2 .

The two-particle correlation function C_2 is defined as

$$C_2(1, 2) = \frac{|\Psi(1, 2)|^2}{|\Psi(1)|^2 |\Psi(2)|^2}, \quad (4.5)$$

where $\Psi(i)$ ($i = 1, 2$) is the wave function for pion i . If the emission is completely incoherent, as would be the case for fully chaotic particle production, the arbitrary phases are unrelated and drop out yielding

$$C_2(1, 2) = 1 + \cos(\Delta p \Delta x), \quad (4.6)$$

where $\Delta p = p_1 - p_2$ is the four-momentum difference of the two pions, and $\Delta x = x_1 - x_2$ is the initial space-time difference of the two pion emission points. On the other hand, if the emission is completely coherent, $C_2(1, 2) = \frac{|\Psi^C(1, 2)|^2}{|\Psi(1)|^2 |\Psi(2)|^2} = 1$.

The second step is to assume that the pion emission points x_1 and x_2 are randomly distributed in the region of space-time and that the source is static, i.e. specified by a density distribution $f(x)$ and a momentum distribution $\rho(p)$, which are normalized as $\int dx f(x) = 1$ and $\int dp \rho(p) = \langle n \rangle$, respectively. In this case the source function can be factorized: $S(x, p) = \rho(x) f(p)$. Then the single-particle spectrum is

$$E \frac{d^3 n}{d^3 p} = \int dx S(x, p) |\Psi(1)|^2 = \rho(p) \int dx f(x) = \rho(p), \quad (4.7)$$

and the two-particle spectrum is

$$E_1 E_2 \frac{d^6 n}{d^3 p_1 d^3 p_2} = \int dx_1 dx_2 S(x_1, p_1) S(x_2, p_2) |\Psi(1, 2)|^2. \quad (4.8)$$

The correlation function of observing two identical pions with momenta p_1 and p_2 is obtained via

$$C_2(p_1, p_2) = \frac{\frac{d^6 n}{d^3 p_1 d^3 p_2}}{\frac{d^3 n}{d^3 p_1} \frac{d^3 n}{d^3 p_2}} = \frac{\int d^4 x_1 d^4 x_2 f(x_1) f(x_2) |\Psi(1, 2)|^2}{\int d^4 x_1 |\Psi(1)|^2 \int d^4 x_2 |\Psi(2)|^2}. \quad (4.9)$$

For the case of coherent emission, $C_2 = 1$, while for completely incoherent (i.e. fully chaotic) emission,

$$C_2(p_1, p_2) = 1 + |\tilde{f}(\Delta p)|^2, \quad (4.10)$$

where $\tilde{f}(\Delta p)$ is the Fourier transform of $f(x)$,

$$\tilde{f}(\Delta p) = \int dx \exp(i\Delta p \cdot x) f(x). \quad (4.11)$$

The second term of Eq. (4.10) is the consequence of the BE interference between the two parts of the amplitude in Eq. (4.3) and the assumption of complete chaoticity. From Eq. (4.10) we see that $C_2(p_1, p_2) - 1$ measures the absolute square of the Fourier transform $|\tilde{f}(\Delta p)|^2$ of the pion source distribution in configuration space. This is the basis of the expectation that the intensity interference pattern can be used to extract information on the space-time structure of the pion source.

Having thus reviewed the simplest, but frequently used, derivation of the BE effect, we can now highlight the deficiencies in this derivation.

Firstly, a serious criticism is that this derivation assumes a static pion source. An early model including time dependence was suggested by Kopylov and Podgoretski [53, 54], in the framework of a simple model of a radiating spherical surface of radius R with incoherent point-like oscillators of life-time τ , namely

$$C_2(p_1, p_2) = 1 + \frac{I^2(q_T R)}{1 + (q_0 \tau)^2}, \quad (4.12)$$

where the variable q_0 is the pion energy difference, q_T is the projection of the three-momentum difference onto the plane perpendicular to the sum of the two three-momenta. The numerator is given in terms of $I(q_T R) = 2J_1(q_T R)/q_T R$, where J_1 is the first Bessel function. Like Eq. (4.10), this modified correlation function has the value of 2 at the origin and tends to unity as the magnitude of Δp increases.

Secondly, the multiparticle nature of the final hadronic state is not considered properly. Here, only two-particle pion wave functions are used, although in general, a coherent superposition of multipion wave functions (and hence, a nontrivial multiplicity distribution) must describe the final hadronic state. Techniques have been developed to calculate multiparticle BE interference to all orders, see, e.g., [55, 56].

Thirdly, it is experimentally observed that, using different parametrizations of the correlation function, the measured correlation functions do not reach the

expected maximum value of 2 at vanishing momentum difference. To accommodate this, an extra parameter λ is introduced [57], which describes the fraction of effectively interfering pion pairs:

$$C_2(p_1, p_2) = 1 + \lambda |\tilde{f}(\Delta p)|^2. \quad (4.13)$$

Now the interpretation of this formula becomes even more difficult. The parameter λ quantifies more or less the level of ignorance of the strength of the correlation. It can be different from unity for several reasons. Some bosons, e.g., from decay of long lived resonances, do not interfere on the experimentally resolvable scale [58]. It is also possible, that bosons are emitted from the source partially coherently. In that case not two but three terms are contained in the correlation function. Experimentally, particle pairs can be misidentified as identical. Furthermore, the experimental resolution may be insufficient to measure small momentum differences, so that the estimate of the $\Delta p \rightarrow 0$ behavior of the correlation function relies on an extrapolation.

Fourthly, in this simple derivation, R_2 only depends on the momentum difference between the two pions. In general, R_2 is defined in a six-dimensional momentum space: three components coming from the momentum difference between the two pions and three components coming from their momentum sum. Indeed, application of the general Wigner formalism [59] to BEC [60, 61] allows for a dependence on the momentum sum, $K = \frac{1}{2}(p_1 + p_2)$, as well. In this formalism, the theoretical approximation of R_2 reads [61]

$$R_2(\Delta p, K) \approx 1 + \frac{|\int d^4x S(x, K) \exp(i\Delta p \cdot x)|^2}{|\int d^4x S(x, K)|^2}, \quad (4.14)$$

where the emission function $S(x, K)$, which is related to the single-particle number density, is the probability of emission of a boson from space-time point x with momentum K .

Finally, the question of final-state interactions, e.g., Coulomb and strong interactions, has not been addressed. In [61, 62] the correlation function is calculated considering these interactions, but the effect is small for e^+e^- annihilation and is neglected in our analysis.

Apart from all of these theoretical problems, there are also some experimental difficulties in measuring BEC, such as track losses, particle misidentification, resolution problems, resonances, etc., as detailed in Sect. 4.3.

4.2 Bose-Einstein Correlation Function

The correlation function of two particles with four-momenta p_1 and p_2 is given by the ratio of the two-particle number density, $\rho_2(p_1, p_2)$, to the product of the two single-particle number densities, $\rho_1(p_1)\rho_1(p_2)$. Since we are interested

here only in the correlation R_2 due to Bose-Einstein interference, the product of single-particle densities in C_2 is replaced by $\rho_0(p_1, p_2)$, the two-particle density that would occur in the absence of Bose-Einstein correlations, yielding:

$$R_2(p_1, p_2) = \frac{\rho_2(p_1, p_2)}{\rho_0(p_1, p_2)}. \quad (4.15)$$

Note that ρ_0 is defined and normalized in the same way as ρ_2 . It is frequently referred to as the density of the ‘reference sample’. Since this sample does not exist in nature, we attempt to create it ourselves (see Sect. 4.3.1).

Since the mass of the two identical particles of the pair is fixed to the pion mass, the correlation function is defined in six-dimensional momentum space. Since Bose-Einstein correlations can be large only at small four-momentum difference $Q = \sqrt{-(p_1 - p_2)^2}$, they are often parametrized in this one-dimensional distance measure:

$$R_2(Q) = \frac{\rho_2(Q)}{\rho_0(Q)}. \quad (4.16)$$

There is no reason, however, to expect the hadron source to be spherically symmetric in jet fragmentation. Recent investigations have, in fact, found an elongation of the source along the jet axis [63–66]. While this effect is thus well established, the elongation is actually only about 20%. In e^+e^- annihilation at lower energy [67] it has been observed that Q is the appropriate variable. We check this in Sect. 5.3 and confirm that this is indeed the case also for e^+e^- annihilation at the Z peak.

This is not the case in heavy-ion and hadron-hadron interactions, where BEC are found not to depend simply on Q , but on the components of the four-momentum difference separately [31, 68, 69].

Since BEC works only at small values of Q , we only consider a certain region of phase space and thus only a certain region of the source in space-time. Therefore, we will from now on speak about the “region of homogeneity”, i.e., the region over which BE interference takes place [70]. This is the region where particles with a given momentum are emitted from. This region of homogeneity is generally smaller than the whole source.

4.3 Determination of R_2

After determining $\rho_2(Q)$ in the raw data, there are three steps in obtaining R_2 . The first step is to create the reference sample, and from it to determine $\rho_0(Q)$. Then two corrections must be determined and applied, one for non-BE correlations lost in forming the reference sample and the other for detector effects.

4.3.1 The Reference Sample

The reference sample, ρ_0 , should include all correlations, such as energy-momentum conservation and correlations due to resonance decays, except those of BE. Since such a sample does not occur in nature, different methods have been developed to construct it.

Three methods to determine the reference sample are the following:

- The reference sample is formed by means of event mixing. In this case, the four-momentum difference is computed between two tracks coming from different randomly selected events of similar multiplicity. This removes the BE correlations while retaining other characteristics of the data sample. The main problem with this method is that it removes more correlations than just BE. This effect is estimated and corrected by MC.
- In the second method, the reference sample is formed by computing Q for unlike-sign particle pairs. Since BEC only occur between identical bosons, it would be a good reference sample except that other correlations are also different for like- and unlike-sign pairs. In particular, resonances like ρ^0 and ω , which are neutral, decay to pions, creating correlations between unlike-sign particles but not between like-sign particles. Thus this method introduces a bias.
- In the third method, the reference sample is formed by Monte Carlo simulation without BEC. In this case, one has to assume that the MC describes the data in all aspects except for the BEC.

In this analysis, the reference sample is formed by using mixed events which are created in the following way. First, events are rotated to a system with the z -axis along the thrust axis and are stored in a ‘pool’. Then, an event is randomly selected from this pool and its tracks are replaced by tracks of the same charge from other randomly selected events in the pool having approximately the same multiplicity, under the condition that no two tracks originate from the same event. After this procedure, the ‘mixed’ event consists of tracks originating from different events in the pool. The randomly selected event is replaced by a new event from outside the pool, thus preventing any regularities in the reference sample. Finally, Q is calculated for each pair of tracks in the mixed events. From this mixed sample we obtain the particle density $\rho_{\text{mix}}(Q)$.

4.3.2 Corrections

Since the mixing procedure removes not only Bose-Einstein but also other correlations, e.g., those from energy-momentum conservation and from resonances, the resulting density ρ_{mix} is corrected by a factor C_{mix} . This factor is estimated by Monte Carlo simulation using a generator without BEC effects. Thus, in the

absence of Bose-Einstein correlations, the two-particle density of the reference sample is given by

$$\rho_0(Q) = \rho_{\text{mix}}(Q) \cdot C_{\text{mix}}(Q), \text{ where } C_{\text{mix}}(Q) = \left[\frac{\rho_2(Q)}{\rho_{\text{mix}}(Q)} \right]_{\text{MC, noBE}}. \quad (4.17)$$

The ratio $(\rho_2/\rho_{\text{mix}})$ must further be corrected for detector resolution, acceptance and efficiency and for particle misidentification. For this correction we use a multiplicative factor derived from Monte Carlo studies. Since the L3 detector does not identify hadrons, this factor, C_{det} , is given by the ratio of the two-pion correlation function found from MC events at generator level to the two-particle correlation function found using all particles after full detector simulation, reconstruction and event and track selection:

$$C_{\text{det}}(Q) = \left(\frac{\rho_2(Q)}{\rho_{\text{mix}}(Q)} \right)_{\text{gen, pions}} / \left(\frac{\rho_2(Q)}{\rho_{\text{mix}}(Q)} \right)_{\text{det, all}}. \quad (4.18)$$

Taking all charged particles, instead of only pions, in the generator level MC, leads to consistent results. Combining this correction factor with (4.15) and (4.17) results in

$$R_2(Q) = \frac{\rho_2(Q)}{\rho_{\text{mix}}(Q)} \cdot \frac{1}{C_{\text{mix}}(Q)} \cdot C_{\text{det}}(Q). \quad (4.19)$$

The analysis is done in bins of Q . In terms of numbers N_k of like-sign particle pairs in bin k of Q , Eq. (4.19) becomes

$$R_{2k} = \left[\frac{N_k}{N_k^{\text{mix}}} \right]_{\text{data}} \cdot \left[\frac{N_k^{\text{mix}}}{N_k} \right]_{\text{MC, noBE}} \cdot \left[\frac{N_k^{\text{gen}}}{N_k^{\text{gen, mix}}} \cdot \frac{N_k^{\text{det, mix}}}{N_k^{\text{det}}} \right]_{\text{MC}}. \quad (4.20)$$

Each N_k is normalized to the total number of pairs in the corresponding sample.

The resolution in the variable Q depends on Q itself and is estimated using Monte Carlo events to be 0.02–0.05 GeV for $Q < 0.2$ GeV. Given the available statistics, we choose a bin size of 0.04 GeV.

In our analysis, we use JETSET without BEC to determine the mixing correction factor C_{mix} and JETSET with BEC to determine the detector correction factor C_{det} .

4.4 The Longitudinal Center-of-Mass System

To study the region of homogeneity in more than one dimension, it is important to decouple the energy difference (and therefore the difference in emission time of Fourier transformed space) of the particles from the difference in momentum components (and therefore the difference in purely spatial components in Fourier transformed space).

In our work the longitudinal center-of-mass system (LCMS) [71] is used. This system is defined for each pair of particles as that system in which the sum of their momenta is perpendicular to the thrust axis \mathbf{n}_3 . For events with a two- or three-jet topology, this thrust axis approximates the direction of the two initial quarks. From here on, the direction of the thrust axis is referred to as the longitudinal direction.

The advantage of the LCMS becomes clear when the three-momentum difference of the two particles is resolved into a component Q_z parallel to the thrust axis, Q_{out} along the sum of the particles' momenta and Q_{side} perpendicular to both Q_L and Q_{out} (see Fig. 4.1), the so-called Bertsch-Pratt (BP) variables [55, 72, 73] defined as

$$Q_z = |p_{z1} - p_{z2}|, \quad (4.21)$$

$$Q_{\text{out}} = \mathbf{Q} \cdot \mathbf{K} / |\mathbf{K}|, \quad (4.22)$$

$$Q_{\text{side}} = |\mathbf{Q} \times \mathbf{K}| / |\mathbf{K}|, \quad (4.23)$$

where $\mathbf{K} = (\mathbf{p}_1 + \mathbf{p}_2)/2$ and $\mathbf{Q} = (\mathbf{p}_1 - \mathbf{p}_2)$, with \mathbf{p}_1 and \mathbf{p}_2 the momentum three-vectors of particles 1 and 2, and p_{z1}, p_{z2} their components along a properly chosen event axis (for e^+e^- collisions we use the thrust axis) in the LCMS frame, where $K_z = 0$. Then, one can decompose the invariant four-momentum difference as

$$\begin{aligned} Q^2 &= Q_z^2 + Q_{\text{side}}^2 + Q_{\text{out}}^2 - (\Delta E)^2 \\ &= Q_z^2 + Q_{\text{side}}^2 + Q_{\text{out}}^2 (1 - \beta^2), \end{aligned} \quad (4.24)$$

where

$$\beta \equiv \frac{p_{\text{out}1} + p_{\text{out}2}}{E_1 + E_2}, \quad (4.25)$$

with $p_{\text{out}i}$ and E_i ($i=1,2$) being the momenta in the out-direction and energies of the particles in the LCMS, respectively. The advantage of the LCMS now becomes apparent: the energy difference and, therefore, the difference in emission time of the particles couples only to the component Q_{out} . Therefore, in Fourier transformed space the longitudinal and the sideways components of the correlation function measure the lengths of homogeneity in longitudinal and (assuming R_2 to be invariant under the transformation $Q_{\text{side}} \rightarrow -Q_{\text{side}}$) transverse direction, respectively.

4.5 Parametrization of R_2

The two-particle Bose-Einstein correlation function can be parametrized using different variables or assuming different source functions. For example, experimental data may be presented in one dimension in terms of the invariant momentum difference, or the relative momentum can be decomposed into some experimentally preferred relative momentum components in 2 or 3 dimensions. For a two-dimensional analysis, Q_z and the transverse component Q_T defined

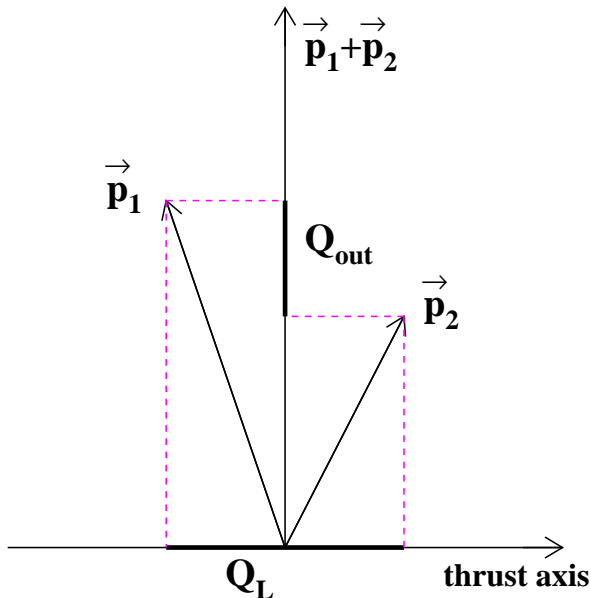


Figure 4.1: LCMS projection onto the (Q_L, Q_{out}) plane.

as $(Q_{\text{out}}^2 + Q_{\text{side}}^2)^{1/2}$ are used. When performing a three-dimensional analysis, the components Q_z , Q_{out} and Q_{side} are used. The shape of the source can follow a Gaussian distribution or can be different from that. In this section we discuss several possibilities.

4.5.1 Gaussian Source Distribution

The simplest assumption is that the source has a symmetric Gaussian distribution since a Fourier transformed Gaussian is also Gaussian and it appears frequently in nature due to the central limit theorem. In the rest frame of the pair, a Gaussian distribution is given as:

$$f(\mathbf{x}) = \frac{1}{\sqrt{2\pi R^2}} \exp\left(-\frac{(\mathbf{x} - \mathbf{x}_0)^2}{2R^2}\right), \quad (4.26)$$

where \mathbf{x} can be a one-, two- or three-dimensional coordinate vector. In this case, $\tilde{f}(\mathbf{Q}) = \exp\left(i\mathbf{x}_0\mathbf{Q} - \frac{(R\mathbf{Q})^2}{2}\right)$. (Note that in the rest frame of the pair $\mathbf{Q}^2 = Q^2$.) Substituting this into Eq. (4.10) implies that

$$R_2(Q) = 1 + \lambda \exp(-(RQ)^2). \quad (4.27)$$

Here, R is a “radius”, or a scale parameter, defined as the square root of the variance of the Gaussian distribution in configuration space. This R is a measure of the length of the region of homogeneity. This simple formula was already derived in the pioneering paper on Bose-Einstein effects by Goldhaber et al. [30].

In fact, a Gaussian ansatz for the two-particle BEC frequently gives a good first approximation to the data, particularly, if the statistical precision of the data is not adequate to perform a detailed shape analysis. One of the reasons for such a Gaussian behavior is that pion production is a rather complicated, stochastic process, in particular in collisions at very high energies. If one assumes that there are many independent processes that shift the coordinate x by δx so that the final production point is a sum of many, similarly distributed, random shifts, $x = \sum_i \delta x_i$, and further that the shifts are characterized by finite means and variances, then the probability distribution of x tends, by the central limit theorem, to a Gaussian one [37].

In order to achieve a more detailed shape analysis, the correlation function can be evaluated as a function of various components of the relative momentum Q .

Using the Bertsch-Pratt variables and a multivariate Gaussian assumption for the source distribution, recent experimental observations on e^+e^- have established an elongation (along the thrust axis) of the region of homogeneity, from which pions are emitted [63–66]. A more detailed shape analysis confirmed the elongation using a non-Gaussian shape of the correlation function [63].

In the BP variables, the correlation function corresponding to the multivariate Gaussian distribution is

$$R_2(Q_z, Q_{\text{side}}, Q_{\text{out}}) = 1 + \lambda \exp \left[-(R_z^2 Q_z^2 + R_{\text{side}}^2 Q_{\text{side}}^2 + R_{\text{out}}^2 Q_{\text{out}}^2 - 2\rho R_z R_{\text{out}} Q_z Q_{\text{out}}) \right]. \quad (4.28)$$

Here, R_z , R_{side} and R_{out} are the radius parameters defined as the square root of the variance of the source emission function in the corresponding direction of configuration space and ρ measures how strongly the z and out terms are coupled.

In the LCMS, the duration of particle emission only couples to the out-direction and only enters in the parameters R_{out} and ρ . Hence, R_{side} can be interpreted as the transverse component of the source. This parametrization assumes azimuthal symmetry, thus the only possible off-diagonal term in the covariance matrix is the $Q_z Q_{\text{out}}$ term. However, ρ must be zero due to symmetry since we have no way to define which direction is positive for thrust and major. Indeed, it turns out to be zero ($\rho R_z R_{\text{out}} = -0.1 \pm 0.6 \text{ GeV}^{-2}$ [63]), as expected.

Let us see what we can expect in the case that R_2 depends only on Q . From Eq. (4.24)

$$R^2 Q^2 = R^2 Q_z^2 + R^2 Q_{\text{side}}^2 + R^2 (1 - \beta^2) Q_{\text{out}}^2. \quad (4.29)$$

Hence Eq. (4.28) should yield $R_z^2 = R_{\text{side}}^2 = R^2$, while $R_{\text{out}}^2 = R^2 (1 - \beta^2)$. Thus for small transverse momentum, where $\beta \ll 1$, $R_{\text{out}} \approx R$, while for large transverse momentum, $R_{\text{out}} \rightarrow 0$.

Low statistics might limit an investigation of the correlation function in three

dimensions. The two-dimensional analog of Eq. (4.28) is

$$R_2(Q_z, Q_T) = 1 + \lambda \exp \left[-(R_z^2 Q_z^2 + R_T^2 Q_T^2) \right], \quad (4.30)$$

where $Q_T^2 = Q_{\text{out}}^2 + Q_{\text{side}}^2$ and R_T is an effective radius parameter defined by

$$R_T^2 (Q_{\text{side}}^2 + Q_{\text{out}}^2) = R_{\text{side}}^2 Q_{\text{side}}^2 + (1 - \beta^2) R_{\text{out}}^2 Q_{\text{out}}^2. \quad (4.31)$$

Again, we can try to find out what the result of this parametrization would be if R_2 depends only on Q . In this case, $R_z = R$ is expected and the transverse component is effectively described as

$$R_T^2 \cong R^2 \frac{Q_{\text{side}}^2 + (1 - \beta^2) Q_{\text{out}}^2}{Q_{\text{side}}^2 + Q_{\text{out}}^2}.$$

Thus at high p_t (in which case $\beta \rightarrow 1$) $R_T < R$, while at low p_t (in which case $\beta \rightarrow 0$) $R_T \rightarrow R$.

Another two-dimensional parametrization, suggested by Bowler [74], can be achieved using the classical Artru-Menessier string model [75, 76] as a dynamical model for the source seen in BEC studies of e^+e^- collisions. In this case, the correlation function becomes

$$R_2(Q_L, Q_{T_B}) = 1 + \lambda \exp \left[-(R_L^2 Q_L^2 + R_{T_B}^2 Q_{T_B}^2) \right], \quad (4.32)$$

where $Q_L^2 = Q_z^2 - (\Delta E)^2$ and $Q_{T_B}^2 = Q_{\text{out}}^2 + Q_{\text{side}}^2$. An advantage of this parametrization is that Q_{T_B} and Q_L are invariant under a Lorentz boost along the event axis. Note that $Q^2 = Q_{T_B}^2 + Q_L^2$. Hence testing the equality of R_L and R_{T_B} tests the fully symmetric Q dependence.

Another check that the Bose-Einstein correlation function depends only on Q (but not on its components individually) is the following parametrization:

$$R_2(\mathbf{Q}, Q_0) = 1 + \lambda \exp \left[-(R_1^2 \mathbf{Q}^2 - \xi R_0^2 Q_0^2) \right], \quad (4.33)$$

where $Q_0 = \Delta E$ and $\xi = \pm 1$. For $\xi = -1$, the parameters R_1 and R_0 are related, respectively, to the mean radius and the mean radiation time of a fireball-like [31] (volume emitting) source with a Gaussian space-time distribution. For $\xi = +1$ and $R_1 = R_0 = R$, Eq. (4.33) reduces to Eq. (4.27). If $\xi = +1$, the equality of R_1 and R_0 also tests the dependence of BEC on Q only.

4.5.2 Edgeworth Expansion

There is, however, no good reason why the shape of R_2 should be exactly Gaussian. A possible deviation from the Gaussian shape can be phenomenologically measured with the help of the Edgeworth expansion [36], which is an expansion about a Gaussian in terms of Hermite polynomials [77, 78]. This is a general

method to characterize any function that is approximately Gaussian. Taking only the lowest-order non-Gaussian term into account, Eq. (4.27) becomes

$$R_2(Q) = 1 + \lambda \exp[-(RQ)^2] \left[1 + \frac{\kappa}{3!} H_3(RQ) \right], \quad (4.34)$$

where κ measures the deviation from the Gaussian and $H_3(RQ) = (\sqrt{2}RQ)^3 - 3\sqrt{2}RQ$ is the third Hermite polynomial. Neglecting the $Q_z Q_{\text{out}}$ term, Eq. (4.28) becomes

$$\begin{aligned} R_2(Q_z, Q_{\text{side}}, Q_{\text{out}}) &= 1 + \lambda \exp[-(R_z^2 Q_z^2 + R_{\text{side}}^2 Q_{\text{side}}^2 + R_{\text{out}}^2 Q_{\text{out}}^2)] \cdot \\ &\cdot \left[1 + \frac{\kappa_z}{3!} H_3(|R_z Q_z|) \right] \left[1 + \frac{\kappa_{\text{side}}}{3!} H_3(|R_{\text{side}} Q_{\text{side}}|) \right] \left[1 + \frac{\kappa_{\text{out}}}{3!} H_3(|R_{\text{out}} Q_{\text{out}}|) \right], \end{aligned} \quad (4.35)$$

where κ_i ($i = z, \text{side}, \text{out}$) measures the deviation from the Gaussian in the corresponding direction.

H_3 is approximately linear around $Q = 0$, hence Eq. (4.35) describes the data points lots better, if the correlation function is more peaked than a Gaussian.

Eq. (4.35) is not, strictly speaking, a proper Edgeworth expansion, since the absolute value of the Q components is used in the arguments of the Hermite polynomials rather the Q components themselves. We use the absolute value in order to keep the function R_2 symmetric. Note that if the absolute value is used, then the support of H_3 is $[0, \infty]$, while in Edgeworth it must be $[-\infty, \infty]$ to guarantee the convergence (for more details, see [77, 78]). This is justified ad hoc by the success of the fit, rather than by the convergence properties of the Edgeworth expansion. Note also that it is possible to require symmetry and a proper Edgeworth expansion. In this case, the coefficients of odd-order Hermite polynomials have to vanish, and the phenomenologically important sensitivity to a sharp, non-Gaussian peak at $Q = 0$ is lost, while the phenomenological Eq. (4.35) indicates such structures with non-vanishing values of κ_i .

An advantage of the Edgeworth expansion is that it is model independent. Hence the values and the errors of some important quantities like the intercept parameter of the correlation function, or the width of the correlation function can be determined without theoretical bias. However, it is also a disadvantage of the Edgeworth expansion that it is model independent. Hence it is not designed to reconstruct the source function of particle emission. In other words, the model independence of the Edgeworth expansion can be both advantageous and disadvantageous, depending on our goals and points of view.

4.5.3 Lévy Stable Source Distribution

In physics, as well as in the theory of probability, the probability distribution of a sum of a large number of random variables is one of the important problems, since such distributions are frequently realized in nature. Limit distributions

characterize the probability distributions of random processes in the limiting case that the number of elementary independent random subprocesses tends to infinity.

The French mathematician Paul Lévy determined the conditions for a family of distributions to be stable (see Appendix or [79]). Such distributions are usually called Lévy stable distributions. A recent book by Zolotarev and Uchaikin [80] contains over 200 pages of applications of stable distributions in probabilistic models, correlated systems and fractals, anomalous diffusion and chaos, physics, radiophysics, astrophysics, stochastic algorithms, financial applications, biology and geology.

A Lévy stable distribution is specified by four parameters: scale R , exponent α (the index of stability), location x_0 and skewness or asymmetry parameter β . The general formula for the characteristic function of Lévy distributions is

$$\tilde{f}(Q) = \exp \left[-\frac{1}{2}R^\alpha|Q|^\alpha + i\frac{\beta}{2}R^\alpha|Q|^\alpha \text{sign}(Q) \tan \left(\frac{\alpha\pi}{2} \right) + iQx_0 \right]. \quad (4.36)$$

For more details, see Ref. [81]. The skewness parameter must lie in the range $[-1, 1]$ and when it is zero, the distribution is symmetric. In the case of $\beta = \pm 1$ a one-sided distribution is obtained. To obtain a source distribution which is positive for all values of its argument, the index of stability has to satisfy $0 < \alpha \leq 2$. The case where $\alpha = 2$ and $\beta = 0$ corresponds to the Gaussian. In this chapter, we limit ourselves to the class of symmetric distributions, but a class of one-sided distributions will be treated in Sect. 6.2.

Symmetric Lévy Parametrization

The Fourier transform (characteristic function) of the symmetric Lévy stable distribution $\tilde{f}(Q)$ has the following general form:

$$\tilde{f}(Q) = \exp \left(ix_0Q - \frac{|RQ|^\alpha}{2} \right). \quad (4.37)$$

Then R_2 has the following, relatively simple form [37]:

$$R_2(Q) = 1 + \lambda \exp(-|RQ|^\alpha). \quad (4.38)$$

Note that the forms $\exp(-|RQ|^\alpha)$ are frequently called stretched exponential fits.

In the BP variables, neglecting the cross term, the correlation function corresponding to the multivariate Lévy stable distribution is

$$R_2(Q_z, Q_{\text{out}}, Q_{\text{side}}) = 1 + \lambda \exp \left(-|R_z^2 Q_z^2 + R_{\text{out}}^2 Q_{\text{out}}^2 + R_{\text{side}}^2 Q_{\text{side}}^2|^{\alpha/2} \right), \quad (4.39)$$

and Eq. (4.33) becomes

$$R_2(\mathbf{Q}, Q_0) = 1 + \lambda \exp \left(-|R_1^2 \mathbf{Q}^2 - \xi R_0^2 Q_0^2|^{\alpha/2} \right). \quad (4.40)$$

Fits of these parametrizations to the data are given in the following chapter. More details on multi-variate Lévy distributions are given in [37].

4.6 Long-range Correlation

As a background, there may be an effect from long-range correlations not adequately taken into account by the reference sample. Therefore, R_2 is usually not found to be constant at large Q . To account for this, the BE correlation function R_2 is multiplied by an appropriate factor, usually a linear dependence either on Q , $\gamma(1 + \delta Q)$, or on its components, e.g., $\gamma(1 + \delta Q_z + \epsilon Q_{\text{out}} + \xi Q_{\text{side}})$. The results will generally find δ (ϵ and ξ) to be small.

4.7 Systematic Uncertainties and Checks

Systematic uncertainties on the results are estimated by considering various sources of systematics:

- event and track selection;
- mixing algorithm used to form the reference sample;
- Monte Carlo generator used in detector and mixing corrections;
- range of Q used in fits and parametrization of long-range effects.

In addition, it was checked that conclusions do not depend on the jet algorithm used or the exact value of y_{cut} .

Track quality cuts

The influence of the track quality cuts is investigated by varying independently each cut parameter (Sect. 3.2) to the values given in Table 4.1. For each cut parameter, p , starting from the original value C_0^p , we redo our analysis using both smaller, C_α^p , and larger, C_ω^p , values. We look for the systematic contribution to the parameters of the BE correlation function. Let us denote $P^{C_0^p}(i)$ the fit result for the i^{th} parameter of the correlation function when the original value of the cut parameter is used. Changes of the fit results produced by varying the selection cuts to C_α^p and C_ω^p are added in quadrature. Positive and negative deviations from the standard result were treated separately and resulted in the positive and negative systematic uncertainty, respectively.

$$\delta_{\text{track}}^{\text{sys}} P(i) = \sqrt{\sum_p^{\text{all cuts}} \left(P^{C_0^p}(i) - P^{C_{\omega/\alpha}^p}(i) \right)^2}, \text{ where } C_0^p \in [C_\alpha^p; C_\omega^p]. \quad (4.41)$$

The systematic uncertainties from each of the track quality cuts are added in quadrature to give the total systematic uncertainty from the track quality cuts:

$$\Delta_{\text{track}}^{\text{syst}} = \sqrt{\sum_i (\delta_{\text{track}}^{\text{syst}} P(i))^2}. \quad (4.42)$$

Standard cuts	C_α^p	C_ω^p
$p_t > 150$ MeV	100 MeV	200 MeV
Span > 40	32	48
$N_{\text{Hits}} > 25$	15	35
DCA < 10 mm	5 mm	15 mm

Table 4.1: Alternative values used to determine the systematic uncertainty due to the choice of the track quality cuts.

Event selection

The systematic uncertainty from the event selection was determined in a manner very similar to that of track quality cuts.

The best values for the parameters of the event selection were described in Sect. 3.1 and 3.3. The alternative cuts for this systematic uncertainty study are summarized in Table 4.2 .

Standard cuts	C_α^p	C_ω^p
$0.5 < E^{\text{cal}}/\sqrt{s}$	0.45	0.55
$E^{\text{cal}}/\sqrt{s} < 1.5$	1.55	1.45
$E_{\parallel}^{\text{cal}} < 0.6$	0.5	0.7
$E_{\perp}^{\text{cal}} < 0.4$	0.3	0.5
$N_{\text{clus}} > 14$	12	16

Table 4.2: Alternative values used to determine the systematic uncertainty due to the choice of the event selection cuts.

Mixing sample

When the reference sample is created the tracks come from different randomly selected events. These events are required to have similar multiplicity. Here events are assigned to multiplicity classes. To obtain the systematic uncertainty of this source, those mixed events are investigated in which the absolute value of the difference between the multiplicities of the original event and the mixed track's event is 1, 2, 3 or 4. Then the same technique was used to evaluate the

systematic uncertainty from the mixing sample, as used for the track quality cuts or the event selection.

Monte Carlo

An important source of systematic uncertainty is the model used for the detector and mixing corrections. This uncertainty is estimated by using different Monte Carlo models: JETSET with and without Bose-Einstein correlations and HERWIG are used for the detector correction, while JETSET, PYTHIA and HERWIG, all without Bose-Einstein simulation, are used for the mixing correction. The same technique is used for the calculation of the systematic uncertainty from this source, as used for that from the track quality cuts, event selection and mixing sample.

Fit range and δ

Instead of the range $0 < Q < 4$ GeV used in our analysis, we have also fitted the correlation functions in the range $0 < Q < 8$ GeV. Related to this fit range study is the adequacy of the parametrization of long-range effects, i.e., the $(1 + \delta Q)$ term. To investigate this, fits are performed fixing δ to zero as well as fixing it to the value found in a fit of $R_2 = \gamma(1 + \delta Q)$ in the region $Q > 2$ GeV. The same technique was used for the calculation of the systematic uncertainty from this source, as described for the track quality cuts and other systematic errors.

Chapter 5

Results on the Parametrization of R_2

5.1 Introduction

In this chapter, Bose-Einstein correlations are investigated in hadronic Z decays in two and three components of the four-momentum difference Q as well as in the absolute value of Q itself. In order to extract information on the shape and the width of the Bose-Einstein correlation function, R_2 , various parametrizations of its relative momentum dependence are studied.

The outline of the chapter is as follows. Firstly, we look for the proper variables of the correlation function, starting with an investigation of the three-dimensional Bertsch-Pratt (BP) parametrization. The next step is to reduce the number of components of Q to two, comparing the Bertsch-Pratt and Bowler parametrizations. Finally, the correlation function is investigated simply as a function of the absolute value of Q . Gaussian, Edgeworth and Lévy stable parametrizations are compared. In the last section, the conclusions of this chapter are summarized.

5.2 Proper Variables of R_2

First we investigate various assumptions for the variables of the correlation function. In particular, we check its dependence on BP variables, Bowler variables and the invariant four-momentum difference, Q .

5.2.1 Assuming Dependence on $(Q_z, Q_{\text{side}}, Q_{\text{out}})$

In a first step, we compare three-dimensional BP parametrizations assuming various symmetric shapes of the source function: Gaussian, Edgeworth and Lévy. Including the long-range correlation and normalization factors, Eqs. (4.28), (4.35) and (4.39) become

$$R_2(Q_z, Q_{\text{side}}, Q_{\text{out}}) = \gamma(1 + \delta Q_z + \xi Q_{\text{side}} + \epsilon Q_{\text{out}}) \left[1 + \lambda \exp(-R_z^2 Q_z^2 - R_{\text{side}}^2 Q_{\text{side}}^2 - R_{\text{out}}^2 Q_{\text{out}}^2) \right], \quad (5.1)$$

$$R_2(Q_z, Q_{\text{side}}, Q_{\text{out}}) = \gamma(1 + \delta Q_z + \xi Q_{\text{side}} + \epsilon Q_{\text{out}}) \left\{ 1 + \lambda \exp(-R_z^2 Q_z^2 - R_{\text{side}}^2 Q_{\text{side}}^2 - R_{\text{out}}^2 Q_{\text{out}}^2) \left[1 + \frac{\kappa_z}{3!} H_3(R_z Q_z) \right] \left[1 + \frac{\kappa_{\text{side}}}{3!} H_3(R_{\text{side}} Q_{\text{side}}) \right] \left[1 + \frac{\kappa_{\text{out}}}{3!} H_3(R_{\text{out}} Q_{\text{out}}) \right] \right\}, \quad (5.2)$$

and

$$R_2(Q_z, Q_{\text{side}}, Q_{\text{out}}) = \gamma(1 + \delta Q_z + \xi Q_{\text{side}} + \epsilon Q_{\text{out}}) \left\{ 1 + \lambda \exp\left(-|R_z^2 Q_z^2 + R_{\text{side}}^2 Q_{\text{side}}^2 + R_{\text{out}}^2 Q_{\text{out}}^2|^{\alpha/2}\right) \right\}, \quad (5.3)$$

respectively.

The experimental results of the fits of the correlation function for the all-events and two-jet event samples, using Eqs. (5.1), (5.2) and (5.3) in the LCMS frame, are presented in Table 5.1 and 5.2, respectively.

The fit results for both the Edgeworth and the Lévy stable parametrizations have a confidence level an order of magnitude better than that for the Gaussian. Furthermore, the Lévy stable parametrization is both more general and more economic in the number of parameters than the Edgeworth expansion. The value of $\alpha = 1.15 \pm 0.10$ is significantly smaller than 2, thus indicating power-law tails in the coordinate space distributions, even in the local regions of homogeneity of particle emission.

An elongation of the region of homogeneity along the thrust direction as observed in [63–66, 82] for the BP frame is confirmed by the ratio R_{side}/R_z being significantly smaller than unity, for all of the parametrizations used. Nevertheless, the difference in longitudinal and transverse radius is only of the order of 20 – 30%. Table 5.1 suggests that R_{side} and R_{out} are equal within 1σ or 2σ errors for all the three parametrizations of Eqs. (5.1), (5.2) and (5.3). This suggests that the dependence of R_2 on Q_{side} and Q_{out} is similar, and the three-dimensional correlation function depends only on Q_z and $Q_T = Q_{\text{side}}^2 + Q_{\text{out}}^2$. This is investigated in Sub-Sect. 5.2.2.

parameter	Gaussian	Edgeworth	Sym. Lévy
γ	0.958 ± 0.004	0.915 ± 0.007	0.912 ± 0.007
λ	0.45 ± 0.01	0.62 ± 0.02	0.75 ± 0.04
R_z (fm)	0.73 ± 0.05	0.66 ± 0.05	0.97 ± 0.05
R_{out} (fm)	0.50 ± 0.06	0.37 ± 0.07	0.63 ± 0.06
R_{side} (fm)	0.56 ± 0.06	0.51 ± 0.06	0.71 ± 0.05
R_{out}/R_z	0.69 ± 0.06	0.56 ± 0.06	0.65 ± 0.06
R_{side}/R_z	0.77 ± 0.06	0.77 ± 0.06	0.73 ± 0.06
$\kappa_{3,z}$	—	0.47 ± 0.05	—
$\kappa_{3,\text{out}}$	—	0.98 ± 0.12	—
$\kappa_{3,\text{side}}$	—	0.14 ± 0.07	—
α	2 (fixed)	2 (fixed)	1.15 ± 0.10
δ (GeV $^{-1}$)	0.024 ± 0.004	0.068 ± 0.008	0.067 ± 0.007
ϵ (GeV $^{-1}$)	0.015 ± 0.003	0.020 ± 0.004	0.032 ± 0.004
ξ (GeV $^{-1}$)	-0.052 ± 0.004	-0.022 ± 0.006	-0.036 ± 0.004
χ^2/NDF	2622/2189	2359/2186	2411/2188
CL (%)	$4 \cdot 10^{-8}$	0.5	0.05

Table 5.1: Fit results using the Bertsch-Pratt variables, assuming Gaussian, Edgeworth or symmetric Lévy stable forms of the shape for the all-event sample.

5.2.2 Investigating Two-dimensional Dependence

In this step, we analyse the results of the fits of the BP two-dimensional parametrization, Eq. (4.30), and the Bowler parametrization, Eq. (4.32), which have the following forms after including long-range correlations and normalization:

$$R_2(Q_z, Q_T) = \gamma (1 + \delta Q_z + \epsilon Q_T) [1 + \lambda \exp(-R_z^2 Q_z^2 - R_T^2 Q_T^2)] \quad (5.4)$$

and

$$R_2(Q_L, Q_{T_B}) = \gamma (1 + \delta' Q_L^2 + \epsilon' Q_{T_B}^2) [1 + \lambda \exp(-R_L^2 Q_L^2 - R_{T_B}^2 Q_{T_B}^2)]. \quad (5.5)$$

There is an important difference between these two parametrizations. The domain $Q = 0$, which is important for BEC, is mapped into a single point in Eq. (5.4), namely the point $Q_z^2 = Q_T^2 = 0$ (Fig. 5.1a). On the other hand, in the case of the Bowler parametrization in Eq. (5.5), $Q = 0$ is extended into a line, namely the line $Q_{T_B}^2 = -Q_L^2$. As shown in Figs. 5.1b and 5.1c, the correlation function has its maximum along this line.

If the correlation function depends independently on the components of Q (e.g. Q_z , Q_{side} , Q_{out} or Q_L , Q_{T_B} , etc.) then R_2 must have a form like

$$R_2 = \gamma \cdot A \cdot \prod_i |\tilde{G}_i(Q_i)|^2, \quad (5.6)$$

parameter	Gaussian	Edgeworth	Sym. Lévy
γ	0.976 ± 0.006	0.943 ± 0.010	0.915 ± 0.015
λ	0.39 ± 0.01	0.51 ± 0.02	0.66 ± 0.06
R_z (fm)	0.73 ± 0.05	0.66 ± 0.07	0.90 ± 0.05
R_{out} (fm)	0.51 ± 0.06	0.43 ± 0.06	0.60 ± 0.06
R_{side} (fm)	0.47 ± 0.06	0.44 ± 0.07	0.54 ± 0.06
R_{out}/R_z	0.70 ± 0.06	0.65 ± 0.06	0.67 ± 0.05
R_{side}/R_z	0.64 ± 0.06	0.66 ± 0.06	0.61 ± 0.05
$\kappa_{3,z}$	—	0.47 ± 0.01	—
$\kappa_{3,\text{out}}$	—	0.66 ± 0.09	—
$\kappa_{3,\text{side}}$	—	0.00 ± 0.06	—
α	2 (fixed)	2 (fixed)	1.14 ± 0.09
δ (GeV^{-1})	0.013 ± 0.006	0.044 ± 0.010	0.070 ± 0.015
ϵ (GeV^{-1})	-0.005 ± 0.005	0.005 ± 0.006	0.018 ± 0.008
ξ (GeV^{-1})	-0.073 ± 0.005	-0.056 ± 0.007	-0.061 ± 0.007
χ^2/NDF	2294/2189	2237/2186	2221/2188
CL (%)	6	22	31

Table 5.2: Fit results using the Bertsch-Pratt variables, assuming Gaussian, Edgeworth or symmetric Lévy stable forms of the shape for the two-jet event sample.

where A includes the long-range correlations and \tilde{G} is the Fourier transform of a component of the particle emitting source, while i denotes the various directions. In this case, $R_2 \rightarrow 1$ if any $Q_i \rightarrow \infty$, i.e. the correlation function decreases when any of the components of Q becomes large. But, as seen in Figs. 5.1b and c, the correlation function does not behave like this. The correlation function keeps its maximum even at high values of Q_{T_B} . This property of R_2 is qualitatively different from the behavior of the BP parametrization.

From Table 5.3, it can be seen that the BP parametrization (5.4) confirms the elongation in the BP frame, while the Bowler parametrization (albeit with very low confidence level) gives longitudinal and transverse radii equal to each other within errors (Table 5.3). This may suggest that the correlation function is a function of Q rather than of its components separately. This conclusion is also supported by the results for e^+e^- at $\sqrt{s} = 34$ GeV of the TASSO collaboration [67], which found $R_L = 0.78 \pm 0.11$ fm and $R_{\text{T}_B} = 0.66 \pm 0.08$ fm with a confidence level of 47% .

In order to check further the possibility of a mere Q dependence of the Bose-Einstein correlation function, we decompose the invariant momentum difference into the three-momentum vector difference and the energy difference as in Eq. (4.33). The corresponding Lévy parametrization is Eq. (4.40). In the framework of fireball-like models [31] (with independent space and decay-time distributions of emitters within the fireball volume or the fireball surface), no

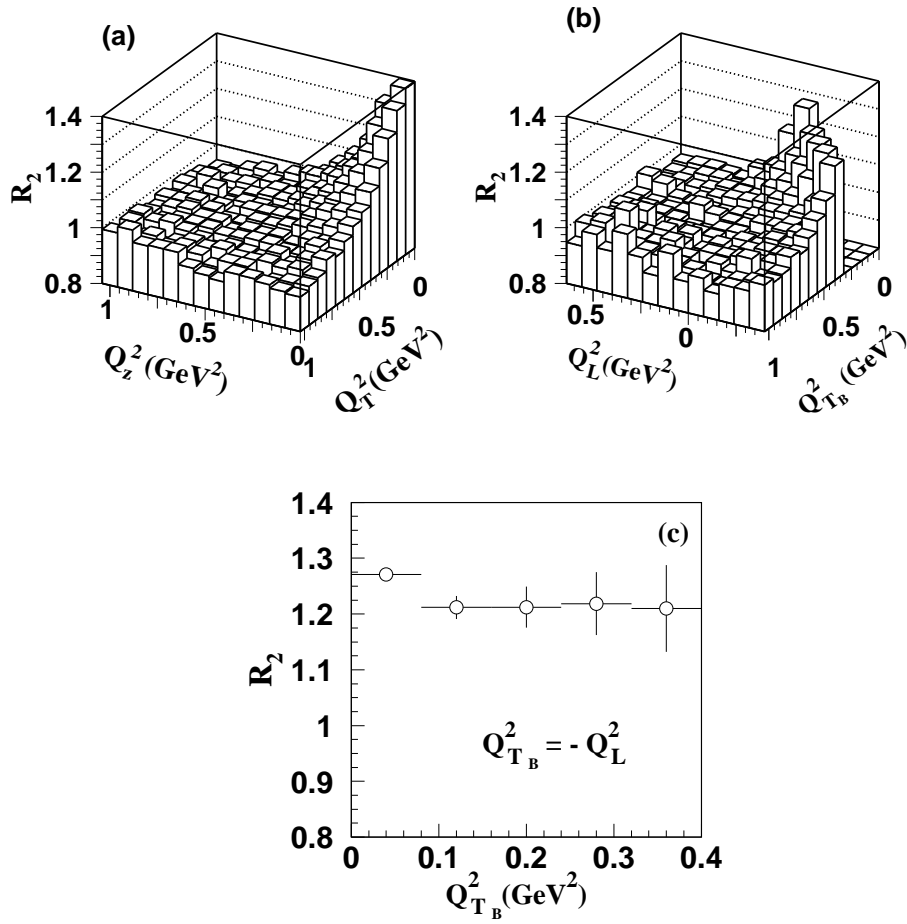


Figure 5.1: The correlation function R_2 in the Bertsch-Pratt (a), in the Bowler (b) variables in the LCMS frame, and along the line $Q_{T_B}^2 = -Q_L^2$ of the Bowler parametrization (c).

parameter	Bertsch-Pratt		Bowler	
	all-event	two-jet event	all-event	two-jet event
γ	0.79 ± 0.01	0.698 ± 0.004	0.918 ± 0.005	0.94 ± 0.01
λ	1.04 ± 0.01	1.08 ± 0.02	0.43 ± 0.01	0.39 ± 0.02
R_z (fm)	0.39 ± 0.01	0.36 ± 0.01	—	—
R_T (fm)	0.34 ± 0.01	0.29 ± 0.01	—	—
R_L (fm)	—	—	0.54 ± 0.01	0.51 ± 0.01
R_{T_B} (fm)	—	—	0.57 ± 0.01	0.55 ± 0.02
δ (GeV^{-1})	0.16 ± 0.01	0.29 ± 0.01	—	—
ϵ (GeV^{-1})	0.10 ± 0.01	0.13 ± 0.01	—	—
δ' (GeV^{-2})	—	—	0.08 ± 0.003	0.03 ± 0.002
ϵ' (GeV^{-2})	—	—	0.03 ± 0.002	0.03 ± 0.01
χ^2/NDF	261/163	203 / 163	350 / 143	213 / 143
CL (%)	10^{-4}	2	10^{-17}	10^{-2}

Table 5.3: Fit results according to the Bertsch-Pratt (5.4) and Bowler (5.5) parametrizations for the all-event and two-jet event samples.

interference effects are expected at large \mathbf{Q} and Q_0 .

After including the long-range correlation, Eqs. (4.33) and (4.40) become

$$R_2(\mathbf{Q}, Q_0) = \gamma(1 + \delta|\mathbf{Q}| + \epsilon Q_0) [1 + \lambda \exp(- (R_1^2 \mathbf{Q}^2 - \xi R_0^2 Q_0^2))] \quad (5.7)$$

and

$$R_2(\mathbf{Q}, Q_0) = \gamma(1 + \delta|\mathbf{Q}| + \epsilon Q_0) \left[1 + \lambda \exp\left(- |R_1^2 \mathbf{Q}^2 - \xi R_0^2 Q_0^2|^{\alpha/2}\right) \right], \quad (5.8)$$

respectively.

The results for these fits are summarized in Tables 5.4 and 5.5 for all events and for two-jet events, respectively. The fits with $\xi = -1$, corresponding to a BP four-dimensional Gaussian source, have a very poor χ^2 both for two-jet and for all-event, thus ruling out a fireball-like source.

In the case of $\xi = +1$ the confidence levels are better, in particular for two-jet events. The values of these fit parameters show similar behavior for the all-event and two-jet samples. We find that $R_1^2 = R_0^2$ within experimental errors both samples. In the case of the stretched exponential fit of Eq. (5.8), we find that the parameter α is significantly below 2.

The fit results of Eq. (5.7) and (5.8) are interpreted as evidence that in e^+e^- collisions at $\sqrt{s} = m_Z$ the two-particle BEC depend on the relative momentum components only through the variable Q rather than on its components separately. This is further checked by explicit evaluation of the two-particle Bose-Einstein correlation function in the variables $Q_0, |\mathbf{Q}|$ in Fig. 5.2 for all events and in Fig. 5.3 for the two-jet events. Similarly to the earlier results by the

parameter	$\xi = -1$		$\xi = +1$	
	Eq. (5.7)	Eq. (5.8)	Eq. (5.7)	Eq. (5.8)
γ	0.96 ± 0.01	0.78 ± 0.01	0.924 ± 0.002	0.861 ± 0.005
λ	0.40 ± 0.01	0.99 ± 0.66	0.346 ± 0.003	0.44 ± 0.01
R_1 (fm)	0.58 ± 0.01	0.68 ± 0.01	0.57 ± 0.01	0.54 ± 0.01
R_0 (fm)	0.00 ± 0.02	0.00 ± 0.04	0.55 ± 0.01	0.52 ± 0.01
α	—	1.06 ± 0.03	—	1.67 ± 0.04
δ (GeV $^{-1}$)	-0.05 ± 0.01	0.15 ± 0.01	0.031 ± 0.003	0.12 ± 0.01
ϵ (GeV $^{-1}$)	0.12 ± 0.01	0.14 ± 0.01	0.007 ± 0.006	-0.03 ± 0.01
χ^2/NDF	917/85	881 / 84	125/85	110/84
CL (%)	0	0	0.3	3

Table 5.4: Fit results using Eqs. (5.7) and (5.8) for all events.

parameter	$\xi = -1$		$\xi = +1$	
	Eq. (5.7)	Eq. (5.8)	Eq. (5.7)	Eq. (5.8)
γ	0.96 ± 0.01	0.73 ± 0.01	0.94 ± 0.01	0.89 ± 0.01
λ	0.37 ± 0.01	0.99 ± 0.01	0.31 ± 0.02	0.39 ± 0.01
R_1 (fm)	0.55 ± 0.01	0.58 ± 0.01	0.55 ± 0.01	0.52 ± 0.01
R_0 (fm)	0.00 ± 0.04	0.00 ± 0.03	0.53 ± 0.02	0.49 ± 0.01
α	—	1.10 ± 0.02	—	1.71 ± 0.06
δ (GeV $^{-1}$)	-0.04 ± 0.01	0.22 ± 0.02	0.01 ± 0.01	0.08 ± 0.01
ϵ (GeV $^{-1}$)	0.11 ± 0.01	0.14 ± 0.01	0.01 ± 0.02	-0.02 ± 0.02
χ^2/NDF	299/85	284 / 84	86/85	83 / 84
CL (%)	10^{-23}	10^{-21}	45	51

Table 5.5: Fit results using Eqs. (5.7) and (5.8) for two-jet events. This implies that $R_2 = R_2(Q)$ in two-jet events.

TASSO Collaboration [67], we find that the BEC are maximal along the entire diagonal $Q_0^2 = \mathbf{Q}^2$. Note that in Table 5.5 a good confidence level is achieved and $R_1 \approx R_0$ (within 1σ) and $\xi = +1$, as would be expected for a simple Q dependence. Note however, that the CL is not as good for all events in Table 5.4. We shall see later that this fit quality can be improved by modeling the shape of $R_2(Q)$ with more sophisticated forms.

Whether BEC depend only on Q or on its components separately has been studied in meson-proton reactions at CERN SPS energies by the NA22 Collaboration [69]. The correlation function $R_2(\mathbf{Q}, Q_0)$ was found to decrease with increasing value of $\mathbf{Q}^2 (\approx Q_0^2)$ along the diagonal $Q_0^2 = \mathbf{Q}^2$ (see Fig. 5.4), indicating that, contrary to e^+e^- collisions, in hadron-proton reactions the functional dependence of the correlation function is on the energy and momentum components separately.

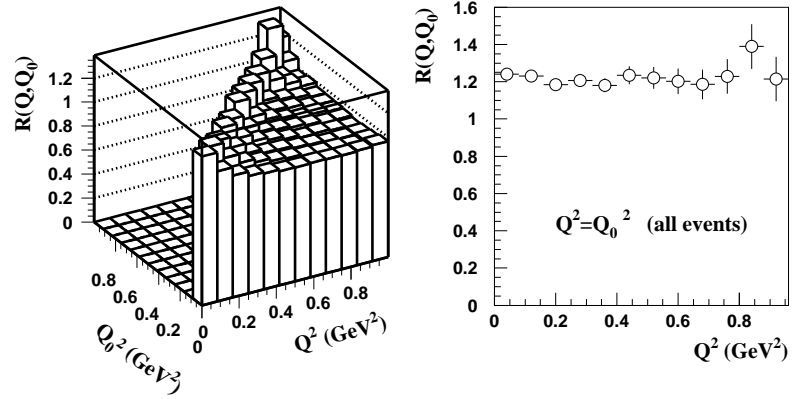


Figure 5.2: $R_2(\mathbf{Q}, Q_0)$ for all events: (a) as a function of \mathbf{Q}^2 and Q_0^2 , (b) as a function of $\mathbf{Q}^2 = Q_0^2$, in bins of 0.08 GeV^2 .

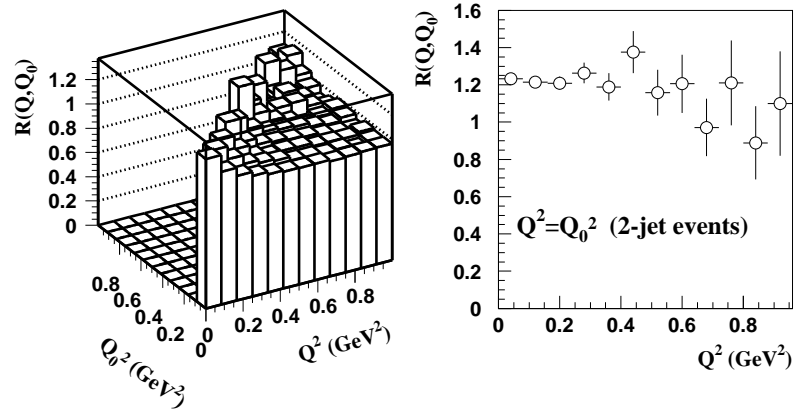


Figure 5.3: $R_2(\mathbf{Q}, Q_0)$ for 2-jet events: (a) as a function of \mathbf{Q}^2 and Q_0^2 , (b) as a function of $\mathbf{Q}^2 = Q_0^2$, in bins of 0.08 GeV^2 .

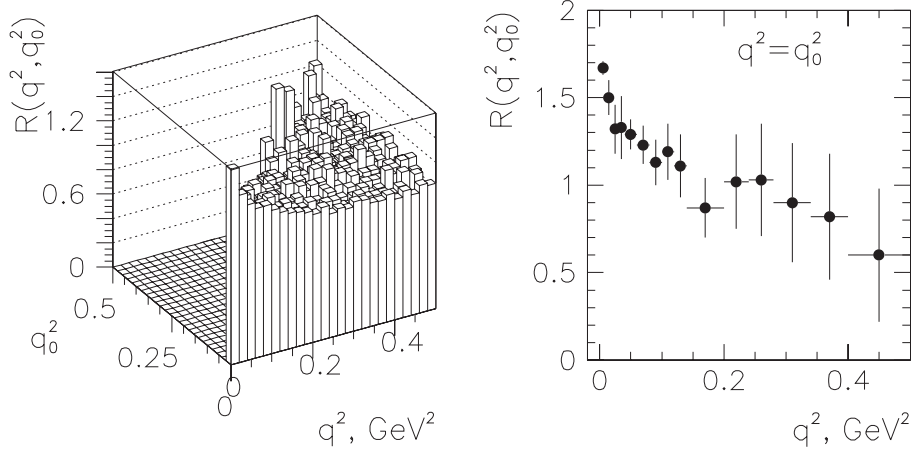


Figure 5.4: NA22 results on $\pi^- \pi^-$ correlations [69]: $R_2(\mathbf{Q}, Q_0)$ at $\mathbf{Q}^2, Q_0^2 < 0.5$ GeV^2 (left); and $R_2(\mathbf{Q}, Q_0)$ as a function of \mathbf{Q}^2 at $\mathbf{Q}^2 \approx Q_0^2$ (right).

Also in heavy-ion interactions, BEC are found not to depend simply on Q , but on the components of the momentum difference separately [31], and R_2 decreases with increasing Q_i .

5.3 Assuming that R_2 is a function of Q

Based on the observations of the previous section, from here on we consider only parametrizations of the two-pion correlation function that depend merely on the invariant momentum difference Q of the two pions.

After accounting for long-range correlations, the Gaussian, Edgeworth and symmetric Lévy parametrizations have the following form

$$R_2(Q) = \gamma(1 + \delta Q) [1 + \lambda \exp(-(RQ)^2)], \quad (5.9)$$

$$R_2(Q) = \gamma(1 + \delta Q) \left\{ 1 + \lambda \exp(-(RQ)^2) \left[1 + \frac{\kappa}{3!} H_3(RQ) \right] \right\} \quad (5.10)$$

and

$$R_2(Q) = \gamma(1 + \delta Q) [1 + \lambda \exp(-|RQ|^\alpha)], \quad (5.11)$$

respectively. The results of fits of these equations for all events are given in Table 5.6 and shown in Fig. 5.5, for three-jet events in Table 5.7 and Fig. 5.6, and for two-jet events in Table 5.8 and Fig. 5.7.

The Gaussian fit of Eq. (5.9) to the data results in an unacceptably low confidence level. The fit is particularly bad at low Q values, as is shown in Fig. 5.5a for all events, in Fig. 5.6a for three-jet events and in Fig. 5.7a for two-jet events, from which we conclude that the shape of the source deviates from a Gaussian. The Edgeworth expansion Eq. (5.10) to the two-jet event sample

(Fig. 5.7b) gives a better fit (CL = 0.7 %) with $\kappa = 0.71 \pm 0.06$. which confirms that the shape of the source deviates from a Gaussian. The Edgeworth fits are poor for the three-jet and all-event samples. Note, however, that also in these cases the value of κ is far from zero.

parameter	Gaussian	Edgeworth	symmetric Lévy
γ	0.951 ± 0.001	0.948 ± 0.001	0.947 ± 0.001
λ	0.43 ± 0.01	0.60 ± 0.02	0.59 ± 0.02
R (fm)	0.65 ± 0.01	0.74 ± 0.01	0.812 ± 0.002
κ	-	0.71 ± 0.06	-
α	2	2	1.34 ± 0.04
δ (GeV $^{-1}$)	0.017 ± 0.001	0.018 ± 0.001	0.019 ± 0.001
χ^2 /NDF	796/96	561/95	634/95
CL (%)	< 0.001	< 0.001	< 0.001

Table 5.6: Fit results using the Q variable, assuming Gaussian, Eq. (5.9), Edgeworth, Eq. (5.10), or symmetric Lévy stable, Eq. (5.11), form of the correlation function for data of all events.

parameter	Gaussian	Edgeworth	symmetric Lévy
γ	0.946 ± 0.001	0.944 ± 0.001	0.942 ± 0.001
λ	0.51 ± 0.01	0.75 ± 0.02	0.70 ± 0.02
R (fm)	0.73 ± 0.01	0.86 ± 0.02	0.93 ± 0.02
κ	-	0.74 ± 0.05	-
α	2	2	1.39 ± 0.04
δ (GeV $^{-1}$)	0.02 ± 0.01	0.02 ± 0.01	0.02 ± 0.01
χ^2 /NDF	611/96	464/95	503/95
CL (%)	< 0.001	< 0.001	< 0.001

Table 5.7: Fit results using the Q variable, assuming Gaussian, Eq. (5.9), Edgeworth, Eq. (5.10), or symmetric Lévy stable, Eq. (5.11), form of the correlation function for three-jet events.

From the symmetric Lévy fit of Eq. (5.11) to the two-jet data shown in Fig. 5.7c, it is clear that the correlation function is not Gaussian: $\alpha = 1.34 \pm 0.04$. However, the confidence level, although improved compared to the fit of Eq. (5.9), is still unacceptably low. The same can be concluded for the three-jet and all-event samples.

Both the symmetric Lévy parametrization and the Edgeworth parametrizations do a fair job of describing the region $Q < 0.6$ GeV for all events and three-jet events as well as for two-jet events, but fail at higher Q . R_2 is nearly constant (≈ 1) in the region $Q \geq 1.5$ GeV. However, in the region 0.6–1.5 GeV R_2 has a smaller value, dipping below unity (more correctly, dipping below the

parameter	Gaussian	Edgeworth	symmetric Lévy
γ	0.958 ± 0.002	0.959 ± 0.002	0.951 ± 0.002
λ	0.43 ± 0.01	0.60 ± 0.02	0.59 ± 0.02
R (fm)	0.65 ± 0.01	0.74 ± 0.01	0.812 ± 0.002
κ	-	0.71 ± 0.06	-
α	2	2	1.34 ± 0.04
δ (GeV $^{-1}$)	0.011 ± 0.001	0.013 ± 0.001	0.014 ± 0.001
χ^2/NDF	234/96	132/95	148/95
CL (%)	< 0.001	0.7	0.04

Table 5.8: Fit results using the Q variable, assuming Gaussian, Eq. (5.9), Edgeworth, Eq. (5.10), or symmetric Lévy stable, Eq. (5.11), form of the correlation function for two-jet events.

value of $\gamma(1 + \delta Q)$), which is indicative of an anti-correlation. This is clearly seen in Fig. 5.7c by comparing the data in this region to an extrapolation of a linear fit, Eq. (5.11) with $\lambda = 0$, in the region $Q \geq 1.5$ GeV, which is indicated by the dot-dashed line. To check that the dip is present and looks the same, irrespective of the fit range of the long-range correlations, we show the data for two-jet events and the long-range part fitted with $\gamma(1 + \delta Q)$ for $Q > 1.5$ GeV, 1.8 GeV, 2.1 GeV and 2.5 GeV in Fig. 5.8a, b, c and d, respectively. The inability to describe this dip in R_2 is the primary reason for the failure of both the Edgeworth and symmetric Lévy parametrizations, while the Gaussian fails to describe not only this dip at $Q \approx 1$ GeV but also the peak of R_2 at $Q \rightarrow 0$.

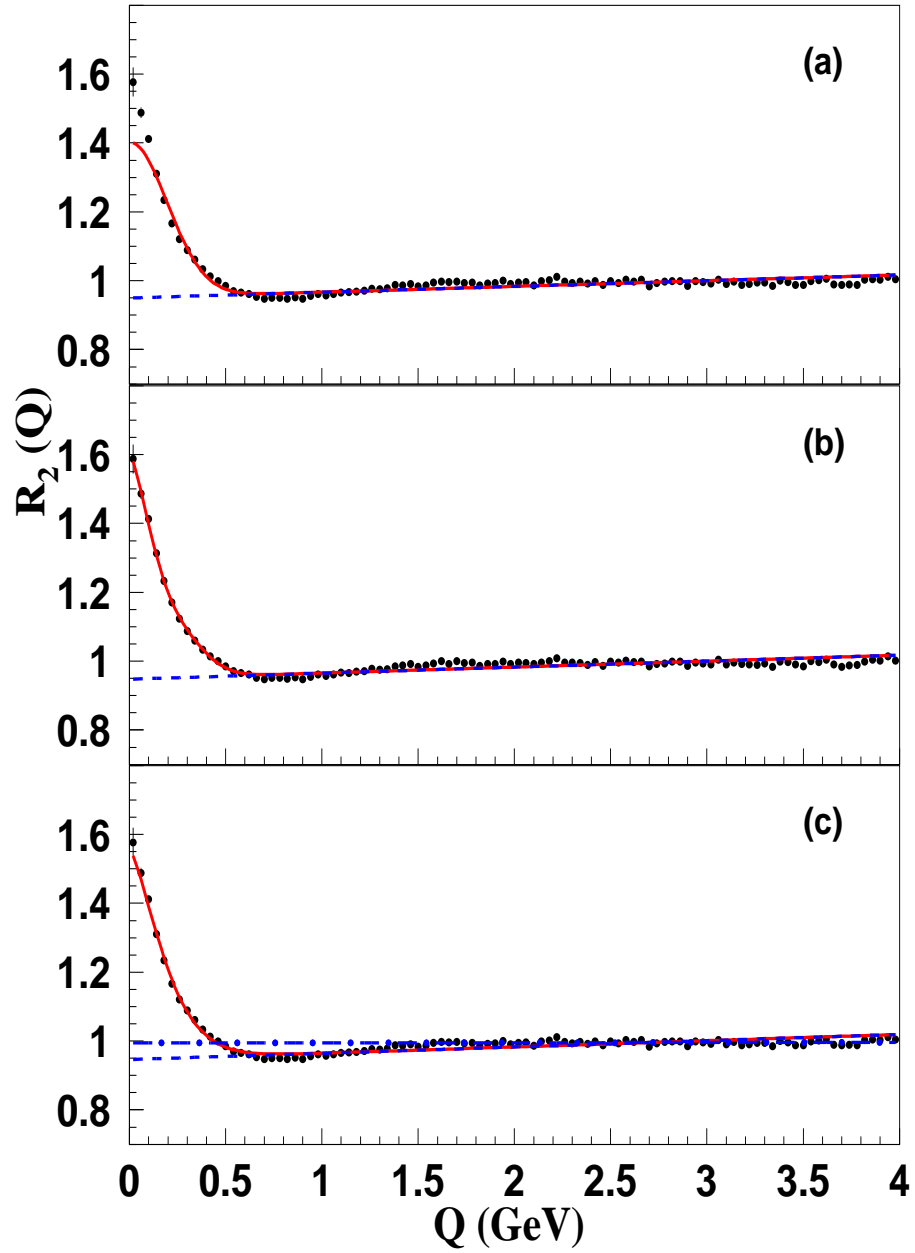


Figure 5.5: The Bose-Einstein correlation function R_2 for all events with the (a) Gaussian, (b) Edgeworth, (c) symmetric Lévy fits. Dashed lines represent extrapolations of the long-range part, $\gamma(1 + \delta Q)$, of the fit. The dot-dashed line in (c) is the result of a fit of Eq. (5.11) with $\lambda = 0$ to the long-range part ($Q > 1.5$ GeV) of the correlation function.

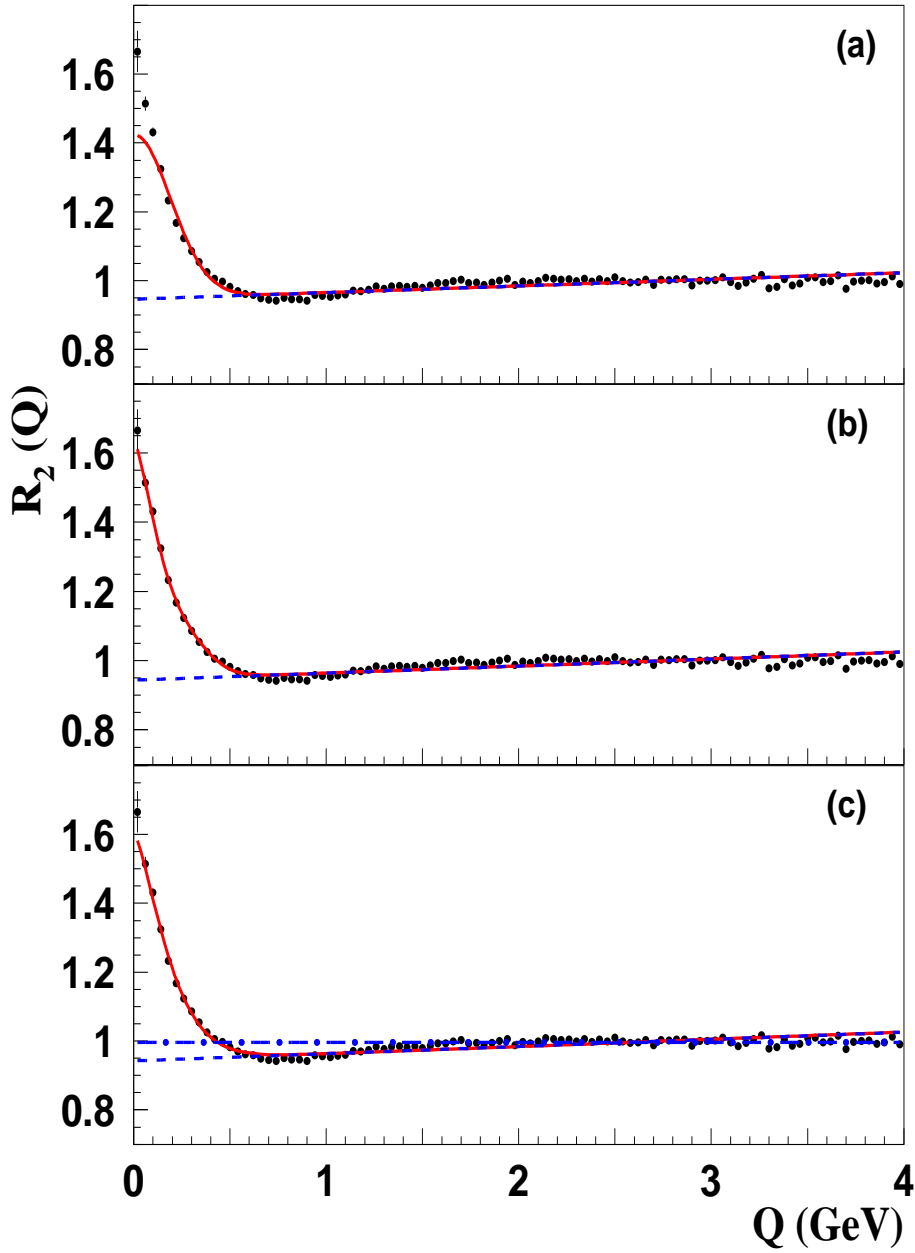


Figure 5.6: The Bose-Einstein correlation function R_2 for three-jet events with the (a) Gaussian, (b) Edgeworth, (c) symmetric Lévy fits. Dashed lines represent extrapolations of the long-range part, $\gamma(1 + \delta Q)$, of the fit. The dot-dashed line in (c) is the result of a fit of Eq. (5.11) with $\lambda = 0$ to the long-range part ($Q > 1.5$ GeV) of the correlation function.

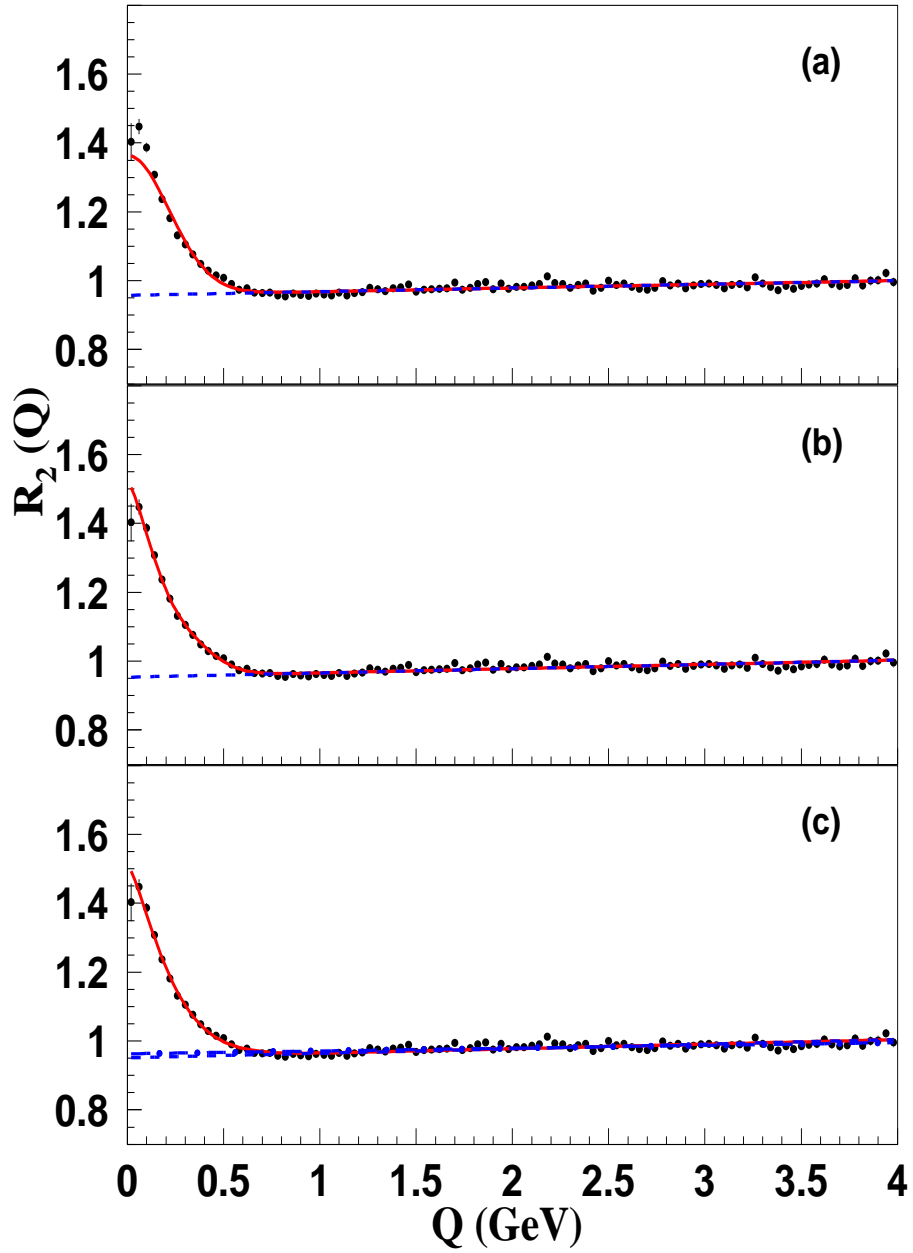


Figure 5.7: The Bose-Einstein correlation function R_2 for two-jet events with the (a) Gaussian, (b) Edgeworth, (c) symmetric Lévy fits. Dashed lines represent extrapolations of the long-range part, $\gamma(1 + \delta Q)$, of the fit. The dot-dashed line in (c) is the result of a fit of Eq. (5.11) with $\lambda = 0$ to the long-range part ($Q > 1.5$ GeV) of the correlation function.

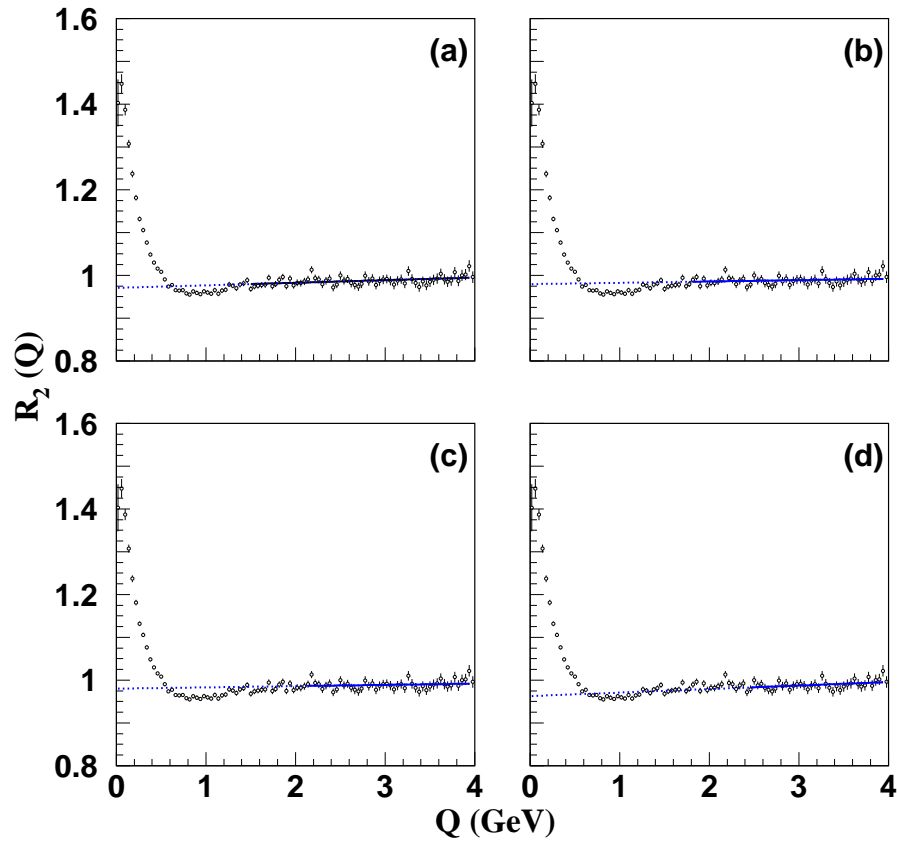


Figure 5.8: The Bose-Einstein correlation function R_2 for two-jet events. The solid lines are the results of fits of $R_2(Q) = \gamma(1 + \delta Q)$ to the long-range part of the correlation function. The fit range is $Q > 1.5$ GeV, 1.8 GeV, 2.1 GeV and 2.5 GeV in subfigures (a) – (d), respectively. The dotted lines are the extrapolation of the solid lines to the low Q region.

5.4 Summary

The main experimental facts found in this chapter can be summarized as follows:

First, using the Bertsch-Pratt parametrization, the source was found to be elongated by 20% – 30%. However, other parametrizations were found to suggest that the correlation function does not depend on the relative momentum components separately, but only on one of their possible combinations, namely the magnitude of the four-momentum difference, Q . This corresponds to a source that is spherically symmetric in the rest frame of the pion pairs. Given the smallness of the elongation in the BP frame, we therefore regard a simple Q dependence as a reasonably good approximation.

Investigating such a spherically symmetric shape of the source, the correlation function is fitted by three different parametrizations: Gaussian, Edgeworth and symmetric Lévy. The traditional (Gaussian) as well as the improved (Edgeworth and symmetric Lévy) forms fail.

The reason for the failure of the three forms described above is a dip below the line of $\gamma(1 + \delta Q)$ of the long-range correlations in the intermediate region $0.6 \text{ GeV} < Q < 1.5 \text{ GeV}$. In the next chapter we review how a mere dependence on Q can be explained theoretically by a model leading to a more natural and better description of the form of the correlation function. As a by-product of explaining the Q dependence, we will also find an explanation for the dipping behavior.

Chapter 6

Determination of the Proper Shape of BEC

In the previous chapter we have seen that in e^+e^- collisions Bose-Einstein correlations (BEC) depend, to a good approximation, only on the invariant momentum-difference Q and not on the components of Q separately. This is a non-trivial result, because this implies that in e^+e^- the BEC remain large if Q is small even if any of its components are large. For a hydrodynamical type of source, on the contrary, BEC decrease when any of the relative momentum components is large [31, 68]. A model which predicts such a mere Q dependence of BEC is the so-called τ -model [83] to be described below. As a by-product, this model also predicts a specific transverse mass dependence of R_2 , to be subjected to an experimental test here.

6.1 Physics of the τ -model

The τ -model was introduced to explain how one can obtain a merely Q dependent correlation function. It was introduced in response to comments by Goldhaber [30] and to the observation of TASSO [67] and Bowler [74] that indicated that in e^+e^- BEC is large if Q is small even when any of the components of Q are large.

The τ -model builds on the point-like nature of the e^+e^- collision. This point of collision thus has to be the center of particle production. In the τ -model, it is assumed that the average production point in the overall center-of-mass system, $\bar{x} = (\bar{t}, \bar{r}_x, \bar{r}_y, \bar{r}_z)$, of particles with a given four-momentum p is given by

$$\bar{x}^\mu(p^\mu) = a\tau p^\mu . \quad (6.1)$$

In the case of two-jet events, $\tau = \sqrt{\bar{t}^2 - \bar{r}_z^2}$ is the longitudinal proper-time and

$a = 1/m_t$, where $m_t = \sqrt{m^2 + p_t^2} = \sqrt{E^2 - p_z^2}$ is the transverse mass. For isotropically distributed particle production, the transverse mass is replaced by the mass in the definition of a , and τ is the proper-time, $\tau = \sqrt{t^2 - \bar{r}_x^2 - \bar{r}_y^2 - \bar{r}_z^2}$.

The second assumption is that the distribution of $x^\mu(p^\mu)$ about its average, $\delta_\Delta(x^\mu(p^\mu) - \bar{x}^\mu(p^\mu))$, is narrower than the proper-time distribution.

The emission function of the τ -model is defined as follows:

$$S(x, p) = \int_0^\infty d\tau H(\tau) \delta_\Delta(x - a\tau p) \rho_1(p), \quad (6.2)$$

where $H(\tau)$ is the (longitudinal) proper-time distribution, the function $\delta_\Delta(x - a\tau p)$ describes the strength of the correlation between coordinate space and momentum space variables and $\rho_1(p)$ is the experimentally measurable single-particle spectrum.

The two-pion distribution, $\rho_2(p_1, p_2)$, is related to $S(x, p)$, in the plane-wave approximation, by the Yano-Koonin formula [84]:

$$\rho_2(p_1, p_2) = \int d^4x_1 d^4x_2 S(x_1, p_1) S(x_2, p_2) (1 + \cos[(p_1 - p_2)(\bar{x}_1 - \bar{x}_2)]) . \quad (6.3)$$

In the spirit of a saddle-point approximation, approximating the δ_Δ function by a Dirac delta function, the momentum-integrated coordinate distribution function is

$$S(x) = \int d\tau \rho_1\left(\frac{x}{a\tau}\right) H(\tau) \quad (6.4)$$

and the argument of the cosine in Eq. (6.3) becomes

$$(p_1 - p_2)(\bar{x}_1 - \bar{x}_2) = (p_1 - p_2)(a_1\tau_1 p_1 - a_2\tau_2 p_2). \quad (6.5)$$

Note that

$$-Q^2 = (p_1 - p_2)^2 = p_1^2 + p_2^2 - 2p_1 p_2 = 2m^2 - 2p_1 p_2 \quad (6.6)$$

and

$$(p_1 - p_2)p_1 = p_1^2 - p_1 p_2 = m^2 - p_1 p_2 = -\frac{Q^2}{2}, \quad (6.7)$$

$$(p_1 - p_2)p_2 = p_1 p_2 - p_2^2 = p_1 p_2 - m^2 = +\frac{Q^2}{2}. \quad (6.8)$$

Finally, the argument of the cosine in Eq. (6.3) becomes

$$(p_1 - p_2)(\bar{x}_1 - \bar{x}_2) = -0.5(a_1\tau_1 + a_2\tau_2)Q^2. \quad (6.9)$$

Substituting Eqs. (6.4) and (6.9) in Eq. (6.3) leads to the following approximation of the two-particle BEC function:

$$R_2(p_1, p_2) = 1 + \lambda \text{Re} \tilde{H}\left(\frac{a_1 Q^2}{2}\right) \tilde{H}\left(\frac{a_2 Q^2}{2}\right), \quad (6.10)$$

where

$$\tilde{H}(w) = \int_0^\infty d\tau H(\tau) \exp(iw\tau) \quad (6.11)$$

is the Fourier-transform of $H(\tau)$. This general form can be simplified even further if one measures $R_2(p_1, p_2)$ in narrow intervals of a , so that $a_1 \approx a_2 \approx \bar{a}$:

$$R_2(p_1, p_2) = 1 + \lambda \text{Re} \tilde{H}^2 \left(\frac{\bar{a}Q^2}{2} \right). \quad (6.12)$$

In the case of two-jet events, the two-particle Bose-Einstein correlation function is then approximated by

$$R_2(p_1, p_2) = 1 + \lambda \text{Re} \tilde{H}^2 \left(\frac{Q^2}{2\bar{m}_t} \right). \quad (6.13)$$

Thus, for a given average of a of the two particles, R_2 is found to depend only on the invariant relative momentum Q . Further, the model also predicts a specific dependence on \bar{a} , which for two-jet events is a specific dependence on \bar{m}_t .¹

We shall now evaluate this formula for axially symmetric, two-jet like expansions and also for spherically symmetric expansions, and for various kinds of proper-time distribution.

6.2 Functional Dependence on Q

It is interesting to note, that for very strongly correlated coordinate and momentum space, the BEC depend on the relative momentum components only through the invariant combination Q , regardless of the shape of the proper-time distribution $H(\tau)$. In addition to that, the BEC depend on the transverse mass of the particles in case of cylindrically symmetric sources, while they depend on the mass of the particles for the case of a spherical symmetry. Besides, we do not have to make any assumptions on the functional form of the spatial distribution of the source (apart from some symmetry).

In this section, let us consider the case of cylindrically symmetric expansions, corresponding to $e^+e^- \rightarrow$ two-jet events, and see how various choices for the proper-time distribution result in various shapes for BEC.

6.2.1 Symmetric Parametrizations

Obviously, the proper time is a variable that satisfies $\tau \geq 0$, where $\tau = 0$ is defined as the proper time of the e^+e^- collision. This means that the distribution must be one-sided. Hence, symmetric laws can only approximate the proper-time distribution. The condition $\tau_m \gg \Delta\tau$ must be satisfied, where τ_m

¹In the initial formulation of the τ -model this dependence was averaged over [83] due to the lack of transverse mass dependent data at that time.

is the position of the maximum of $H(\tau)$ and $\Delta\tau$ its width, in order that the weight of the distribution in the $\tau \leq 0$ region be negligible.

Gaussian longitudinal proper-time dependence

Again, we start with the simplest assumption that the proper-time has a Gaussian distribution:

$$H(\tau) = \frac{1}{\sqrt{2\pi}\Delta\tau^2} \exp\left(-\frac{(\tau - \tau_m)^2}{2\Delta\tau^2}\right), \quad (6.14)$$

where τ_m is the mean of the Gaussian distribution. The characteristic function (Fourier transform) of Eq. (6.14) is

$$\tilde{H}(\omega) = \exp\left(i\tau_m\omega - \frac{1}{2}(\Delta\tau\omega)^2\right), \quad (6.15)$$

and hence

$$\tilde{H}\left(\frac{\bar{a}Q^2}{2}\right) = \exp\left(\frac{i\tau_m\bar{a}Q^2}{2} - \frac{1}{2}\left(\frac{\Delta\tau\bar{a}Q^2}{2}\right)^2\right). \quad (6.16)$$

Substituting Eq. (6.16) into Eq. (6.12) with a long-range correlation term and a normalization factor we obtain an approximately Gaussian correlation function in terms of Q^2 , with an oscillating pre-factor:

$$R_2(Q) = \gamma(1 + \delta Q) \left[1 + \lambda \cos(\tau_m\bar{a}Q^2) \exp\left(-\left(\frac{\Delta\tau\bar{a}Q^2}{2}\right)^2\right) \right]. \quad (6.17)$$

In the case of two-jet events, the corresponding correlation function has the form:

$$R_2(Q) = \gamma(1 + \delta Q) \left[1 + \lambda \cos\left(\frac{\tau_m Q^2}{\bar{m}_t}\right) \exp\left(-\left(\frac{\Delta\tau Q^2}{2\bar{m}_t}\right)^2\right) \right]. \quad (6.18)$$

This oscillation term causes a dip in $R_2(Q)$. Thus we have identified yet another feature of the τ -model which is in qualitative agreement with the data.

Symmetric Lévy stable longitudinal proper-time dependence

We also investigate the possibility that the proper-time distribution is characterized by a Lévy distribution, where the simplest case corresponds to the class of symmetric distributions. In this case, the longitudinal proper-time distribution has the following asymptotic shape:

$$H(\tau) \approx \frac{1}{|\tau - \tau_m|^{1+\alpha}}, \quad (6.19)$$

which is symmetric under a reflection with respect to $\tau = \tau_m$ and decreases as a power law for large values of proper-time. The Lévy stable distributions with $\alpha < 2$ are characterized by a non-analytic behavior of their Fourier transform around zero. The corresponding BEC function is found to be [37]

$$R_2(Q) = \gamma(1 + \delta Q) \left[1 + \lambda \cos(\tau_m \bar{a} Q^2) \exp\left(-\left(\frac{\Delta\tau \bar{a} Q^2}{2}\right)^\alpha\right) \right], \quad (6.20)$$

and the corresponding two-jet event correlation function is

$$R_2(Q) = \gamma(1 + \delta Q) \left[1 + \lambda \cos\left(\frac{\tau_m Q^2}{\bar{m}_t}\right) \exp\left(-\left(\frac{\Delta\tau Q^2}{2\bar{m}_t}\right)^\alpha\right) \right], \quad (6.21)$$

where the case of a Gaussian distribution considered above is obtained for $\alpha = 2$.

6.2.2 Results for the Symmetric Parametrizations

For two-jet events, fits of Eq. (6.18), corresponding to the Gaussian longitudinal proper-time distribution of Eq. (6.14), result in a statistically unacceptable χ^2 , as summarized for various \bar{m}_t intervals in Table 6.1 and shown in Fig. 6.1. Note that the assumption that $m_{t_1} \approx m_{t_2} \approx \bar{m}_t$ is not required here.

On the other hand, the fit with a symmetric Lévy-stable longitudinal proper-time distribution results in statistically acceptable χ^2 at $\bar{m}_t \lesssim 0.6$ GeV, as shown in Table 6.2. However, an important problem with many of these fits is that τ_m is found to be smaller than $\Delta\tau$. Thus, the a priori condition of validity of these parametrizations, $\Delta\tau \ll \tau_m$, is violated.

In physical terms, this indicates two points:

1. Particle emission seems to be maximal for very small values of the longitudinal proper time τ .
2. Due to this reason and the constraint of $\tau \geq 0$, a symmetric proper-time distribution cannot be utilized to describe the time evolution of particle emission in these reactions.

6.2.3 One-sided Parametrization

The τ model with m_t dependence

A more appropriate form of the longitudinal proper-time distribution corresponds to the asymmetric class of stable distributions, in particular, when the asymmetry parameter is fixed to $\beta = 1$, in which case the support of these distributions is bounded from below. For our case this corresponds to a certain

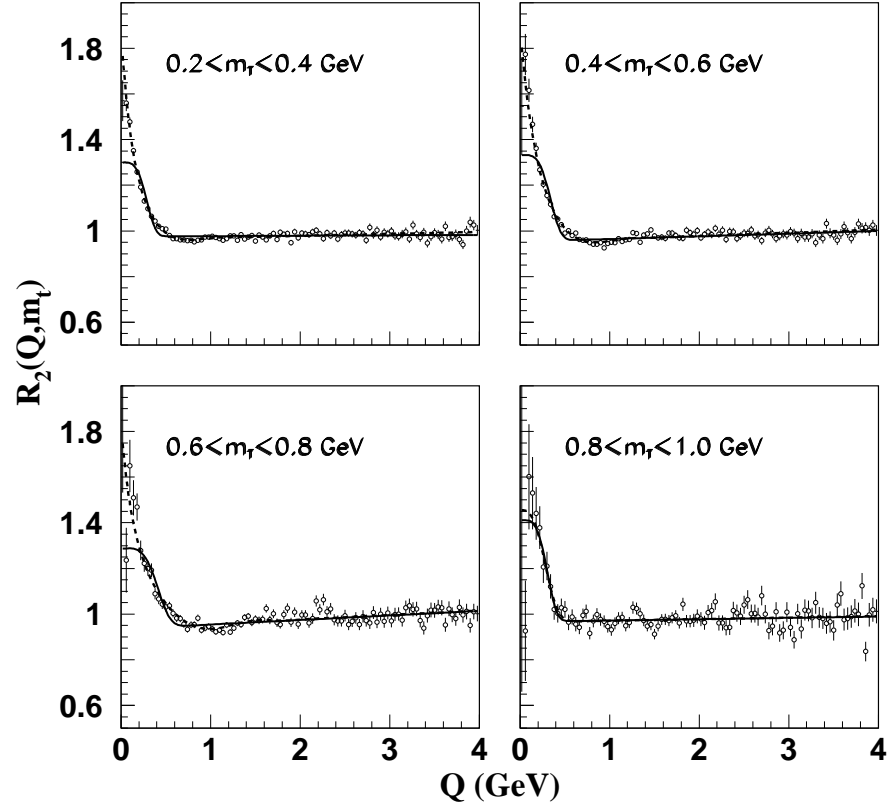


Figure 6.1: The Bose-Einstein correlation function R_2 for two-jet events with the result of a fit of the Gaussian proper-time distribution (solid line), Eq. (6.18), and the symmetric Lévy proper-time distribution (dashed line), Eq. (6.21), for various \overline{m}_t intervals.

\overline{m}_t (GeV)	0.2 – 0.4	0.4 – 0.6	0.6 – 0.8	0.8 – 1.0
γ	0.975 ± 0.004	0.953 ± 0.003	0.934 ± 0.005	0.97 ± 0.01
λ	0.33 ± 0.01	0.40 ± 0.02	0.38 ± 0.09	0.46 ± 0.10
τ_m (fm)	0.14 ± 0.64	0.76 ± 0.85	0.26 ± 29.6	0.31 ± 8.2
$\Delta\tau$ (fm)	3.1 ± 0.1	3.6 ± 0.2	3.5 ± 1.4	1.61 ± 1.82
δ (GeV $^{-1}$)	0.002 ± 0.002	0.012 ± 0.002	0.021 ± 0.003	0.006 ± 0.003
χ^2/NDF	518 / 95	311 / 95	197 / 95	122 / 95
CL (%)	10^{-59}	10^{-22}	10^{-7}	3

Table 6.1: Results of fitting Eq. (6.18), corresponding to the Gaussian proper-time distribution of Eq. (6.14), for two-jet events in various intervals of \overline{m}_t .

\overline{m}_t (GeV)	0.2 – 0.4	0.4 – 0.6	0.6 – 0.8	0.8 – 1.0
γ	0.961 ± 0.003	0.949 ± 0.003	0.937 ± 0.005	0.96 ± 0.01
λ	0.97 ± 0.02	1.00 ± 0.02	1.00 ± 0.06	0.51 ± 0.12
τ_m (fm)	0.23 ± 0.02	0.33 ± 0.02	0.35 ± 0.02	0.05 ± 0.15
$\Delta\tau$ (fm)	2.45 ± 0.23	2.46 ± 0.16	3.12 ± 0.36	1.72 ± 0.43
α	0.47 ± 0.02	0.49 ± 0.02	0.41 ± 0.02	1.52 ± 0.58
χ^2/NDF	106 / 94	130 / 94	138 / 94	122 / 94
CL (%)	19	1	0.2	3

Table 6.2: Results of fitting Eq. (6.21), corresponding to the symmetric Lévy proper-time distribution, for two-jet events in various intervals of \overline{m}_t . Note that the physical condition $\Delta\tau \ll \tau_m$ is violated.

lower limit $\tau_0 < \tau$ on the random variable τ . The characteristic function of the asymmetric stable distribution, for $\alpha \neq 1$, can be written [81] as follows:

$$\tilde{H}(\omega) = \exp\left(-\frac{1}{2}\Delta\tau^\alpha|\omega|^\alpha + i\frac{\beta}{2}\Delta\tau^\alpha|\omega|^\alpha\text{sign}(\omega)\tan\left(\frac{\alpha\pi}{2}\right) + i\omega\tau_0\right). \quad (6.22)$$

For the special case of $\alpha = 1$, see [81]. In the symmetric case $\beta = 0$ and Eq. (4.37) is obtained. Squaring Eq. (6.22) and setting $\beta = 1$, yields

$$\tilde{H}^2(\omega) = \exp\left(-\Delta\tau^\alpha|\omega|^\alpha + i\Delta\tau^\alpha|\omega|^\alpha\tan\left(\frac{\alpha\pi}{2}\right) + 2i\omega\tau_0\right) \quad (6.23)$$

and

$$\text{Re}\tilde{H}^2\left(\frac{\bar{a}Q^2}{2}\right) = \cos\left(\tau_0\bar{a}Q^2 + \tan\left(\frac{\alpha\pi}{2}\right)\left(\frac{\Delta\tau\bar{a}Q^2}{2}\right)^\alpha\right)\exp\left(-\left(\frac{\Delta\tau\bar{a}Q^2}{2}\right)^\alpha\right). \quad (6.24)$$

The corresponding Bose-Einstein correlation function has an analytic, al-

though somewhat complicated form:

$$R_2(Q, \bar{a}) = \gamma (1 + \delta Q) \left[1 + \lambda \cos \left(\tau_0 \bar{a} Q^2 + \tan \left(\frac{\alpha \pi}{2} \right) \left(\frac{\Delta \tau \bar{a} Q^2}{2} \right)^\alpha \right) \exp \left(- \left(\frac{\Delta \tau \bar{a} Q^2}{2} \right)^\alpha \right) \right] \quad (6.25)$$

and the corresponding two-jet event correlation function is

$$R_2(Q, \bar{m}_t) = \gamma (1 + \delta Q) \left[1 + \lambda \cos \left(\frac{\tau_0 Q^2}{\bar{m}_t} + \tan \left(\frac{\alpha \pi}{2} \right) \left(\frac{\Delta \tau Q^2}{2 \bar{m}_t} \right)^\alpha \right) \exp \left(- \left(\frac{\Delta \tau Q^2}{2 \bar{m}_t} \right)^\alpha \right) \right], \quad (6.26)$$

where τ_0 is the proper time of the onset of particle production. If the particle emission starts immediately after the collision, this corresponds to the $\tau_0 \rightarrow 0$ limit.

The τ model for average a

Before proceeding to fits of Eq. (6.26), we first consider a simplification of the equation obtained by assuming (a) that particle production starts immediately, i.e., $\tau_0 = 0$, and (b) an average \bar{a} -dependence. Assumption (b) is implemented in an approximate way by defining an effective radius $R = \sqrt{\Delta \tau \bar{a} / 2}$, which for two-jet events becomes $R = \sqrt{\Delta \tau / (2 \bar{m}_t)}$. This results in the following, relatively simple form:

$$R_2(Q) = \gamma (1 + \delta Q) \left[1 + \lambda \cos [(R_a Q)^{2\alpha}] \exp \left(-(RQ)^{2\alpha} \right) \right], \quad (6.27)$$

where R_a is related to R by

$$R_a^{2\alpha} = \tan \left(\frac{\alpha \pi}{2} \right) R^{2\alpha}. \quad (6.28)$$

6.2.4 Results for the Asymmetric Parametrization with Average a

Fits of Eq. (6.27) are first performed with R_a as a free parameter. The fit results are listed in Table 6.3 for all events and for the two- and three-jet event samples. The first error is statistical and the second error is systematic (the contributions to the systematic errors are summarized in the following section), and shown in Figs. 6.2a, 6.2b and 6.2c, respectively. They have acceptable confidence levels, describing well the dip below unity in the 0.6–1.5 GeV region, as well as the low- Q peak.

The fit parameters for the two-jet events satisfy Eq. (6.28). However, those for all and three-jet events do not. We note that the values of the parameters λ, R_a and α do not differ greatly between the samples. However, these parameters are rather highly correlated (in the fit for all events, the correlation

coefficients are $\rho(\lambda, R) = 0.95$, $\rho(\lambda, \alpha) = -0.67$ and $\rho(R, \alpha) = -0.61$, which makes the simple calculation of the statistical significance of differences in the parameters unreliable.

Fit results imposing Eq. (6.28) are given in Table 6.4 and shown in Figs. 6.3a, 6.3b and 6.3c. For two-jet events, the values of the parameters are the same as in the fit with R_a free—only the uncertainties have changed. For all events and three-jet events, the introduction of Eq. (6.28) results in values of α and R closer to those for two-jet events, but the confidence level is very bad, a consequence of incompatibility with Eq. (6.28). Since a is known for two-jet events, we focus on this class of events in the remaining sections of this thesis.

parameter	all	three-jet	two-jet
γ	0.997 ± 0.003	1.01 ± 0.01	$0.979 \pm 0.005 \pm_{0.013}^{0.045}$
λ	0.73 ± 0.02	0.84 ± 0.03	$0.67 \pm 0.03 \pm_{0.19}^{0.11}$
R (fm)	0.81 ± 0.03	0.89 ± 0.03	$0.79 \pm 0.04 \pm_{0.17}^{0.07}$
R_a (fm)	0.81 ± 0.02	0.88 ± 0.03	$0.59 \pm 0.03 \pm_{0.11}^{0.42}$
α	0.38 ± 0.01	0.35 ± 0.02	$0.42 \pm 0.02 \pm_{0.11}^{0.03}$
δ (GeV $^{-1}$)	0.003 ± 0.001	-0.003 ± 0.002	$0.003 \pm 0.002 \pm_{0.013}^{0.003}$
χ^2/NDF	98/94	102/94	97/94
CL (%)	37	27	40

Table 6.3: Results of fits of Eq. (6.27) for all, three-jet and two-jet events.

parameter	all	three-jet	two-jet
γ	0.973 ± 0.001	0.972 ± 0.001	$0.979 \pm 0.005 \pm_{0.007}^{0.010}$
λ	0.69 ± 0.03	0.77 ± 0.02	$0.67 \pm 0.03 \pm_{0.19}^{0.12}$
R (fm)	0.79 ± 0.03	0.85 ± 0.02	$0.79 \pm 0.03 \pm_{0.12}^{0.06}$
α	0.45 ± 0.01	0.44 ± 0.01	$0.42 \pm 0.01 \pm_{0.03}^{0.04}$
δ (GeV $^{-1}$)	0.009 ± 0.001	0.010 ± 0.001	$0.003 \pm 0.001 \pm_{0.04}^{0.12}$
χ^2/NDF	175/95	174/95	97/95
CL (%)	10^{-4}	10^{-4}	42

Table 6.4: Results of fits of Eq. (6.27) imposing Eq. (6.28) for all, three-jet and two-jet events. The first errors are statistical. The second errors are systematic, determined for the two-jet events only.

6.2.5 The Dependence on \overline{m}_t

The result of the fits of Eq. (6.26) is presented in Table 6.5 and shown in Fig. 6.4. The quality of the fits is acceptable. From Fig. 6.5, the parameters appear to be independent of \overline{m}_t within errors.

To satisfy the assumption $a_1 \approx a_2 \approx \bar{a}$ made in deriving Eq. (6.12), we now require that the difference in transverse mass of the two pions be less than 0.2

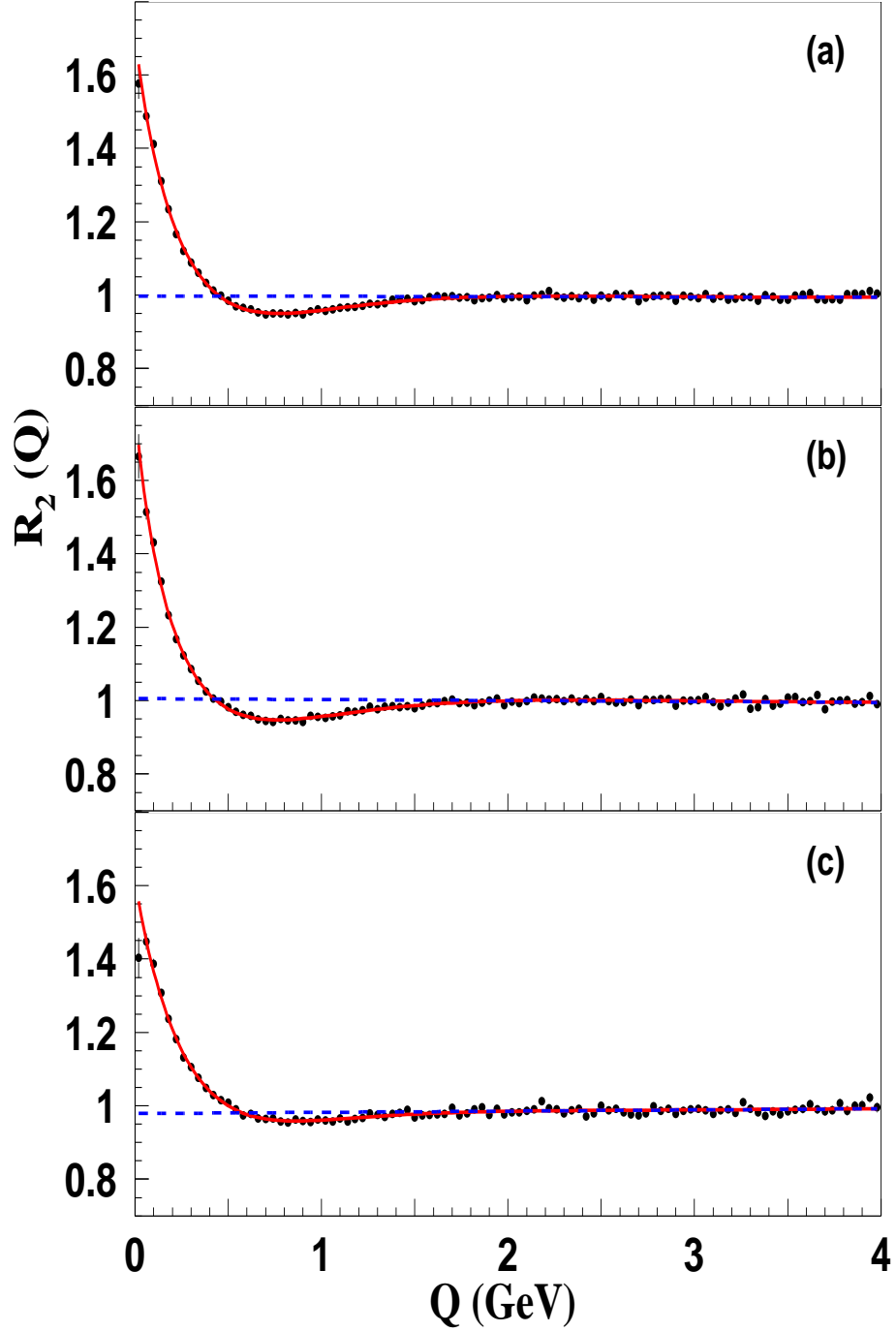


Figure 6.2: The Bose-Einstein correlation function R_2 for all events (a), three-jet events (b) and two-jet events (c). The curve corresponds to the fit of the asymmetric Lévy parametrization, Eq. (6.27), without taking into account the constraint given by Eq. (6.28). The dashed line represents the long-range part of the fit, i.e., $\gamma(1 + \delta)$.

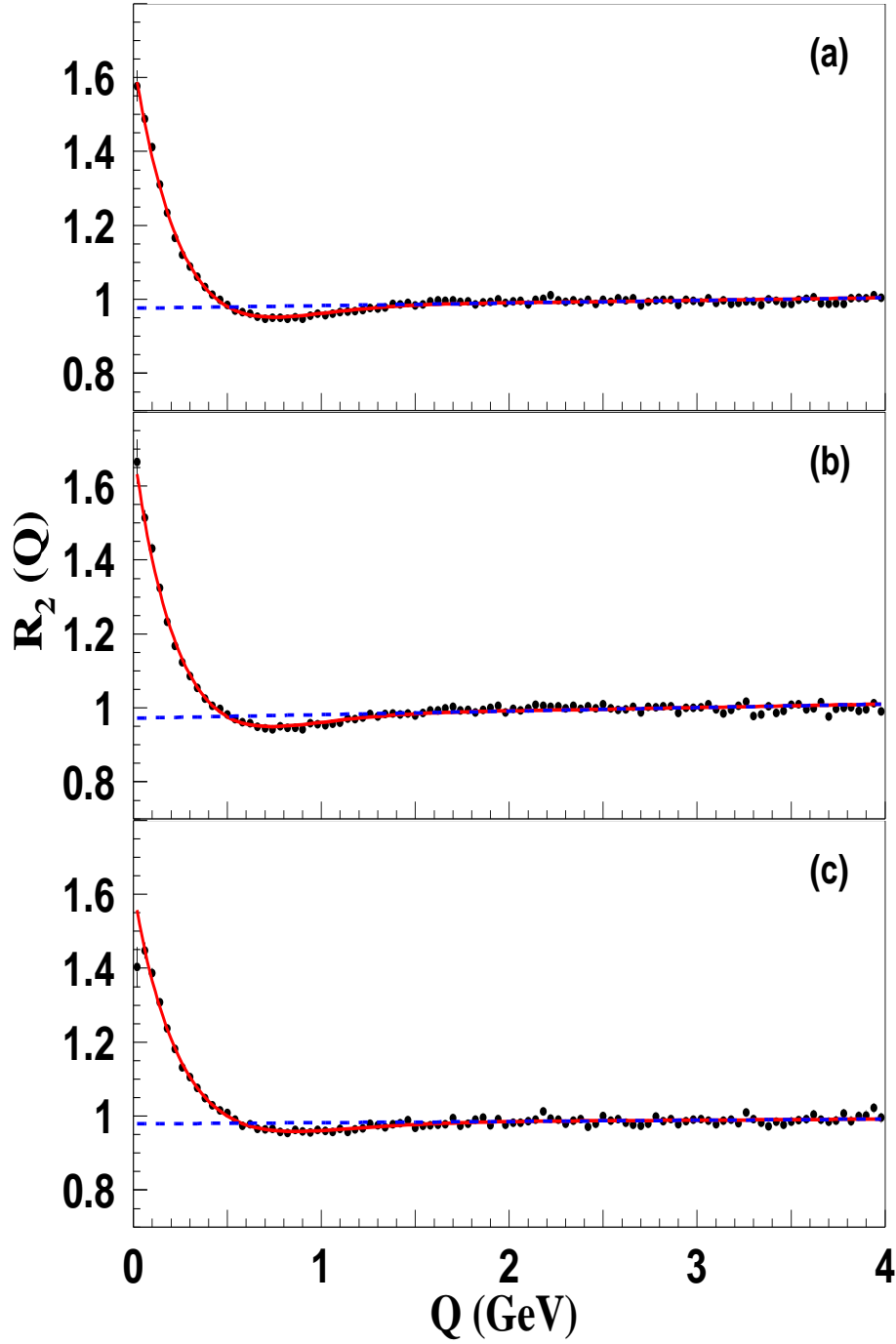


Figure 6.3: The Bose-Einstein correlation function R_2 for all events (a) and three-jet events (b) and two-jet events (c). The curve corresponds to the fit of the asymmetric Lévy parametrization, Eq. (6.27), with also applying the constraint given by Eq. (6.28). The dashed line represents the long-range part of the fit, i.e., $\gamma(1 + \delta)$.

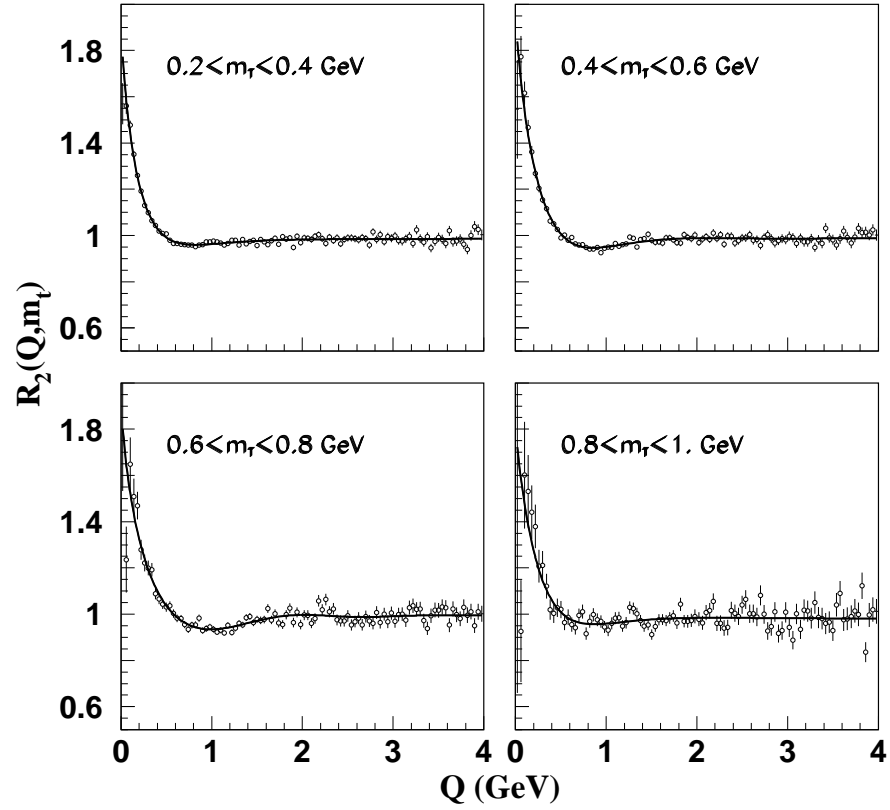


Figure 6.4: The Bose-Einstein correlation function R_2 for two-jet events with the result of a fit of the asymmetric Lévy parametrization, Eq. (6.26), for various \bar{m}_t intervals.

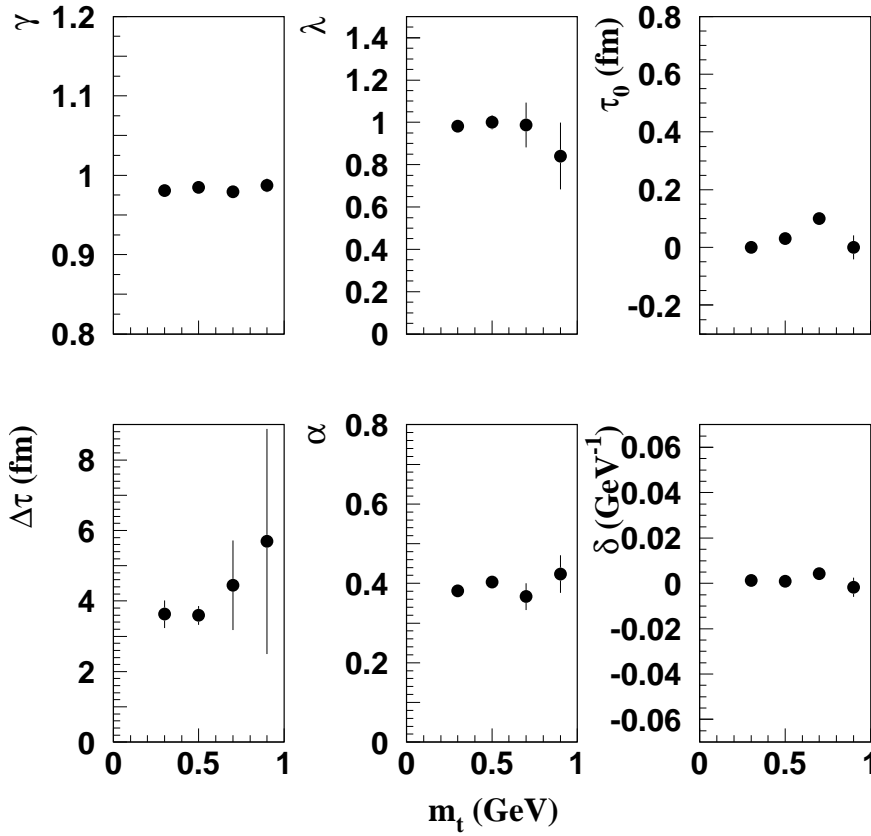


Figure 6.5: The values of the parameters of Eq. (6.26) found in fits for various \overline{m}_t intervals.

\overline{m}_t (GeV)	0.2 – 0.4	0.4 – 0.6	0.6 – 0.8	0.8 – 1.0
γ	0.981 ± 0.003	0.985 ± 0.003	0.979 ± 0.005	0.99 ± 0.01
λ	0.98 ± 0.02	1.00 ± 0.04	0.99 ± 0.18	0.84 ± 0.16
τ_0 (fm)	0.00 ± 0.03	0.03 ± 0.02	0.10 ± 0.04	0.00 ± 0.04
$\Delta\tau$ (fm)	3.63 ± 0.15	3.59 ± 0.10	4.5 ± 0.8	5.7 ± 1.5
α	0.381 ± 0.004	0.40 ± 0.01	0.37 ± 0.02	0.42 ± 0.03
δ (GeV ⁻¹)	0.001 ± 0.002	0.001 ± 0.002	0.004 ± 0.003	-0.002 ± 0.004
χ^2/NDF	107 / 94	108 / 94	120 / 94	130 / 94
CL (%)	17	15	4	1

Table 6.5: Fit results with Eq. (6.26), corresponding to the asymmetric proper-time distribution, for two-jet events in various intervals of \overline{m}_t .

parameter	$0.2 < \overline{m}_t < 0.4$	$0.4 < \overline{m}_t < 0.6$
γ	$0.976 \pm 0.004^{+0.033}_{-0.013}$	$0.988 \pm 0.006^{+0.006}_{-0.032}$
λ	$0.92 \pm 0.04^{+0.18}_{-0.51}$	$0.91 \pm 0.06^{+0.24}_{-0.59}$
τ_0 (fm)	$0.00 \pm 0.01^{+0.08}_{-0}$	$0.00 \pm 0.04^{+0.17}_{-0}$
$\Delta\tau$ (fm)	$2.76 \pm 0.28^{+2.12}_{-2.06}$	$1.57 \pm 0.19^{+0.89}_{-0.30}$
α	$0.40 \pm 0.01^{+0.13}_{-0.06}$	$0.49 \pm 0.02^{+0.01}_{-0.14}$
δ (GeV ⁻¹)	$0.003 \pm 0.002^{+0.006}_{-0.012}$	$-0.004 \pm 0.003^{+0.03}_{-0.004}$
χ^2/NDF	105 / 94	77 / 94
CL (%)	21	90
parameter	$0.6 < \overline{m}_t < 0.8$	$0.8 < \overline{m}_t < 1.0$
γ	$0.972 \pm 0.011^{+0.056}_{-0.13}$	$0.927 \pm 0.026^{+0.090}_{-0.079}$
λ	$0.96 \pm 0.09^{+0.07}_{-0.78}$	$0.65 \pm 0.21^{+0.51}_{-0.93}$
τ_0 (fm)	$0.00 \pm 0.04^{+0.12}_{-0}$	$0.00 \pm 0.15^{+0.34}_{-0}$
$\Delta\tau$ (fm)	$1.55 \pm 0.23^{+6.01}_{-1.34}$	$1.65 \pm 0.79^{+4.42}_{-1.75}$
α	$0.50 \pm 0.02^{+0.16}_{-0.24}$	$0.58 \pm 0.09^{+1.31}_{-0.77}$
δ (GeV ⁻¹)	$0.002 \pm 0.006^{+0.051}_{-0.023}$	$0.005 \pm 0.013^{+0.106}_{-0.012}$
χ^2/NDF	117 / 94	104 / 94
CL (%)	5.4	23

Table 6.6: Fit results with Eq. (6.26), corresponding to the asymmetric proper-time distribution, for two-jet events in various intervals of \overline{m}_t in GeV requiring that the transverse mass of the pions be similar.

GeV. The resulting fits are shown for typical \overline{m}_t intervals in Fig. 6.6, and the values of the parameters obtained in the fits are shown in Fig. 6.7 and Table 6.6. The quality of these fits is improved compared to the fits of Table 6.5, while the values of $\Delta\tau$ are smaller and those of α somewhat larger. The fitted values of the model parameters are stable and within errors independent of \overline{m}_t , confirming the expectation of the τ -model. We conclude that the τ -model with a one-sided Lévy proper-time distribution describes the data with parameters

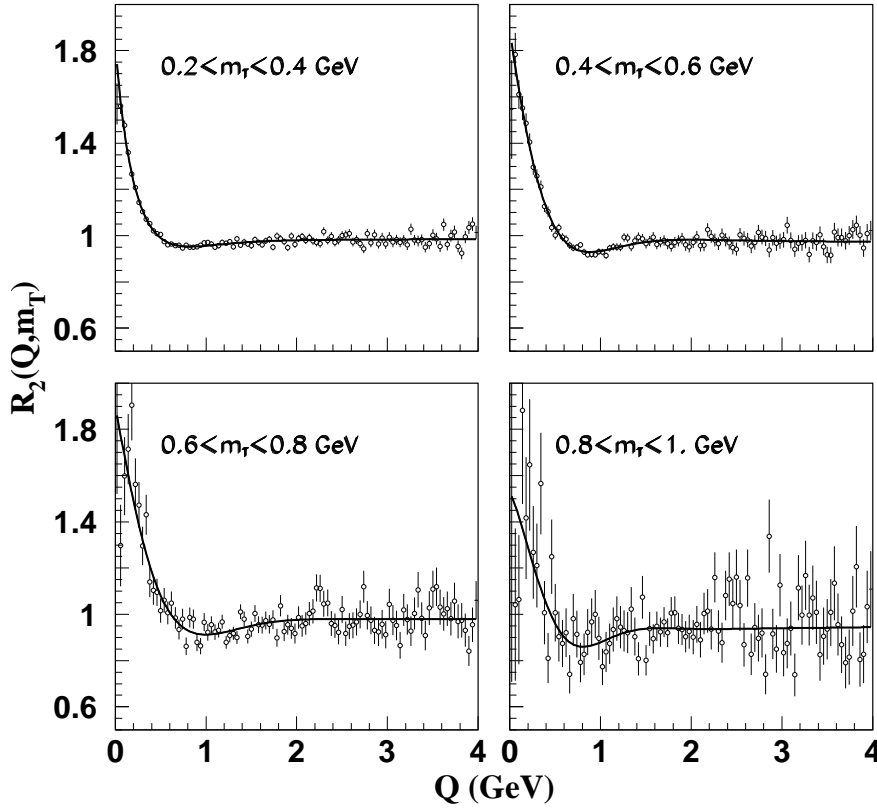


Figure 6.6: The Bose-Einstein correlation function R_2 for two-jet events with the result of a fit of the asymmetric Lévy parametrization, Eq. (6.26), for various \overline{m}_t intervals requiring that the transverse mass of the pions be similar (i.e. the difference less than 0.2 GeV).

$\tau_0 = 0 \pm 0.01$ fm, $\alpha = 0.43 \pm 0.03$ and $\Delta\tau = 1.8 \pm 0.4$ fm. (The values are the weighted averages of the corresponding values found for the four \overline{m}_t intervals. The errors include systematic uncertainties.)

It is of particular interest to point out the \overline{m}_t dependence of the ‘width’ of the source. In Eq. (6.26) the parameter associated with the width is $\Delta\tau$. Note that it enters Eq. (6.26) as $\Delta\tau Q^2 / \overline{m}_t$. In a Gaussian parametrization the radius R enters the parametrization as $R^2 Q^2$. Our observance that $\Delta\tau$ is independent of \overline{m}_t thus corresponds to $R \propto 1/\sqrt{\overline{m}_t}$ and can be interpreted as confirmation of the observance [82, 85, 86] of such a dependence of the Gaussian radii in 2- and 3-dimensional analyses of Z decays.

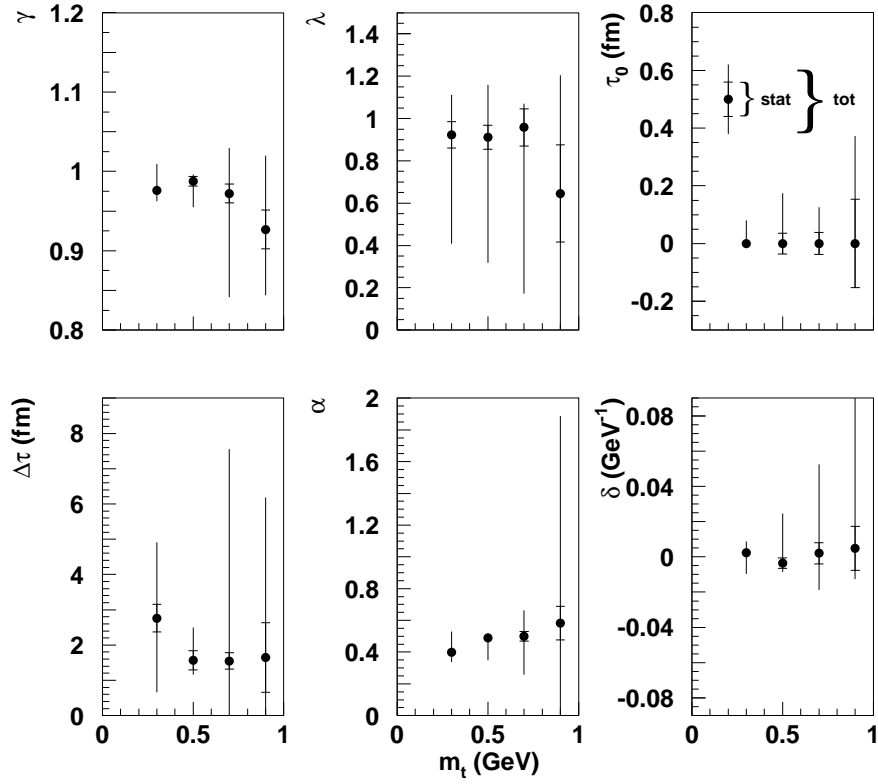


Figure 6.7: The values of the parameters of Eq. (6.26) found in fits for various \overline{m}_t intervals requiring that the transverse mass of the pions be similar. Statistical and systematic errors are added in quadrature to obtain the total errors on the fit parameters.

6.2.6 Systematic Uncertainties on Fitted Results

The systematic uncertainties are estimated, as described in Sect. 4.7, only for two-jet events since \bar{a} is known for two-jet events. Table 6.7 presents the contributions to the total systematic error from the various sources on fits of Eq. (6.27), while Table 6.8 shows the contributions to the total systematic uncertainties for one of the \bar{m}_t intervals on fits of Eq. (6.26). The main source of the systematic error is the choice of the Monte Carlo simulation.

6.2.7 Controlling the τ -model with additional measurements

Within the framework of the τ -model, we exploit the prediction of this model, namely that the Bose-Einstein correlation function depends only on the invariant momentum-difference Q . However, earlier studies [63–66, 82] showed that the region of homogeneity is elongated along the thrust direction. In this section we make a check of the validity of the τ -model.

Using the BP parametrization, a 3-dimensional histogram is fitted by the main equation of the τ -model, Eq. (6.26), for two-jet events. The value of Q is calculated from the BP variables at the center of each bin, and the transverse mass is set to 0.3 GeV (the average of the transverse mass distribution). The resulting values of the main parameters are: $\tau_0 = 0.0 \pm 0.4$ fm, $\alpha = 0.41 \pm 0.01$ and $\Delta\tau = 2.3 \pm 0.1$ fm. These are consistent with the values obtained in fits of the Q distribution for various \bar{m}_t intervals (Table 6.6). However, the confidence level of the fit is low: 10^{-19} ($\chi^2/\text{NDF} = 2829/2191$). We attribute this low confidence level to the elongation of the region of homogeneity observed in the LCMS which is inconsistent with the strict Q dependence of the τ -model. However, the consistency observed in the resulting parameters suggests that the τ -model provides a reasonable approximation.

As another check, a combined fit is made for the four \bar{m}_t intervals. The main parameters, τ_0 , α and $\Delta\tau$, are constrained to be the same for each \bar{m}_t interval. The resulting values are: $\tau_0 = 0.0 \pm 0.01$ fm, $\alpha = 0.43 \pm 0.01$ and $\Delta\tau = 2.2 \pm 0.2$ fm. The quality of the fit is acceptable: $\chi^2/\text{NDF} = 446/385$, from which the confidence level is 2%.

In conclusion, we find that the τ -model describes the Bose-Einstein correlation data of two-jet events in L3, even if these data are taken in terms of the Bertsch-Pratt variables, despite the fact that the correlation function depends on Q and \bar{m}_t , while the effective source is known to be elongated in terms of the Bertsch-Pratt parametrization.

	α		R		R_a		λ		δ		γ	
	+	-	+	-	+	-	+	-	+	-	+	-
2-jet	R_a free											
Track	0.01	0.03	0.03	0.06	0.07	0	0.04	0.05	0	0.002	0.011	0
Event	0.01	0.04	0.05	0.02	0.07	0	0.05	0.01	0.001	0.005	0.012	0
Fit Range/ δ	0	0.01	0.01	0	0.02	0	0.005	0	0	0.002	0.003	0
Mix strategy	0.01	0.01	0.02	0.02	0.03	0.07	0.04	0.02	0.001	0.002	0.005	0.008
MC choice	0.02	0.07	0.01	0.15	0.37	0.08	0.06	0.17	0.002	0.008	0.031	0.010
Combined	0.03	0.11	0.07	0.17	0.42	0.11	0.11	0.19	0.003	0.013	0.045	0.013
Statistical	0.02		0.04		0.03		0.03		0.002		0.005	
2-jet	R_a constrained by Eq. (6.28)											
Track	0.025	0	0.03	0.06			0.025	0.06	0.001	0.001	0.003	0.002
Event	0.01	0.01	0.04	0.02			0.01	0.02	0.007	0.001	0.003	0.001
Fit Range/ δ	0.01	0	0	0.02			0	0.02	0	0.003	0.006	0
Mix strategy	0.01	0.01	0.02	0.02			0.05	0.01	0.001	0.001	0.002	0.001
MC choice	0.03	0.02	0.02	0.08			0.08	0.17	0.009	0.001	0.005	0.007
Combined	0.04	0.03	0.06	0.12			0.12	0.19	0.012	0.004	0.010	0.007
Statistical	0.01		0.03				0.03		0.001		0.005	

Table 6.7: Systematic uncertainties on results of fits of Eq. (6.27).

	α		τ_0		$\Delta\tau$		λ		δ		γ	
	+	-	+	-	+	-	+	-	+	-	+	-
2-jet	R_a constrained by Eq. (6.28)											
Track	0.00	0.05	0.001	0.00	0.46	0.00	0.17	0.00	0.010	0.000	0.001	0.013
Event	0.00	0.03	0.002	0.00	0.34	0.09	0.10	0.02	0.013	0.000	0.003	0.017
Fit Range/ δ	0.00	0.03	0.000	0.00	0.10	0.00	0.00	0.01	0.000	0.002	0.000	0.004
Mix strategy	0.00	0.30	0.000	0.00	0.46	0.00	0.13	0.00	0.007	0.000	0.000	0.003
MC choice	0.01	0.12	0.170	0.00	0.50	0.28	0.00	0.59	0.019	0.003	0.005	0.023
Combined	0.01	0.14	0.17	0.00	0.89	0.30	0.24	0.59	0.028	0.004	0.006	0.032
Statistical	0.02		0.04		0.19		0.06		0.003		0.003	

Table 6.8: Systematic uncertainties on results of fits of Eq. (6.26) when \overline{m}_t is between 0.4 – 0.6 GeV.

6.3 Summary and Conclusions

In this chapter, firstly the τ -model was described. This model explains the experimental observation that BEC in e^+e^- reactions depend only on Q rather than on the components of Q separately. It also predicts a specific transverse mass dependence of R_2 for two-jet events, and it also provides a natural explanation for the anti-correlation seen in the L3 Bose-Einstein correlation data.

Secondly, various choices for the proper-time distribution were considered. The symmetric parametrizations fail in physical terms since particle production cannot start before the collision. Hence, we tried a one-sided distribution, namely a one-sided Lévy distribution.

The quality of the fits of one-sided distributions is seen to be statistically acceptable. Further, an \overline{m}_t dependence is observed for two-jet events, confirming the expectation of the τ -model. We conclude that the τ -model with one-sided Lévy proper-time distribution describes the two-jet event data with parameters $\tau_0 = 0 \pm 0.01$ fm, $\alpha = 0.43 \pm 0.03$ and $\Delta\tau = 1.8 \pm 0.4$ fm.

Finally, we have performed a control measurement, by fitting the correlation function of the τ -model to the Bose-Einstein correlation function of two-jet events measured and binned in terms of the usual Bertsch-Pratt variables, where an elongation of the source was observed in the thrust direction. We found that the analytic form of the τ -model, given by Eq. (6.26), describes these data with a statistically acceptable confidence level. The best values of the fit parameters of the τ -model obtained in this control measurement agree within errors with the parameters obtained directly from the fits with Eq. (6.26) to the correlation function measured in the Q variable in various \overline{m}_t intervals.

Chapter 7

Reconstruction of the Emission Function

With the help of the τ -model and with a few additional assumptions, we use measurements of Bose-Einstein Correlations (BEC) together with single-particle inclusive spectra to reconstruct the space-time evolution of hadronization in two-jet events.

7.1 The Emission Function of Two-jet Events

The emission function in configuration space, $S(x)$, is the proper-time derivative of the integral over p of $S(x, p)$, which in the τ -model is given by Eq. (6.2). Approximating δ_Δ by a Dirac delta function, we find [87–89]

$$S(x) = \frac{d^4 n}{d\tau d^3 x} = \left(\frac{m_t}{\tau}\right)^3 H(\tau) \rho_1\left(p = \frac{m_t x}{\tau}\right). \quad (7.1)$$

Note that if δ_Δ is a sufficiently (but not infinitely) narrow function, a saddle-point integration leads to the same results.

To simplify the reconstruction of $S(x)$ we assume that it can be factorized in the following way:

$$S(r, z, t) = I(r)G(\eta)H(\tau), \quad (7.2)$$

where $I(r)$ is the single-particle transverse distribution, $G(\eta)$ is the space-time rapidity distribution of particle production, and $H(\tau)$ is the proper-time distribution. From the strongly correlated phase space of the τ -model, $\eta = y$ and $r = p_t \tau / m_t$. Hence,

$$G(\eta) = N_y(\eta), \quad (7.3)$$

$$I(r) = \left(\frac{m_t}{\tau}\right)^3 N_{p_t}(r m_t / \tau), \quad (7.4)$$

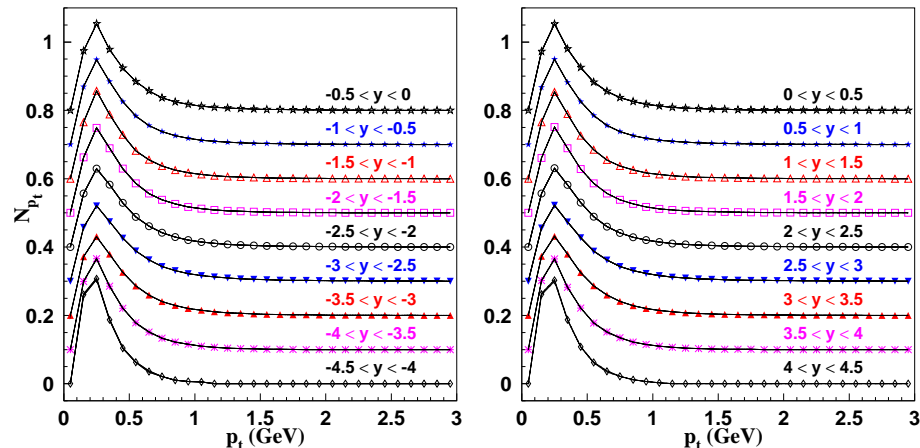


Figure 7.1: Distribution of p_t for various intervals in y . For clarity, the points for successive y intervals are displaced on the vertical axis by a successive addition of 0.1 to the measured values of the transverse momentum spectra.

where N_y and N_{p_t} are the single-particle inclusive rapidity and p_t distributions, respectively. The factorization of transverse and longitudinal distributions has been checked for the analyzed L3 two-jet data. The distribution of p_t is, to a good approximation, independent of the rapidity. This is shown in Fig. 7.1 and confirms the applicability of the factorization assumption Eq. (7.2).

With these assumptions and using $H(\tau)$ given in Fig. 7.2 as obtained from the fit of Eq. (6.26) together with the inclusive rapidity and p_t distributions (shown in Fig. 7.3a and b, respectively), the full emission function is reconstructed. (To account for detector acceptance and resolution, the raw data is corrected by the ratio of the corresponding MC distribution before and after the detector simulation.) Its integral over the transverse distribution is plotted in Fig. 7.4. It exhibits a “boomerang” shape with a maximum at low t and z but with tails reaching out to very large values of t and z , a feature already observed for hadron-hadron [90,91] and heavy ion collisions [92].

The transverse part of the emission function at given proper-time, τ , is obtained by integrating over z and azimuthal angle. Figs. 7.5 and 7.6 show the transverse part of the emission function for various proper times. Particle production starts immediately, increases rapidly and decreases slowly. In the transverse direction, a ring-like structure is observed similar to the expanding, ring-like wave created by a pebble in a pond. This ring like structure was also observed in hadron-hadron collisions [90], where it was interpreted as due to the production of a fire-ring.

Interpolating and extrapolating Figs. 7.5 and 7.6, the proper-time dependence of the transverse expansion of the emission function can be best shown in a movie [93] that ends in about 3.5 fm, making it the shortest movie ever made of a process in nature.

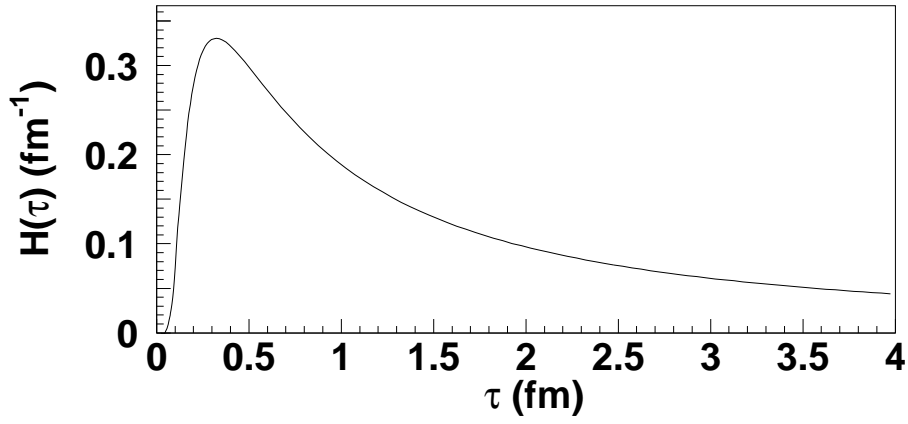


Figure 7.2: The proper-time distribution $H(\tau)$ with $\alpha = 0.43$, $\Delta\tau = 1.8$ fm and $\tau_0 = 0$ fm, corresponding to fits of Eq. (6.26) to two-jet data for various \overline{m}_t intervals.

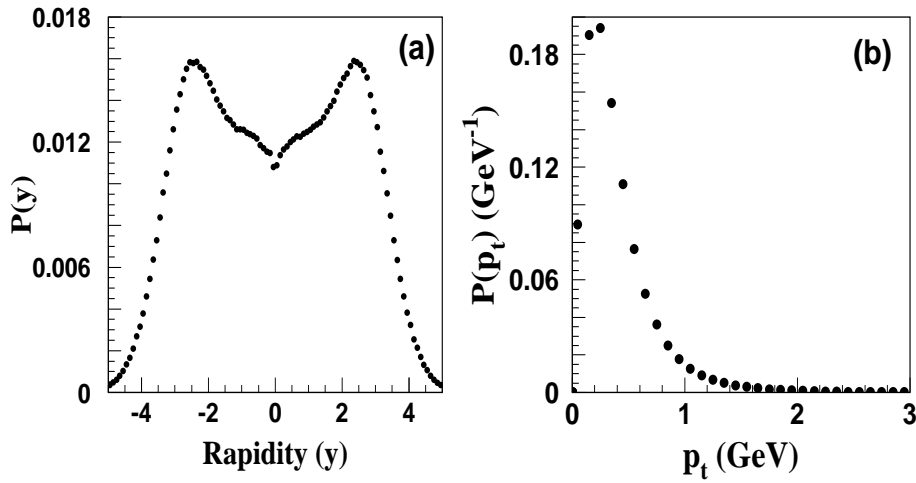


Figure 7.3: Normalized distributions of (a) rapidity and (b) transverse momentum.

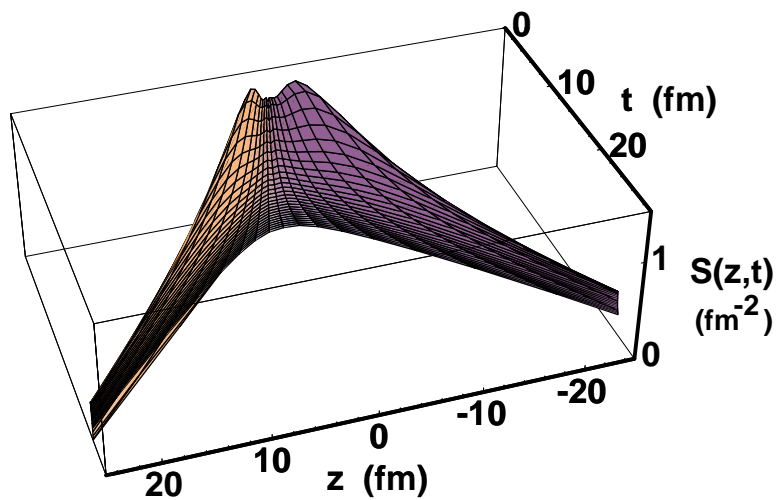
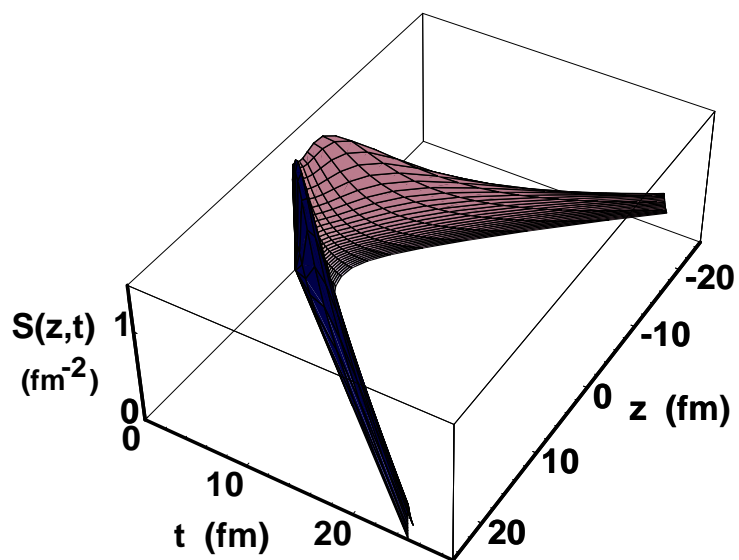


Figure 7.4: Two views of the temporal-longitudinal part of the emission function normalized to the average number of pions per event.

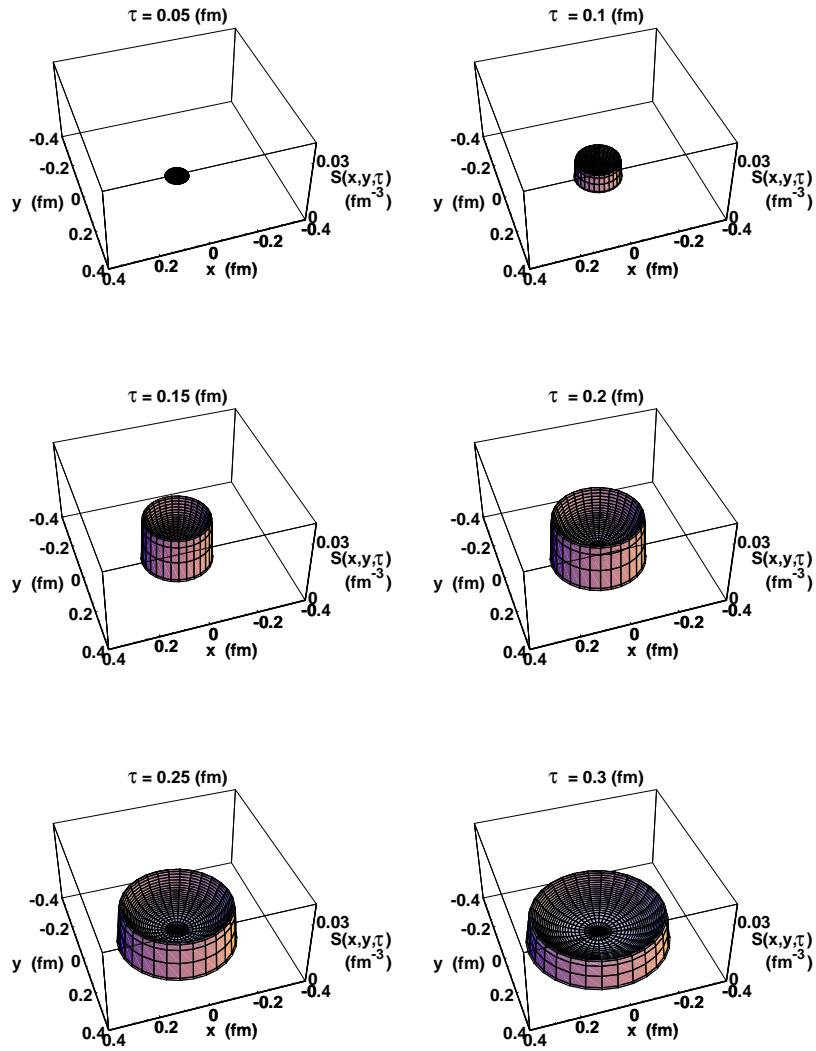


Figure 7.5: The transverse emission function normalized to the average number of pions per event for various proper times. An animated gif file covering the first $0.3 \text{ fm} = 10^{-24} \text{ sec}$ is available [93].

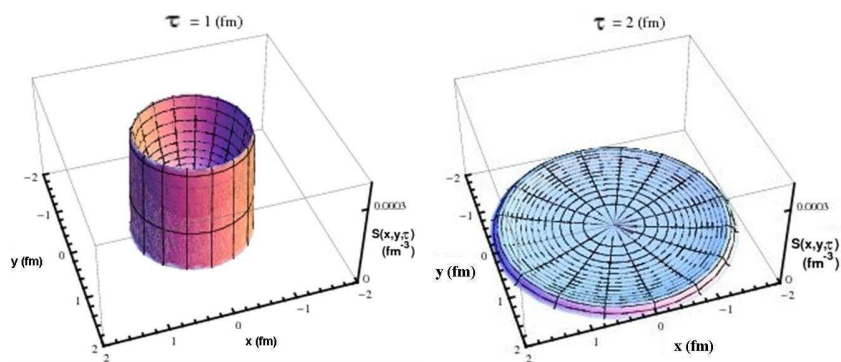


Figure 7.6: The transverse emission function normalized to the average number of pions per event for $\tau = 1 \text{ fm}$ and $\tau = 2 \text{ fm}$.

Chapter 8

BEC and the Anomalous Dimension of QCD

8.1 Introduction

In this chapter, the Bose-Einstein correlation function is shown to be related to the fractal structure of QCD jets. The anomalous dimension of QCD determines the Lévy index of stability. Thus the running coupling constant of QCD becomes measurable with the help of two-particle Bose-Einstein correlation functions.

The study of fractal phenomena was introduced to high energy particle and nuclear physics by Białas and Peschanski in ref. [94]; see also ref. [95] for an early review. In QCD, partons emit partons that emit additional partons and so on. The fractal structure of these successive emissions was explored with the help of a geometric picture in refs. [96–98]. These ideas were developed further by the Lund group [99–101], by Dokshitzer and Dremin [102] as well as by Ochs and Wosiek [103,104] and Brax, Meunier and Peschanski [105]. Both theoretical and experimental aspects of the so-called intermittency or fractal structures in high energy physics were reviewed by De Wolf, Dremin and Kittel in ref. [106,107].

Białas realized, that Bose-Einstein correlations and intermittency might be deeply connected [108]. The mathematical properties of Bose-Einstein correlation functions for Lévy stable (convolution invariant) sources were written up in refs. [37]. Here we add a physical interpretation and show, that the fractal properties of QCD cascades can naturally be measured by the Lévy index of stability of Bose-Einstein correlations. Our analytical results are similar in spirit to the numerical investigations of Wilk and collaborators in ref. [109].

8.2 (Multi)fractal Structure of the QCD Jets

The process of e^+e^- annihilation into hadrons, is often described in terms of two stages, a hard perturbative, calculable process, described in terms of quarks and gluons, and a soft hadronization process in which the energy of these partons is transformed into the observable hadrons. The latter phase can be described phenomenologically in terms of clusters or in terms of strings as in the Lund model.

The hard perturbative phase can be described using the dipole formulation of QCD cascades together with an infrared stable measure on parton states related to the hadronic multiplicity.

8.2.1 Dipole Formulation

A high energy $q\bar{q}$ system radiates gluons according to the dipole formula [96,97]

$$dn = \frac{3\alpha_s}{4\pi^2} \frac{dk_{\perp}^2}{k_{\perp}^2} dy d\phi, \quad (8.1)$$

where α_s is the running coupling constant of QCD, k_{\perp} is the transverse momentum, y is the rapidity of the radiated gluon and ϕ is the angle between the quark and the radiated gluon.

Here the phase space for the emission of a gluon is given by the relation

$$|y| \leq \frac{1}{2} \ln(s/k_{\perp}^2), \quad (8.2)$$

which corresponds to the triangular region in a $(y, \ln k_{\perp}^2)$ diagram as shown in Fig. 8.1.a. Therefore the rapidity range Δy_1 for the emission of the first gluon is given by $\Delta y_1 = \ln s - \ln k_{\perp,1}^2$.

If two gluons are emitted, then the distribution of the hardest gluon is described by Eq. (8.1), while the emission of the second, softer, gluon corresponds to emission from two dipoles. The first consists of the quark and the first gluon, and the second the first gluon and the anti-quark.

Denoting the masses of the qg_1 and $g_1\bar{q}$ systems by $\sqrt{s_{12}}$ and $\sqrt{s_{23}}$, respectively, the transverse momentum, $k_{\perp,1}$, and rapidity, y_1 , of the first gluon are given by the relations

$$s \cdot k_{\perp,1}^2 = s_{12} \cdot s_{23}, \quad (8.3)$$

$$y_1 = \frac{1}{2} \ln \frac{s_{23}}{s_{12}}. \quad (8.4)$$

Therefore the rapidity range Δy_2 available for the second gluon is given by

$$\begin{aligned} \Delta y_2 &= \ln(s_{12}/k_{\perp,2}^2) + \ln(s_{23}/k_{\perp,2}^2) = \\ &= \ln s + \ln k_{\perp,1}^2 - 2 \ln k_{\perp,2}^2 = \\ &= \Delta y_1 + 2(\ln k_{\perp,1}^2 - \ln k_{\perp,2}^2). \end{aligned} \quad (8.5)$$

The phase space available for emission of a second gluon is increased as compared to that of the first gluon. It corresponds to the folded surface in Fig. 8.1.b, with the constraint $k_{\perp,2}^2 < k_{\perp,1}^2$, as the first gluon is assumed to be the hardest one.

This procedure can be generalized so that the emission of a third, still softer gluon corresponds to radiation from three color dipoles. With n gluons emitted already, the emission of the $(n+1)$ -th gluon is given by a chain of $n+1$ dipoles. We note that the dipoles connect the gluons in the same way as the string in the Lund fragmentation model.

Thus, with many gluons, the gluonic phase space can be represented by a multi-faceted surface as illustrated in Fig. 8.1.c. Each gluon adds a fold to the surface, which increases the phase space for softer gluons. (Note, that in this process the recoils are neglected, as is the case in the leading log approximation).

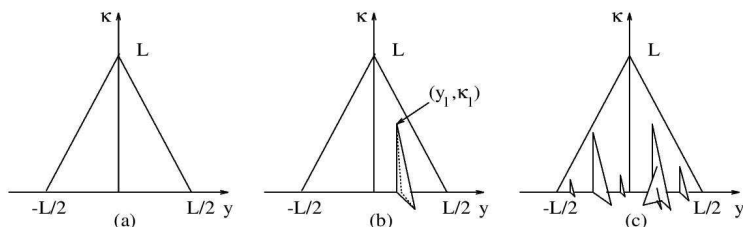


Figure 8.1: The phase space of QCD jets in the (y, κ) plane, where $\kappa = \log(k_{\perp}^2)$. (a) The phase-space available for a gluon emitted by a high energy $q\bar{q}$ system is a triangular region in the (y, κ) plane. (b) If one gluon is emitted at (y_1, κ_1) , the phase-space for a second (softer) gluon is given by the area of this folded surface. (c) The total gluonic phase space can be described by this multifaceted fractal surface [96–98].

8.2.2 Multiplicity Measure

In string fragmentation the hadronic multiplicity for a simple $q\bar{q}$ -system is proportional to $\ln s$. The hadrons are evenly distributed in rapidity, which means that their energy-momentum four-vectors are distributed around a hyperbola.

For a $q\bar{q}g$ -system, we obtain in the Lund string fragmentation model a bent string with two straight segments. The energy in the segments is s_{12} and s_{23} , where $s_{ij} = (k_i + k_j)^2$ and k_1, k_2 and k_3 are the four-momenta of the q, g and \bar{q} respectively. Thus the average multiplicity, $\langle n \rangle$, is given by the relation

$$\langle n \rangle \propto \ln s_{12} + \ln s_{23} = \ln s + \ln k_{\perp}^2. \quad (8.6)$$

Here k_{\perp}^2 is the transverse momentum of the gluon. We also note that this expression is equal to the length of the baseline of the surface in Fig. 8.1.b. In

this case, the energy-momentum four-vectors of hadrons are distributed around two hyperbolae.

For a multigluon state we find in the same way

$$\langle n \rangle \propto \Sigma \ln s_{i,i+1} \approx \ln s + \Sigma \ln k_{\perp,i}^2. \quad (8.7)$$

This expression is an “effective rapidity range”. It is given by the length of the baseline of the surface in Fig. 8.1 c.

8.2.3 Fractal Structures

For a multigluon state the hadron momenta are distributed around a curve in energy-momentum space (called the x-curve). Due to its iterative nature, the process generates a Koch-type fractal curve at the base-line. The length of this base-line of the partonic structure on Fig. 8.1.c is proportional to the particle multiplicity. This curve is longer, when studied with higher resolution: it is a fractal curve, embedded into the four-dimensional energy-momentum space, characterized by the fractal dimension

$$d_f = 1 + \sqrt{\frac{6\alpha_s}{\pi}}, \quad (8.8)$$

or one plus the anomalous dimension of QCD [96–98].

With the help of the Lund string fragmentation picture, this fractal in momentum space is mapped into a fractal in coordinate space, and the constant of conversion is the hadronic string tension, $\kappa \approx 1$ GeV/fm. This mapping does not change the fractal properties of the curve. The emission of softer and softer gluons corresponds to a smaller and smaller modification of this curve, as a gluon with a very small transverse mass creates a very small kink on the Lund string. Hence this curve is infrared stable.

8.3 The Anomalous Dimension of QCD Jets and BEC

Let us discuss here the stability of the particle emitting source in QCD, and consider the Bose-Einstein correlation functions for such sources.

We focus on the property of particle emission from QCD jets, that the fractal defining the particle emission is infrared stable: adding one more, very soft gluon does not change the resulting source distributions. Thus the source of particles is stable under convolution. The Bose-Einstein correlation functions for such particle emitting sources were evaluated recently in ref. [37].

For the case of the partons emitting partons emitting partons and so on, the final position of a particle emission is given by a large number of position shifts,

hence the distribution of the final position x is obtained as a convolution,

$$x = \sum_{i=1}^n x_i, \quad f(x) = \int \prod_{i=1}^n dx_i \prod_{j=1}^n f_j(x_j) \delta(x - \sum_{k=1}^n x_k). \quad (8.9)$$

The Generalized Central Limit Theorem states that under certain conditions, the distribution of the sum of a large number of random variables converges (for $n \rightarrow \infty$) to a limit distribution. The stable distributions are frequently given in terms of their characteristic functions (= Fourier transforms), as the Fourier transform of a convolution is a product of the Fourier-transforms,

$$\tilde{f}(q) = \prod_{i=1}^n \tilde{f}_i(q), \quad (8.10)$$

and limit distributions appear when the convolution of one more elementary process does not change the form of the limit distribution but only results in a modification of its location and scale parameters. Note that Eq. (8.10) holds for all stable distributions including asymmetric ones. However, it is easier to demonstrate the validity of this assumption for univariate, symmetric stable distributions. The characteristic function of univariate and symmetric stable distributions is

$$\tilde{f}(q) = \exp(iq\delta - |\gamma q|^\alpha), \quad (8.11)$$

where the support of the density function $f(x)$ is $(-\infty, \infty)$.

These Lévy distributions are indeed stable under convolutions, in the following sense:

$$\tilde{f}_i(q) = \exp(iq\delta_i - |\gamma_i q|^\alpha), \quad \prod_{i=1}^n \tilde{f}_i(q) = \exp(iq\delta - |\gamma q|^\alpha), \quad (8.12)$$

$$\gamma^\alpha = \sum_{i=1}^n \gamma_i^\alpha, \quad \delta = \sum_{i=1}^n \delta_i. \quad (8.13)$$

Figure 8.2 (top) shows univariate symmetric Lévy source distributions. Note that values of the index of stability α are related to the tails of these distributions. If $\alpha < 2$, for large values of $S = r/R$ the Lévy sources decay as $f_\alpha(S) \propto S^{-1-\alpha}$. Bose-Einstein correlation functions for Lévy stable source distributions are shown in Figure 8.2 (bottom) for various values of the index of stability α , and for a constant value of the radius parameter R . These Bose-Einstein correlation functions are sensitive to the value of α not only in the small $Q < \hbar/R$ region, but are also in the “large” relative momentum region of $Q > \hbar/R$. Thus these correlations are sensitive to the structure of the particle emission in the region which is shaped by the jets.

A random walk, where the length of the steps is given by a Lévy distribution, and the direction of the steps is random, corresponds to a fractal curve, in physical terms it can be interpreted as the path of a test particle performing a

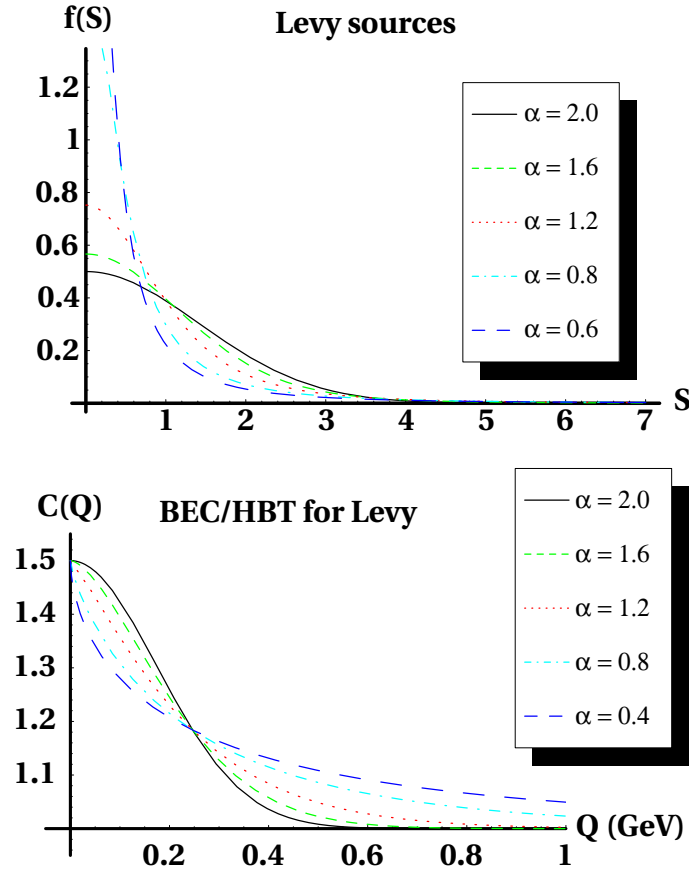


Figure 8.2: (top) Source functions for univariate symmetric Lévy laws, as a function of the dimensionless variable $S = r/R$, on a linear-linear scale, for various values of the Lévy index of stability, α . (bottom) Bose-Einstein correlation (or HBT) correlation functions for univariate symmetric Lévy laws, for a fixed scale parameter of $R = 0.8$ fm and various values of the Lévy index of stability, α .

generalized Brownian motion. This motion is referred to as anomalous diffusion and the probability that the test particle diffuses to distances r greater than a certain value of $|S|$ is given by $P(r > |S|) \propto |S|^{-\alpha}$. This relation is valid for anomalous diffusion not only in one, but also in two and three dimensions. Thus the Lévy index of stability α is the fractal dimension of the trajectory of the corresponding anomalous diffusion [110].

Note that, if gluon radiation is neglected, the $q\bar{q}$ system hadronizes as a 1+1 dimensional hadronic string, which has no fractal structure. If the gluon emission is switched on, the emission of gluon n from one of the n dipoles corresponds to a step of an anomalous diffusion in the plane transverse to the given dipole. Hence the anomalous dimension of QCD is equal to the Lévy index

of stability of this anomalous diffusion,

$$\sqrt{\frac{3\alpha_s}{2\pi}} = \alpha. \quad (8.14)$$

Thus we find the following relationship between the strong coupling constant and the exponent of an invariant relative momentum dependent Bose-Einstein correlation function:

$$\alpha_s = \frac{2\pi}{3}\alpha^2. \quad (8.15)$$

Assuming generalized local parton hadron duality [111–113], one can expect that the distribution of hadrons retains the features of the gluon distribution. For the value $\alpha = 0.43 \pm 0.03$ found in Sect. 6.2.5, we find $\alpha_s = 0.39 \pm 0.05$ for two-jet events. This is a reasonable value for a scale of 1–2 GeV, where particle production takes place. For comparison, from τ decay, $\alpha_s(m_\tau \approx 1.8 \text{ GeV}) = 0.34 \pm 0.03$ [114].

Chapter 9

Conclusions

A detailed study of the Bose-Einstein correlation functions of identical charged pions produced in Z-boson decays has been performed in terms of various parametrizations. The correlation function is found to depend, to a good degree of approximation, only on the absolute value of the four-momentum difference, Q , of the two pions. This is in sharp contrast to the BEC found in hadron-hadron and heavy-ion collisions, where the correlation function does not depend simply on Q , but on its components separately.

The so-called τ -model is able to explain the Q -dependence. The τ -model assumes:

- The average space-time position at which particles are produced is linearly related to their four-momentum by

$$\bar{x}^\mu(p^\mu) = a\tau p^\mu . \quad (9.1)$$

- The distribution of x^μ about its average is much narrower than the proper-time distribution.

To arrive at a formula for R_2 an additional assumption is made, namely that this correlation, i.e., the value of a , is approximately the same for the two pions. The resulting formula is in terms of the distribution of the proper-time of emission of pions, for which we assume a one-sided Lévy distribution.

The resulting parametrization of R_2 was simplified by assuming that particle production starts immediately after the collision and by introducing additional parameters R and R_a to characterize the dependence on the position momentum correlation parameter a . The simplified formula is able to describe the *transverse-mass averaged* three-jet as well as two-jet data even though the data do not satisfy the assumption of $a_1 \approx a_2$. However, only the two-jet event sample was investigated further using the unsimplified τ -model formula, Eq. (6.26),

since a is known exactly for this type of reaction: $a = 1/m_t$. The data are well-described by this formula.

A Lévy distribution arises naturally from a fractal or from anomalous diffusion, and the parton shower of the leading log approximation of QCD is a fractal. In this case, the Lévy index of stability is related to the strong coupling constant, α_s . For the value of the Lévy parameter α found in fits of the τ -model equation, we obtain a strong coupling constant of $\alpha_s = 0.39 \pm 0.05$, a reasonable value for a scale of 1 – 2 GeV where particle production takes place. For comparison, from τ decay, $\alpha_s(m_\tau \approx 1.8 \text{ GeV}) = 0.34 \pm 0.03$. This agreement provides additional support for the τ -model.

The pion emission function of two-jet events is reconstructed from the results of the fit of Eq. (6.26) to the two-jet data assuming that the pion emission function can be factorized as the product of a single-particle transverse distribution, the space-time rapidity distribution and the proper-time distribution. In the τ -model the transverse and space-time rapidity distributions are related to the transverse momentum and rapidity distributions. The proper-time distribution is found from BEC. Particle production begins immediately after the collision, increases rapidly, then decreases slowly, occurring predominantly close to the light cone. In the transverse plane a ring-like structure expands outwards, which is similar to a wave created by a pebble in a pond. The observed ring-like structure is somewhat similar to a *ring of fire* as seen in hadron-hadron collisions. However, in e^+e^- collisions, the measured correlation function does not depend on the various relative momentum components separately, as it should for fireball or fire-ring type of sources, as clearly demonstrated by the mere Q dependence of the correlation function. Hence, these L3 Bose-Einstein correlation data are inconsistent with thermalized production of hadrons in two-jet events in e^+e^- annihilation at LEP.

The success of the τ -model in describing BEC and in particular the observation of the predicted m_t dependence of the width of the $R_2(Q, m_t)$ correlation functions is evidence for the model's assumption of a strong correlation between momentum and configuration space. Other evidence for such a correlation was recently provided by an OPAL study of the transverse-momentum dependence of BEC radii in the Bertsch-Pratt and Yano-Koonin parametrizations [82].

Appendix: Lévy Stable Distributions

A normal distribution in a variate ξ with mean μ and variance σ^2 is a statistic distribution with cumulative probability function

$$P(\xi < x) = \frac{1}{\sqrt{2\pi}\sigma} \int_{-\infty}^x \exp\left(-\frac{(t-\mu)^2}{2\sigma^2}\right) dt \quad (\text{A.1})$$

on the domain $x \in (-\infty, +\infty)$. While statisticians and mathematicians uniformly use the term ‘normal distribution’ for this distribution physicists frequently call it a Gaussian distribution. A Gaussian distribution with mean $\mu = 0$ and variance $\sigma^2 = 1$ is called the standard normal distribution.

The Central Limit Theorem states the following: let ξ_1, ξ_2, \dots be independent random variables with their sum $S_n = \xi_1 + \xi_2 + \dots + \xi_n$. Assume that σ_i^2 is the variance of ξ_i and μ_i is the mean of ξ_i , and assume that $0 < \sigma_i^2 < \infty$, $-\infty \leq \mu_i \leq \infty$. Then

$$\lim_{n \rightarrow \infty} P\left(\frac{S_n - \sum \mu_i}{\sqrt{\sum \sigma_i^2}} < x\right) = \frac{1}{\sqrt{2\pi}} \int_{-\infty}^x \exp\left(-\frac{t^2}{2}\right) dt \quad \forall x \in \mathbb{R}. \quad (\text{A.2})$$

Informally speaking, the distribution of normalized S_n converges to the standard normal distribution.

An important property of Gaussian random variables is that the sum of two of them is itself a normal random variable. One consequence of this is that if ξ is Gaussian, then for ξ_1 and ξ_2 independent copies of ξ and any positive constant a and b ,

$$a\xi_1 + b\xi_2 \doteq c\xi + d, \quad (\text{A.3})$$

for some positive c and some $d \in \mathbb{R}$. (The symbol \doteq means equality in distribution.) We say that a random variable is stable if it satisfies Eq. (A.3). The word stable is used because the shape is preserved (unchanged) under addition.

There are multiple parametrizations for stable laws because of a combination of historical evolution or different situations which required different

parametrizations. In the notation of Nolan [81], our choice corresponds to the $S(\alpha, \beta, \gamma, \delta; 1)$ convention.

A random variable is $S(\alpha, \beta, \gamma, \delta; 1)$ if its characteristic function is

$$\tilde{f}(u) = \exp\left(-\gamma^\alpha |u|^\alpha \left[1 - i\beta \left(\tan \frac{\pi\alpha}{2}\right) (\text{sign } u)\right] + i\delta u\right) \quad \alpha \neq 1. \quad (\text{A.4})$$

For the case of $\alpha = 1$ see [81].

A Lévy stable distribution is specified by four parameters: scale γ , exponent α (the index of stability), location δ and skewness parameter β . The parameters are restricted to the range $\gamma \geq 0$, $\alpha \in (0, 2]$, $\delta \in \mathbb{R}$ and $\beta \in [-1, 1]$. Since α and β determine the form of the distribution, they may be considered shape parameters. Note that the Gaussian is obtained in case of $\alpha = 2, \beta = 0, \gamma = \sigma$ and $\delta = \mu$.

In our work, we use the following convention: $\gamma^\alpha = \frac{1}{2}R^\alpha$ and $\delta = x_0$.

Lévy stable distributions are symmetric around zero when $\beta = 0$ and $x_0 = 0$, in which case the characteristic function has the simpler form

$$\tilde{f}(u) = e^{-R^\alpha |u|^\alpha}. \quad (\text{A.5})$$

(Note that when $\beta \neq 0$ the asymmetry factor (the imaginary term) becomes an issue.)

Stable densities are supported on either the whole real line or a half line. The latter situation can only occur when $\alpha < 1$ and ($\beta = +1$ or $\beta = -1$). Precise limits are given by the following expression.

$$\text{support } f(x) = \begin{cases} [x_0, \infty) & \alpha < 1 \text{ and } \beta = 1, \\ (-\infty, x_0] & \alpha < 1 \text{ and } \beta = -1, \\ (-\infty, \infty) & \text{otherwise.} \end{cases} \quad (\text{A.6})$$

A general distribution is said to be heavy tailed if its tails are heavier than exponential. For $\alpha < 2$, stable distributions have one tail (when $\alpha < 1$ and $\beta = \pm 1$) or both tails (all other cases) that are asymptotically power laws with heavy tails. One consequence of heavy tails is that not all moments exist. In most statistical problems, the first moment and variance are routinely used to describe a distribution. However, these are not generally useful for heavy tailed distributions, because the integral expressions for these expectations may diverge.

The classical Central Limit Theorem says that the normalized sum of independent, identical terms with finite variance converges to a normal distribution. The Generalized Central Limit Theorem shows that if the finite mean and finite variance assumptions are dropped, the only possible resulting limits are stable.

Bibliography

- [1] UA1 Collab., G. Arnison et al., Phys. Lett. **B122** (1983) 103.
- [2] UA2 Collab., M. Banner et al., Phys. Lett. **B122** (1983) 476.
- [3] UA1 Collab., G. Arnison et al., Phys. Lett. **B126** (1983) 398.
- [4] UA2 Collab., P. Bagnaia et al., Phys. Lett. **B129** (1983) 130.
- [5] ALEPH, DELPHI, L3 and OPAL Collaborations and the LEP Electroweak Working Group, J. Alcaraz et al., [arXiv:hep-ph/0612034](https://arxiv.org/abs/hep-ph/0612034), 2006.
- [6] A.H. Mueller, Nucl. Phys. **B 213** (1983) 85.
- [7] Yu.L. Dokshitzer et al., Rev. Mod. Phys. **60** (1988) 373.
- [8] G. Marchesini, B.R. Webber, Nucl. Phys. **B 238** (1984) 1.
- [9] K. Konishi, A. Ukawa, G. Veneziano, Nucl. Phys. **B 157** (1979) 45.
- [10] R. Odorico, Nucl. Phys. **B 172** (1980) 157.
- [11] G.C. Fox, S. Wolfram, Nucl. Phys. **B 168** (1980) 285.
- [12] J. Kalinowski, K. Konishi, T.R. Taylor, Nucl. Phys. **B 181** (1981) 221.
- [13] J.F. Gunion, J. Kalinowski, Phys. Rev. **D 29** (1984) 1545.
- [14] J.F. Gunion, J. Kalinowski, L. Szymanowski, Phys. Rev. **D 32** (1985) 2303.
- [15] B. Andersson, G. Gustafson, G. Ingelman and T. Sjöstrand, Phys. Rep. **B101** (1983) 31.
- [16] T. Sjöstrand, Comp. Phys. Comm. **82** (1994) 74.
- [17] G. Marchesini et al., Comp. Phys. Comm. **67** (1992) 465.
- [18] B. Andersson and M. Rignér, Nucl. Phys. **B513** (1998) 627.
- [19] R.D. Field and R.P. Feynman, Nucl. Phys. **B136** (1978) 1.
- [20] D. Amati and G. Veneziano, Phys. Lett. **B83** (1979) 87.

- [21] G. Marchesini, L. Trentadue and G. Veneziano, Nucl. Phys. **B181** (1981) 335.
- [22] S. Brandt et al., Phys. Lett. **12** (1964) 57.
- [23] MARK J Collab., D.P. Barber et al., Phys. Rev. Lett. **43** (1979) 830.
- [24] R.J. Glauber, Phys. Rev. Lett. **10** (1963) 84.
- [25] http://nobelprize.org/nobel_prizes/physics/laureates/2005/info.pdf.
- [26] R. Hanbury Brown and R.Q. Twiss, Phil. Mag. **45** (1954) 663.
- [27] R. Hanbury Brown and R.Q. Twiss, Nature **177** (1956) 27.
- [28] R. Hanbury Brown and R.Q. Twiss, Nature **178** (1956) 1046.
- [29] G. Goldhaber, S. Goldhaber, W.B. Fowler and T.F Hoang, Phys. Rev. Lett. **3** (1959) 181.
- [30] G. Goldhaber, S. Goldhaber, W. Lee and A. Pais, Phys. Rev. **120** (1960) 300.
- [31] T. Csörgő, Heavy Ion Physics **15** (2002) 1.
- [32] W. Kittel, Acta Phys. Pol. **B32** (2001) 3927.
- [33] W. Kittel, [arXiv:hep-ph/0111462](https://arxiv.org/abs/hep-ph/0111462), 2001.
- [34] W. Kittel, [arXiv:hep-ph/9905394](https://arxiv.org/abs/hep-ph/9905394), 1999.
- [35] G. Alexander, Rep. Prog. Phys. **66** (2003) 481.
- [36] T. Csörgő, S. Hegyi and Z.A. Zajc, Phys. Lett. **B489** (2000) 15.
- [37] T. Csörgő, S. Hegyi and W.A. Zajc, Eur. Phys. J. **C36** (2004) 67.
- [38] T. Csörgő, S. Hegyi, T. Novák and W.A. Zajc, Acta Phys. Pol. **B 36** (2005) 329.
- [39] LEP design report volume I, Internal Report CERN-LEP/TH/83-29, 1983.
- [40] LEP design report volume II, Internal Report CERN-LEP/TH/84-01, 1984.
- [41] LEP design report volume III, Internal Report CERN-LEP/TH/96-01, 1996.
- [42] L3 Collab., B. Adeva et al., Nucl. Inst. Meth. **A289** (1990) 35.
- [43] L3 Collab., O. Adriani et al., Nucl. Inst. Meth. **A344** (1994) 521.
- [44] R. Brun et al., CERN/DD/EE/84-1, (1987).

- [45] L. Lönnblad and T. Sjöstrand, *Eur. Phys. J.* **C2** (1998) 165.
- [46] T. Sjöstrand, *Comp. Phys. Comm.* **132** (2001) 238.
- [47] G. Corcella, *JHEP* **01** (2001) 10.
- [48] L3 Collab., P. Achard et al., *Phys. Rep.* **399** (2004) 71.
- [49] JADE Collab., W. Bartel et al., *Z. Phys.* **C 33** (1986) 23.
- [50] S. Catani et al., *Phys. Lett.* **B 269** (1991) 432.
- [51] S. Moretti, L. Lönnblad and T. Sjöstrand, *JHEP* **9808** (1998) 001.
- [52] A. Ballestro et al., [arXiv:hep-ph/0006259](https://arxiv.org/abs/hep-ph/0006259), 2000.
- [53] G.I. Kopylov and M.I. Podgoretsky, *Sov. J. Nucl. Phys.* **15** (1973) 219.
- [54] G.I. Kopylov, *Phys. Lett.* **B 50** (1974) 472.
- [55] S. Pratt, *Phys. Lett.* **B301** (1993) 159.
- [56] T. Csörgő and J. Zimányi, *Phys. Rev. Lett.* **80** (1998) 916.
- [57] M. Deutschmann et al., *Nucl. Phys.* **B 204** (1982) 333.
- [58] T. Csörgő, B. Lörstad and J. Zimányi, *Z. Phys.* **C71** (1996) 491.
- [59] E.P. Wigner, *Phys. Rev.* **40** (1932) 749.
- [60] H. Gyulassy, S. Kauffmann, L.W. Wilson, *Phys. Rev.* **C20** (1979) 2267.
- [61] S. Pratt, T. Csörgő and J. Zimányi, *Phys. Rev.* **C 42** (1990) 2646.
- [62] D.H. Boal, C.K. Gelbke and B.K. Jennings, *Rev. Mod. Phys.* **62** (1990) 553.
- [63] L3 Collab., M. Acciarri et al., *Phys. Lett.* **B458** (1999) 517.
- [64] OPAL Collab., G. Abbiendi et al., *Eur. Phys. J.* **C16** (2000) 423.
- [65] DELPHI Collab., P. Abreu et al., *Phys. Lett.* **B471** (2000) 460.
- [66] ALEPH Collab., A. Heister et al., *Eur. Phys. J.* **C36** (2004) 147.
- [67] TASSO Collab., M. Althoff et al., *Z. Phys.* **C30** (1986) 355.
- [68] T. Csörgő and B. Lörstad, *Phys. Rev.* **C54** (1996) 1390.
- [69] NA22 Collab., N.M. Agababyan et al., *Z. Phys.* **C71** (1996) 405.
- [70] A.N. Makhlin and Yu.M. Sinyukov, *Z. Phys.* **C39** (1988) 69.
- [71] T. Csörgő and S. Pratt, in *Proc. Workshop on Relativistic Heavy-Ion Physics*, Budapest, Hungary, May 17-21, 1991, ed. T. Csörgő et al., (KFKI-1991-28/A, Budapest, 1991), p. 75.

- [72] G.F. Bertsch, Nucl. Phys. **A498** (1989) 173c.
- [73] S. Pratt, Phys. Rev. Lett. **53** (1984) 1219.
- [74] M.G. Bowler, Z. Phys. **C29** (1985) 617.
- [75] X. Artru and A. Mennessier, Nucl. Phys. **B70** (1974) 93.
- [76] X. Artru, Z. Phys. **C26** (1984) 83.
- [77] F.Y. Edgeworth, Trans. Cambridge Phil. Soc. **20** (1905) 36.
- [78] Harald Cramér, Mathematical Methods of Statistics, (Princeton Univ. Press, 1946).
- [79] W. Feller, An Introduction to Probability Theory and its Applications, (World Scientific, 1971).
- [80] V.V. Uchaikin and V.M. Zolotarev, Chance and stability, stable distributions and their applications, (VSP Science, 1999).
- [81] J.P. Nolan, Stable distributions: Models for Heavy Tailed Data, 2005, <http://academic2.american.edu/~jpnolan/stable/CHAP1.PDF>.
- [82] OPAL Collab., G. Abbiendi et al., Eur. Phys. J. **C 52** (2007) 787.
- [83] T. Csörgő and J. Zimányi, Nucl. Phys. **A517** (1990) 588.
- [84] F.B. Yano and S.E. Koonin, Phys. Lett. **B78** (1978) 556.
- [85] B. Lörstad and O.G. Smirnova, in Proc. 7th Int. Workshop on Multiparticle Production, Nijmegen, The Netherlands, June 30 - July 6 1996, ed. R.C. Hwa et al., (World Scientific, Singapore, 1997), p. 42.
- [86] J.A. van Dalen, in Proc. 8th Int. Workshop on Multiparticle Production, Mátraháza, Hungary, 14-21 June 1998, ed. T. Csörgő et al., (World Scientific, Singapore, 1999), p. 37.
- [87] T. Csörgő, in Proc. XXXII. ISMD'02, Alushta, Ukraine, Sep 7-13, 2002, ed. A. Sissakian et al., (World Scientific, Singapore, 2003), p. 38.
- [88] W.J. Metzger, T. Novák, W. Kittel and T. Csörgő, Int. J. Mod. Phys. **E16** (2008) 3224.
- [89] T. Csörgő, W. Kittel, W.J. Metzger and T. Novák, Phys. Lett. **B663** (2008) 214.
- [90] NA22 Collab., N.M. Agababyan et al., Phys. Lett. **B422** (1998) 359.
- [91] A. Ster and T. Csörgő, AIP Conf. Proc. **828** (2006) 572.
- [92] A. Ster, T. Csörgő and B. Lörstad, Nucl. Phys. **661** (1999) 419.
- [93] T. Novák, <http://www.hef.ru.nl/~novakt/movie/movie.gif>.

- [94] A. Białas and R. Peschanski, Nucl. Phys. **B273** (1986) 703.
- [95] A. Białas, Nucl. Phys. **A525** (1991) 345.
- [96] P. Dahlqvist, B. Andersson and G. Gustafson, Nucl. Phys. **A328** (1989) 76.
- [97] G. Gustafson and A. Nilsson, Nucl. Phys. **B355** (1991) 106.
- [98] G. Gustafson, in Proc Int. Workshop on Correlations and Multiparticle Production, Marburg, West Germany, May 14-16, 1990, ed. S. Raha M. Plümer and R. M. Weiner, (World Scientific, Singapore, 1991).
- [99] G. Gustafson and A. Nilsson, Z. Phys. **C52** (1991) 533.
- [100] G. Gustafson, Nucl. Phys. **B392** (1993) 251.
- [101] B. Andersson, G. Gustafson, J. Samuelsson, Nucl. Phys. **B 463** (1996) 217.
- [102] Y.L. Dokshitzer and I.M. Dremin, Nucl. Phys. **B402** (1993) 139.
- [103] W. Ochs and J. Wosiek, Phys. Lett. **B305** (1993) 144.
- [104] W. Ochs and J. Wosiek, Z. Phys. **C68** (1995) 269.
- [105] Ph. Brax, J.L. Meunier and R. Peschanski, Z. Phys. **C62** (1994) 649.
- [106] E.A. De Wolf, I.M. Dremin and W. Kittel, Phys. Rep. **270** (1996) 1.
- [107] W. Kittel and E.A. De Wolf, Soft Multihadron Dynamics, (World Scientific, 2005).
- [108] A. Białas, Acta Phys. Pol. **B 23** (1992) 561.
- [109] O.V. Utyuzh, G. Wilk and Z. Włodarczyk, Phys. Rev. **D61** (2000).
- [110] V. Seshardi, B.J. West, Proc. Nat. Acad. Sci. USA **79** (1982) 4501.
- [111] Ya.I. Azimov, Z. Phys. **C27** (1985) 65.
- [112] Ya.I. Azimov, Z. Phys. **C31** (1986) 213.
- [113] L. Van Hove and A. Giovannini, Acta Phys. Pol. **B19** (1988) 931.
- [114] Particle Data Group, W.-M. Yao et al., J. Phys. **G 33** (2006) 1.

Summary

*I told you, man: have fight, thrust
and be full of hope.*

/Imre Madách/

In this thesis, Bose-Einstein Correlations (BEC) of pairs of identical, charged pions produced in hadronic Z-boson decays are analyzed in terms of various parametrizations.

Essentially, intensity correlations appear due to the Bose-Einstein or Fermi-Dirac symmetrization of identical bosons or fermions, respectively, and due to the chaotic nature of particle emission. The Bose-Einstein effect in a system of identical bosons is a direct consequence of the symmetrization of the wave function of this system. This effect is experimentally measured as a relative enhancement of the production of identical bosons with small four-momentum differences, $Q = \sqrt{-(p_1 - p_2)^2}$, with respect to the production of these bosons that would occur in a world without BEC.

The main goal of this work was to reconstruct the complete space-time picture of the particle emitting source using information gained from the study of BEC. We investigated various static parametrizations of BEC in terms of Q and found that none give an adequate description of the Bose-Einstein correlation function observed experimentally. However, a good description was achieved within the framework of models assuming strongly correlated coordinate and momentum space. Using this description, the source function was reconstructed.

The final-state particles of Z decays were detected with the L3 detector, which was placed in the Large Electron Positron (LEP) Collider designed to accelerate and collide electrons and positrons at CERN, near Geneva. BEC were studied in the $e^+e^- \rightarrow Z \rightarrow q\bar{q}$ process at an e^+e^- center-of-mass energy of $\sqrt{s} \simeq 91.2$ GeV. Approximately 36 million like-sign pairs of well-measured charged particle tracks of about 0.8 million hadronic Z decays were used. We performed the analysis on the complete sample as well as on two- and three-jet sub-samples. The latter two samples were found using calorimeter clusters with the Durham jet algorithm with jet resolution parameter $y_{\text{cut}} = 0.006$. To determine the thrust axis of the event we also used calorimeter clusters.

Earlier investigations have shown that the source is not spherical but has an elongated shape along the thrust axis in the so-called longitudinal center-of-mass system. (In this system each pair of particles is Lorentz boosted, such that the sum of the two momenta in the direction of the thrust axis - that approximates the direction of the two initial quarks - is zero.) While elongation is well established, it has been found in this and other studies to be only about 20–30%. The fit results of Eq. (5.7) and (5.8) were interpreted as evidence that in e^+e^- collisions at $\sqrt{s} = m_Z$ the two-particle BEC depended on the relative momentum components only through the variable Q rather than on its components separately. This was further checked by explicit evaluation of the two-particle Bose-Einstein correlation function in the variables $Q_0, |\mathbf{Q}|$ for all events as well as for the two-jet events. Similarly to the earlier results by the TASSO Collaboration [67], we found that the BEC were maximal along the diagonal of $Q_0^2 = \mathbf{Q}^2$ in the whole experimentally observable range. This indicates that a simple Q dependence is a reasonably good approximation.

Fitting the correlation function as a function of Q , we found that the assumption that the source has a Gaussian shape was too simple. A possible deviation from the Gaussian shape can be phenomenologically measured with the help of the Edgeworth expansion. The fit result of this expansion confirmed that the shape of the source was not Gaussian. Hence we turned to stable distributions. One of the most important parameters of Lévy stable distributions is the index of stability α which must lie in the interval $(0, 2]$. The case $\alpha = 2$ corresponds to the Gaussian source distribution. The Edgeworth and the Lévy parametrizations did a fair job describing the region $Q < 0.6$ GeV for all events and three-jet events as well as for two-jet events, but failed at higher Q . In the region of $0.6 - 1.5$ GeV R_2 dips below the line of $\gamma(1 + \delta Q)$ of the long range correlations. The inability to describe this dip in R_2 was the primary reason for the failure of both the Edgeworth and symmetric Lévy parametrizations.

It was shown that the Q dependence of the correlation function could be understood if the four-momentum of a produced particle and the space-time position at which it was produced were linearly related and strongly correlated. A model which predicts Q -dependence while satisfying this linear relation is the so-called τ -model. As a by-product of explaining the Q dependence, this model also predicted a specific transverse mass dependence of R_2 . Within the framework of the τ -model the emission function depends on the proper-time distribution, $H(\tau)$. We choose a one-sided Lévy distribution as the proper-time distribution. We have performed this fit to the two-jet data in several m_t intervals and concluded that the main parameters were stable: the onset of the particle production was found to be $\tau_0 = 0 \pm 0.01$ fm, the index of stability $\alpha = 0.43 \pm 0.03$ and the width of the proper-time distribution $\Delta\tau = 1.8 \pm 0.4$ fm. Within errors, these values were found to be independent of m_t . This confirmed the expectation of the τ -model.

Within the framework of the τ -model, we reconstructed the space-time picture of the emitting process for two-jet events. To simplify the reconstruction we

assumed that the emission function could be factorized as the product of a single-particle transverse distribution, the proper-time distribution and the space-time rapidity distribution. Using the values of the parameters resulting from the fits, we reconstructed the emission function. From this we concluded that particle production started immediately after the collision, increased rapidly, and then decreased slowly. In the longitudinal direction (along the event axis) the emission function had a two-peak structure, with very long tails stretching along the light cone. In the transverse direction a ring-like structure was observed, similar to the expanding ring-like wave created by a pebble in a pond.

We found that BEC of all events as well as two- and three-jet events were described by a Lévy parametrization. A Lévy distribution arises naturally from a fractal, from a random walk or from anomalous diffusion, and the parton shower of the leading log approximation of QCD is a fractal. In this case, the Lévy index of stability α is related to the strong coupling constant, α_s , by $\alpha_s = \frac{2\pi}{3}\alpha^2$. Assuming generalized local parton hadron duality, one can expect that the distribution of hadrons retains the features of the gluon distribution. From the value of α obtained in our fits we found $\alpha_s = 0.39 \pm 0.05$ for two-jet events. This is a reasonable value for a scale of 1–2 GeV where particle production takes place. For comparison, from τ decay, $\alpha_s(m_\tau \approx 1.8 \text{ GeV}) = 0.34 \pm 0.03$.

Samenvatting

In dit proefschrift wordt Bose-Einstein Correlatie (BEC) van paren van identieke geladen pionen, geproduceerd in hadronische Z-boson verval, geanalyseerd in termen van verschillende parametrisaties.

Intensiteit correlaties ontstaan door Bose-Einstein of Fermi-Dirac symmetrisatie van identieke bosonen of fermionen, respectievelijk, en door de chaotische natuur van deeltjes emissie. Het Bose-Einstein effect in een systeem van identieke bosonen is een direct gevolg van de symmetrisatie van de golffunctie van dit systeem. Dit effect wordt experimenteel gemeten als een relatieve verhoging van de productie van identieke bosonen met klein vier-momentum verschil, $Q = \sqrt{-(p_1 - p_2)^2}$, ten opzichte van de productie in een wereld zonder BEC.

Het doel van dit proefschrift is om het complete ruimtetijd beeld te verkrijgen van de deeltjesbron door gebruik te maken van de informatie verkregen door de studie van BEC. We hebben verschillende statische parametrisaties van BEC onderzocht in termen van Q en hebben gevonden dat geen enkele een adequate omschrijving geeft van de experimenteel geconstateerde Bose-Einstein correlatie functie. Een goede beschrijving was echter verkregen binnen het raamwerk van modellen door een sterk gecorreleerde ruimte en tijd aan te nemen. Met gebruik van deze beschrijving is een bron functie gereconstrueerd.

The final-state deeltjes van het Z verval werden gedetecteerd met de L3 detector, die geplaatst was in de Large Electron Positron (LEP) Collider ontworpen om electronen en protonen te versnellen bij CERN, nabij Geneve. BEC werden bestudeerd in het $e^+e^- \rightarrow Z \rightarrow q\bar{q}$ proces in een e^+e^- massamiddelpuntsenergie van $\sqrt{s} \simeq 91.2$ GeV. Ongeveer 36 miljoen paar van goed gemeten banen van gelijk geladen deeltjes werden gebruikt van ongeveer 0.8 miljoen hadronische Z vervallen. We hebben de analyse gedaan op de gehele verzameling van Z vervallen (zogenaamde “events”), maar ook op twee- en drie-jet verzamelingen. The laatste twee werden gevonden met de calorimeter gebruik makende van het Durham jet algoritme met een jet resolutie parameter $y_{\text{cut}} = 0.005$. Om de “thrust” as van het event te vinden hebben we ook gebruik gemaakt van calorimeter clusters.

Eerdere onderzoeken hebben aangetoond dat de bron niet sferisch is maar

een verlengde vorm heeft in de richting van de “thrust” as in het zogenaamde longitudinale massamiddelpunts systeem. (In dit systeem heeft elk paar een Lorentz boost ondergaan, op zo’n wijze dat de som van de twee momenta in de richting van de thrust as – dit benadert de richting van de twee initiële quarks – nul is.) Terwijl verlenging bekend is, is bepaald in dit werk en andere werken dat dit slechts 20–30% is. De fit resultaten van Eq. (5.7) en (5.8) zijn geïnterpreteerd als bewijs dat in e^+e^- botsingen bij $\sqrt{s} = m_Z$ de twee-deeltjes BEC af hing van de relatieve momentum componenten alleen door de variabele Q in plaats van de componenten zelf. Dit was verder gecontroleerd door expliciete evaluatie van de twee-deeltjes Bose-Einstein correlatie functie van de variabelen $Q_0, |\mathbf{Q}|$ voor alle events en voor alle twee-jet events. Net als bij eerdere resultaten door de TASSO collaboratie [67], hebben wij gevonden dat de BEC maximaal is langs de diagonaal $Q_0^2 = \mathbf{Q}^2$, over het totaal van het experimenteel observeerbaar gebied. Dit geeft aan dat een simpele Q afhankelijkheid een goede benadering is.

Door de correlatie functie als een functie van Q te fitten, hebben we gevonden dat de aanname dat de bron een Gaussische vorm heeft te simpel was. Een mogelijke deviatie van de Gaussiaanse vorm kan fenomenologisch worden gemeten met hulp van de Edgeworth expansie. Het fit resultaat van deze expansie heeft bevestigd dat de vorm niet Gaussiaans was. Daarom zijn we naar stabiele distributies gegaan. Een van de meest belangrijke parameters van de Lévy stabiele distributies is de index van stabiliteit α , die in het interval $(0, 2]$ moet liggen. Het geval $\alpha = 2$ komt overeen met de Gaussiaanse bron distributie. De Edgeworth en de Lévy parametrisaties hebben goed werk verricht om het gedeelte $Q < 0.6$ GeV te beschrijven voor alle events, drie-jet events en twee-jet events, maar faalden bij hogere Q . In het gebied $0.6 - 1.5$ GeV komt de R_2 onder de lijn $\gamma(1 + \delta Q)$ van de lange-afstands correlaties. Het niet kunnen beschrijven van dit is de belangrijkste reden voor het falen van de Edgeworth en symmetrische Lévy parametrisaties.

Het is aangetoond dat de Q afhankelijkheid van de correlatie functie begrepen kan worden als er een sterke correlatie en lineaire relatie was tussen het vier-momentum van een geproduceerd deeltje en de ruimtetijds positie waar het was geproduceerd. Een model dat de Q afhankelijkheid voorspelt en aan de lineaire relatie voldoet is het zogenaamde τ model. Als een bijproduct van het verklaren van de Q afhankelijkheid verklaart dit model een specifieke transversale massa afhankelijkheid van R_2 . Binnen het raamwerk van het τ model hangt de emissie functie af van de eigentijd distributie $H(\tau)$. We hebben een eenzijdige Lévy distributie gekozen als de eigentijd distributie. We hebben deze fit uitgevoerd op de twee-jet data in verschillende m_t intervallen en geconcludeerd dat de belangrijkste parameters stabiel zijn: het begin van de deeltjes productie $\tau_0 = 0 \pm 0.01$ fm, de index van stabiliteit $\alpha = 0.43 \pm 0.03$ en de breedte van de eigentijd distributie $\Delta\tau = 1.8 \pm 0.4$ fm. Binnen de fouten zijn deze grootheden onafhankelijk van m_t . Dit heeft de verwachting van het τ model bevestigd.

Binnen het raamwerk van het τ model hebben we een ruimte-tijd beeld gemaakt van het emitterende proces van de twee-jet events. Om de reconstruc-

tie makkelijker te maken hebben we aangenomen dat de emissie functie gefactoriseerd kan worden als het product van een een-deeltje transversale distributie, de eigentijd distributie en de ruimte-tijd “rapidity” distributie. We hebben de emissie functie gereconstrueerd door gebruik te maken van de parameters van de fit. Van dit hebben we geconcludeerd dat deeltjes productie meteen na de botsing begint is, snel is toe neemt, en dan langzaam af neemt. In de longitudinale richting (langs de event as) heeft de emissie functie een structuur met twee pieken, met erg lange staarten langs de licht kegel. In de transversale richting word een ringvormige structuur geobserveerd, gelijk aan de expanderende ringvormige golf veroorzaakt door een steentje in een vijver.

We hebben gevonden dat BEC van alle events als van de twee- en drie-jet events beschreven is door Lévy parametrisatie. Een Lévy distributie komt van natuur te voorschijn van een fractaal, van een “random walk” of van anomale diffusie, en de parton shower van de leidende log benadering van QCD is een fractaal. In dit geval is de Lévy index van stabiliteit α gerelateerd aan de sterke koppelingsconstante α_s volgens $\alpha_s = \frac{2\pi}{3}\alpha^2$. Door de gegeneraliseerde locale parton hadron dualiteit aan te nemen, kan men verwachten dat de distributie van hadronen de eigenschappen van de gluon distributie behoudt. Van de waarde van α verkregen in de fits hebben we gevonden dat voor twee-jet events $\alpha_s = 0.39 \pm 0.05$. Dit is een aannemelijke waarde voor een schaal van 1–2 GeV waar deeltjes productie plaats vindt. Ter vergelijking, van τ veral, $\alpha_s(m_\tau \approx 1.8 \text{ GeV}) = 0.34 \pm 0.03$.

Acknowledgements

This thesis could not have been written without the help and support of many people. It would be difficult to thank them all individually. However, I would like to mention some of them explicitly.

First of all, I am deeply indebted to my supervisors, Prof. Dr. Wolfram Kittel and Prof. Dr. Tamás Csörgő, who gave me the opportunity to work in the Experimental High Energy Physics group of the Radboud University Nijmegen as a Ph.D. student. I thank Wolfram for his flexibility and expert guidance. I am also grateful for Tamás' continuous support and for the many critical discussions we had which have helped to channel the boiling flow of ideas in a more navigable way which has finally resulted in this thesis.

Special thanks go to my co-supervisor, Dr. Wesley Metzger, who guided me in the data analysis and was always there to listen and to give advice. Without his warm encouragement, I could not have finished this dissertation.

It is my pleasure to thank all members of the L3 collaboration for their combined effort to make the success of the experiment. I also thank colleagues at KFKI in Hungary for their help for the possibility to work there for a year.

I thank all the past and present members of the Experimental High Energy Physics department in Nijmegen for providing a very pleasant working atmosphere. I would like in particular to thank Yuan Hu, Jorn van Dalen, Pieter Houben, Eric Jansen, Folkert Koetsveld. Special thanks to Qin Wang, Miruna Anastasoae, Miran Djordjevic, Gustavo Ordonez, Bram Wijngaarden, Lucian Ancu, Cristina Galea for their friendship. Thanks also to Peter Klok, Frans Rohde and Wim Janssen for helping me with computers. Furthermore, I thank Marjo van Wees-Mobertz, Gemma Kopper-Janssen, Annelies Oosterhof-Meij and Hanneke Vos-van der Lugt for their kind help in the administrative domain.

Let me say 'thank you' to my football team, which kept me in good physical and mental condition. I will never forget the match what we won.

My special thanks go to my family my parents, Jenő Novák and Jenőné Novák, for giving me life in the first place, for educating me, for their support and encouragement, my sister, Anita, for listening to my complaints and

frustrations, and for believing in me.

Finally, I would like to thank Judit Pető, my partner and wife, for her unconditional love and warm support.

Curriculum Vitae

The author of this thesis was born on 16th of May 1979 in Gyöngyös (Hungary). After finishing his secondary school in 1997, he moved to Debrecen, where he studied mathematics as an undergraduate student at the Kossuth Lajos University (presently University of Debrecen). In 2002, he obtained his Master degree of Science. Immediately after that he started to work as a graduate student at the Katholieke Universiteit Nijmegen (presently Radboud University Nijmegen) in the Netherlands under the supervision of Prof. Dr. E.W. Kitzel and Dr. W.J. Metzger. During his PhD studies he has spent one year at the KFKI Research Institute for Particle and Nuclear Physics of the Hungarian Academy of Sciences in Budapest, Hungary, where his PhD supervisor was Prof. Dr. T. Csörgő. The topics of his study are those presented in this thesis: Bose-Einstein Correlations in e^+e^- Annihilation.

During his studies, he took part in several graduate schools, namely the joint Belgian-Dutch-German graduate schools at Nijmegen (The Netherlands) in 2002 and at Bonn (Germany) in 2003. He also participated in a number of international conferences and meetings including the XXXV International Symposium on Multiparticle Dynamics and the Workshop on Particle Correlations and Femtoscopy, both in Kroměříž (Czech Republic) in 2005.

Since September 2006 he has been teaching mathematics and statistics at the Károly Róbert College in Gyöngyös, Hungary and working with Prof. Dr. T. Csörgő of KFKI Research Institute for Particle and Nuclear Physics of the Hungarian Academy of Sciences, Budapest, Hungary.